Geophysical Methods for Monitoring Soil Stabilization by Microbial Induced Carbonate Precipitation

By

Sina Saneiyan

A dissertation submitted to the

Graduate School-Newark

Rutgers, The State University of New Jersey

In partial fulfillment of requirements

For the degree of

Doctor of Philosophy

Graduate Program in Environmental Sciences

Written under the direction of

Dr. Dimitrios Ntarlagiannis

and approved by

_____

_____

_____

_____

Newark, New Jersey

October, 2019

ABSTRACT OF THE DISERTATION

Geophysical Methods for Monitoring Soil Stabilization by Microbial Induced Carbonate Precipitation

By Sina Saneiyan

Dissertation Director:

Dr. Dimitrios Ntarlagiannis

Urbanization growth rate is increasing exponentially and with that comes challenging issues in urban development and environment sustainability. Generally, any development processes disturb the environment, and soil stabilization as one of the first steps in infrastructure building is no exception. However, in the past few decades, methods have been sought to reduce the possible harmful impact of soil stabilization processes on the environment. One promising method is microbial induced carbonate precipitation (MICP); in which, ubiquitous soil microorganisms stabilize the loose soil in natural and minimally harmful ways. Although MICP is continuously being studied in multi-disciplinary research, there are still ambiguities in understanding its subsurface processes. This is commonly due to lack of proper monitoring tools capable of providing coherent micro and macro scale information about MICP in subsurface. Geophysical methods are handy tools capable of providing images of the subsurface with high spatiotemporal resolution; while, being cost efficient, non-disruptive and viable for long-term monitoring applications.

This thesis is investigating the efficiency of induced polarization (IP) in monitoring MICP processes and comparing it to direct monitoring methods as well as other geophysical methods. IP is known as a sensitive method to interfacial changes within fluid-grain boundaries in porous media; hence, it is a great measure to study MICP where most changes happen in this boundary (e.g., precipitation of calcite). In this three-phase study, firstly, it is shown that spectral IP (SIP) is capable of tracking changes due to calcite precipitation (the main byproduct of MICP) in the porous media, induced by chemical reactions in a laboratory scale experiment. Compared to resistivity and shear-wave velocity, SIP provided additional information with calcite precipitation pattern. Secondly, in a field scale study, time-domain IP is compared to direct monitoring approaches (e.g., chemical analysis) and showed spatial and temporal extents of MICP in the subsurface; while, direct methods failed to provide such information. And finally, in a more in depth study, it is shown that SIP can reveal frequency dependency of MICP in both laboratory and field scale settings. The additional information provided by IP compared to other methods indicate that IP is the prime candidate for monitoring MICP processes.

Acknowledgement

First and foremost, my appreciation and utmost thanks goes to my advisor Dr. Dimitrios Ntarlagiannis, who believed in me and supported me in every step of the way throughout my Ph.D., both financially and geophysically!! Dimitris's advice was not limited to my Ph.D., he also pushed me to learn beyond the scientific scope of this dissertation, I learned things like programming which I might have never done on my own. He trusted me in multiple side works and research projects, and without him I would never have reached to this stage. I am proud to call him my friend now and not only my advisor. Thank you Dimitris!

I would like to thank my committee members, Drs. Andrea Ustra, Frederick Colwell and Dale Werkema, without whom I would not have been able to complete many parts of this thesis. Dale provided me with necessary instrumental support that helped in ground truthing my idea; Rick provided me not only with countless support on basics of microbiology, but also with the solely most important agent in microbial induced carbonate precipitation, the microbes! And Andrea who shared with me her complex programming codes, skills and theories. Thank you guys. I would also like to thank Dr. Ken Williams, whose help allowed me to work at IFRC site at Rifle, CO. for the duration of my field scale study.

I am thankful to my colleagues Junghwoon Lee and Juliette Ohan, who helped me both at the field and during my laboratory experiments and never delayed responding my numerous emails and calls asking for help.

Special thanks to Dr. Lee Slater who initially saw the potential in me as a Ph.D. student and introduced me to Dimitris and now has offered me a post-doctoral research

position here at Rutgers. I am also grateful for his scientific support, his office door was (and still is) always open to me. Thank you Lee.

My appreciation also goes towards my friends and co-officers at Rutgers Geophysical Society (SEG student chapter), Chen Wang, Yonghui Peng and Alejandro Garcia who covered for me whenever I asked them for help. I also thank the former chapter officers and Ph.D. students, Gordon Osterman and Jon Algeo.

My laboratory works would not have been finished without help of Panagiotis Kirmizakis, along with a number of undergraduate researchers who I undoubtedly benefited from their presence at Rutgers from time to time.

Liz Morrin may have retired but I can never thank her enough for her help during my first 2 years at Rutgers, she took care of my numerous administrative problems and was there for me whenever I needed her help. I would also thank Elizabeth Moncada and Nipa Sahasrabuddhe who after Liz's departure also took care of my never-ending administrative problems, purchase orders, reimbursements, and the list goes on. Special thanks to Mike Kalcynzki whose help is always beyond just technical support in the laboratory.

Thanks to Drs. Kristina Keating, Evert Elzinga, Ashaki Rouff and Adam Kustka; and their students, especially, David Shire, Alon Rabinovich and Omanjana Goswami who let me to work in their labs, use their resources and also provided me with valuable advice along the way. Thanks to Dr. Alexander Gates for supporting me and showing me the correct way of being in charge of TAs and undergraduate students for the past two years.

Finally, I thank the love of my life and beautiful wife, Azadeh. You supported me with pure love, in ways no man can ever imagine. Honey, my appreciation towards you cannot be put into words. You remain the only one I can always rely on. I love you.

I am proud to dedicate this work to my father, Saeid, and mother, Roya. You guys never stopped believing in me. Dad, you are still my role model! I have a long way to become a well-respected engineer like you, and oh I wish someday to be like you. Mom, your unconditional love is the fuel for my journey of life, I love you.

Table of Contents

List of Tables

List of Illustrations

Chapter 1: Introduction

1.1 Soil stabilization

Soils, abundant everywhere and the bed to most human activities, are constantly under degradation by natural and/or anthropogenic forces. Degradation results in soils that suffer from low cohesiveness, high porosity and permeability. While on their own, these results are not bad (especially for agricultural purposes), but from an engineering perspective, such soils are commonly known to be of substandard quality [*DeJong et al.*, 2010, 2013].

Urbanization has led to an increasing demand for robust infrastructures that are expected to last for long periods of time in developed urban areas (e.g., coastal areas and major cities). The viability of these infrastructures heavily relies on the building foundations' quality and stability; hence, the quality of the soil supporting these foundations cannot be overlooked.

Poor quality (in terms of engineering) soils are prone to liquefaction under weathering (e.g., saturation during rain events) and shear forces (e.g., earthquakes, blasting, vehicular movements); hence, such weathered soils lack sufficient stability and strength in supporting loads imposed upon them by the infrastructures. While soil degradation usually occurs naturally (and in some cases, anthropogenically), it is almost impossible to reverse or stop this process without human intervention [*DeJong et al.*, 2006, 2013; *Dhami et al.*, 2013]. The process of enhancing soil qualities (i.e., reversing the degradation) to reach engineering accepted standards is called "soil stabilization".

Soil stabilization processes involve physical, chemical and/or bio-chemical subsurface changes that result in binding loose soil grains together. These processes reduce porosity/permeability and increase the cohesiveness/stiffness of the soil; thus, improve the overall stability of the soil against shear failure [*Burbank et al.*, 2011; *DeJong et al.*, 2013].

1.1.1 Current soil stabilization practices

Conventional soil stabilization methods, currently depend heavily on artificial material and man-made forces. Physical stabilization commonly involves reduction of pore space in the soil by compressive forces (e.g., deep dynamic compaction) or thermal treatments. On the other hand, chemical treatments result in soil stabilization by increasing the cohesiveness of the soil through synthetic or natural additives that bind soil grains together (e.g., cement grouting). Although both methods have shown to be effective in enhancing engineering qualities of the soil, they have downsides as well. Due to human involvements and synthetic nature of the physical and chemical soil stabilization techniques, it is sometimes economically and/or environmentally not feasible to use these techniques. Furthermore, physical methods, such as deep dynamic compaction, are often not suitable for densely populated urban areas. Similarly, chemical treatments are capable of altering subsurface chemical properties (e.g., pH) permanently and typically include toxic material; thus, have high risk to human life (e.g., if applied near water resources). Another issue with the conventional methods is their localized impacted area; in most cases, the soil will remain unaffected (unstable) beyond 1 – 2 meters of the treatment point [*Worrell et al.*, 2001; *Karol*, 2003; *DeJong et al.*, 2006; *Chang et al.*, 2015; *Wang et al.*, 2017]. Therefore, the final outcome is usually an inhomogeneous stabilization.

The above issues often force the engineers to take conservative approaches in stabilization procedures that result in higher project costs due to excessive use of material and energy (i.e., over-design) [*Ivanov and Chu*, 2008; *DeJong et al.*, 2013; *Gomez et al.*, 2015]. Hence, it is necessary to explore the availability of reliable alternative soil stabilization techniques.

1.1.2 Microbial induced carbonate precipitation

In nature, various minerals have been seen as natural cementing material (e.g., silicates, evaporates and carbonates) [*Haeri et al.*, 2005]; hence, it is not far-fetched to imagine the existence of a natural soil stabilization method. Among the broad range of minerals that can be precipitated naturally, calcium carbonate (calcite) is one of the most common minerals on Earth [*Whiffin*, 2004]. In natural alkaline environments, where the concentration of calcium (Ca^{2+}) and carbonate (CO_3^-) ions is high, calcite will be precipitated abiotically [*Hammes and Verstraete*, 2002]. Additionally, microbial activities can result in precipitation of calcite; this process is called biomineralization [*Ferris et al.*, 1986, 1996].

In the recent decades, interdisciplinary research has paved the way for exploring new methods that can utilize microbiology, chemistry and civil engineering for the purposes of soil stabilization by harnessing the power of natural calcite precipitation. Microbial induced carbonate precipitation (MICP) is the most promising approach of soil stabilization through biomineralization of calcite. MICP is a naturally occurring process; in which, ubiquitous soil microorganisms and their metabolic activities promote the processes of calcite precipitation. In return, the precipitation of calcite in pore spaces acts

as a cohesive agent in binding unconsolidated soil grains [*DeJong et al.*, 2013; *Gomez et al.*, 2017; *Wang et al.*, 2017].

Microorganisms capable of MICP are typically motile [*Burbank et al.*, 2012], and in saturated environments can move freely in search of carbon and energy sources [*Cheng and Cord-Ruwisch*, 2012]. The motility of microorganisms makes them good candidates for a homogenous subsurface treatment. Utilizing the microbes, therefore, reduces the material injection efforts, requires less energy and results in relatively lower final stabilization project costs. Furthermore, due to the natural origins of the ingredients used in MICP (urea, calcium and ureolytic microbes); this method is relatively environmental friendly (if applied correctly) [*DeJong et al.*, 2010, 2013]. The abundance of microorganisms, the generally benign nature of MICP, combined with application cost efficiency makes MICP a strong alternative for conventional soil stabilization techniques. Nevertheless, due to limited field studies, the nature of subsurface processes during MICP remains unclear. Additionally, incorrect application can lead to high concentration of harmful byproducts (e.g., ammonia). Therefore, despite all of the mentioned benefits, the effectiveness of MICP in soil stabilization is still under scrutiny and it is a long way from practical acceptance. While numerous laboratory studies and limited field trials proved MICP works, the spatial and temporal changes during MICP are often limited to low resolution and sparse physical samplings or one-dimensional standard seismic tests.

1.2 Monitoring MICP

Generally, there are two approaches in monitoring any subsurface activities, direct and indirect techniques.

1.2.1 Direct monitoring techniques

As the name of the method implies, direct monitoring methods involve studying a process by direct analysis. The most well-known and simplest direct monitoring method is physical sampling and analysis; in which, actual samples are taken from the soil through destructive procedures that could result in permanent damage. Additionally, physical sampling only represents the point of sampling and spatial interpretation relies on extrapolation and/or excessive sampling which is not practical in most cases. Similarly, temporal interpretation is limited to sampling time and often lags behind the real time changes. Other direct monitoring techniques include, chemical, bio-sampling, X-Ray imaging/diffractometry and standard civil engineering tests (e.g., triaxial load, rebound hammer) [*Anderson et al.*, 2003; *Mitchell and Santamarina*, 2005; *DeJong et al.*, 2006; *Rodriguez-Navarro et al.*, 2012; *Gomez et al.*, 2017].

Although, direct monitoring methods are by far the most accurate type of monitoring in soil analysis, they are not always applicable. These methods are often time delayed as they need laboratory analysis. For instance, in case of effluent chemical analysis, simple fluid properties (e.g., pH, dissolved oxygen and conductivity) can be obtained with field probes, but ion concentrations or ammonia test usually need precise laboratory instruments [*Weil et al.*, 2012]. Furthermore, since direct samples only cover a small area, the reliability of monitoring studies heavily depends on numbers and frequency of sampling. Excessive sampling is expensive, and also prolongs the monitoring period and interferes with real-time monitoring.

1.2.2 Indirect monitoring techniques

In contrast with direct monitoring, indirect monitoring techniques determine sample properties through interpretation of measured physical (and/or chemical) properties that do not directly represent the property of interest [*Day-Lewis et al.*, 2017]. A promising indirect monitoring approach is the use of geophysics. Geophysical methods are acknowledged as minimally to non-invasive methods that are capable of providing subsurface insights with high spatial and temporal resolution [*Williams et al.*, 2009; *Robinson et al.*, 2012]. These techniques are relatively easy to apply and combined with right computational analytical software, can track subsurface changes in real-time [*Huang and Won*, 2003]. Additionally, for some geophysical techniques (e.g., geoelectrical methods) long-term monitoring is possible through permanent instrument installation at study sites [*Heenan et al.*, 2015]. These benefits make geophysics an environmentally friendly and economically viable monitoring approach that can significantly enhance our understanding of subsurface changes during MICP.

Nevertheless, geophysical monitoring of the subsurface alone can be challenging. Interpretation of geophysical signals could lead to erroneous, and sometimes unrealistic, conclusions. Although geophysical surveys provide images the subsurface and help delineating contrasts, standalone usage of these methods usually provides very little about the nature of the subsurface phenomena of interest. It is typically suggested to accompany geophysics with minimal direct sampling. This helps in understanding the nature of subsurface processes and a better geophysical signal interpretation.

In this thesis, I particularly focus on the geoelectrical method, induced polarization (IP). IP has a long history in mining engineering and is a well-established exploration tool

for finding ore deposits (e.g., copper) [*Dey and Morrison*, 1979a, 1979b]. IP is increasingly becoming an attractive tool in near-surface environmental studies as well, due to its unique sensitivities to interfacial properties of earth media [*Binley and Kemna*, 2005]. Additionally, IP is sensitive to calcite precipitation and microbial activities [*Ntarlagiannis et al.*, 2005; *Personna et al.*, 2013; *Saneiyan et al.*, 2018, 2019]. These qualities make IP a promising monitoring tool for MICP applications.

1.3 Objectives

This thesis explores the challenges during laboratory and field scale MICP projects and provides multiple approaches to study MICP. In order to provide a solid guideline, indirect monitoring methods have been coupled with direct methods to confirm the validity of the measurements. The ultimate goal of this thesis is to show IP is capable of MICP monitoring, and that it is: 1. able to produce reliable and repeatable data, 2. easy-to-carry out, 3. economically feasible, 4. environmentally friendly, and 5. viable for long-term monitoring. Through the main three chapters of this thesis, the following points will be investigated and demonstrated:

1. Geophysical signatures of abiotic calcite precipitation in soil samples in controlled laboratory environment (chapter 3). It is necessary to investigate the effect of calcite (only) on the geophysical signals (especially IP) prior to any microbial introductions. This will help us to better distinguish the signals of the main MICP product (i.e., calcite) from purely microbial signatures in the uncontrolled environment of field settings.
2. Field scale *in-situ* MICP and monitoring procedures. It is important to address the challenges of IP data interpretation, benefits of IP versus other geophysical

methods (electrical resistivity and nuclear magnetic resonance), overall agreement of IP signal with direct monitoring methods (X-Ray diffraction, ammonia concentration) in the field and finally to show that IP can successfully delineate MICP changes in the subsurface (chapter 4).

3. Spectral and temporal agreement of IP signal in monitoring laboratory and field scale MICP projects. Establishing the links between laboratory and field signals helps in better field data processing, typically plagued by noise and lower accuracy. In turn, this allows for better interpretation, leading to a clearer image of subsurface processes in field size monitoring applications.

This research presents a novel approach in studying MICP by utilizing remote geophysical monitoring. The advancements and findings presented in this dissertation ultimately allow for more comprehensive understanding of the underlying subsurface changes during the MICP processes at both micro and macro scale.

Chapter 2: Methods

2.1 Geoelectrical methods

The demand for locating oil and ore minerals has led to the introduction of electrical resistivity and induced polarization (IP) methods (respectively) in the early 1900s. The electrical resistivity is routinely used for groundwater mapping, environmental application (e.g., contamination plume mapping, waste dumps, saltwater intrusion, etc.) and geotechnical applications (e.g., fracture and fault mapping) [*Telford et al.*, 1976; *Dobecki and Romig*, 1985; *Ward*, 1990; *A. & Cheng*, 2012; *Ayolabi et al.*, 2013; *Robinson*, 2015]. The IP method has initially developed by C. Schlumberger in 1927 for detection of disseminated mineral ores in metal exploration [*Marshallt and Madden*, 1959; *Seigle*, 1959; *Pelton et al.*, 1978; *Wong*, 1979; *Sumner*, 2012]; more recently, IP has been used for non-exploration purposes such as environmental applications (e.g., contaminant transport) and geotechnical soil stabilization monitoring [*Börner and Schön*, 1995; *Vanhala and Soininen*, 1995; *Börner et al.*, 1996; *Scott*, 2003; *Ustra et al.*, 2012; *Ntarlagiannis et al.*, 2016; *Saneiyan et al.*, 2019].

Both methods allow for the measurement of electrical properties of porous media (soils and rocks), which are controlled by arrangement and interactions of the constituents (solids, liquids and gasses) [*Börner et al.*, 1996; *Slater and Lesmes*, 2002]. Generally, resistivity and IP are considered coupled methods and can be performed concurrently, as they follow the same measurement setup [*Hohmann and Ward*, 1981; *Ward*, 1990]. Both methods are highly regarded in the field of hydrogeophysics and are widely used to determine petrophysical properties of porous media in subsurface [*Binley and Kemna*, 2005].

2.1.1 Theory

In the presence of an applied electrical field, electrical charge transfers through material by two mechanisms: 1. movement of electrons and 2. movement of ions. While in conductors (e.g., metallic substances and graphite) the charge transfer is purely driven by electron migration (electronic conduction), in subsurface this is often not the case due to a deficiency of interconnected conductive minerals. In porous media (e.g., soils and rocks) two main mechanisms contribute to charge transport in the presence of an electrical field: 1. movement of free ions in pore fluid electrolyte (electrolytic conduction) within interconnected pore space, and 2. conduction through ions at the mineral-fluid interface (surface conduction) in the electrical double layer (EDL - Figure 2.1c). [*Binley and Kemna*, 2005]. These two ionic conduction pathways act in parallel (Equation 2.3 and Figure 2.1b) and each has its own resistance (Figure 2.1a) to the applied electrical field (current) [*Waxman and Smits*, 1968].

The electrical properties of the earth media can be expressed in form of complex conductivity (σ^* - Equation 2.1 and Figure 2.2).

$$\sigma^* = |\sigma|e^{i\phi} = \sigma' + i\sigma'' \tag{2.1}$$

$$|\sigma| = \sqrt{\sigma'^2 + \sigma''^2} \tag{2.2}$$

where $|\sigma|$ is conductivity magnitude, ϕ is phase angle, σ' is the real part and σ'' is the imaginary part of σ^* vector and *i* is the imaginary component = $\sqrt{-1}$.

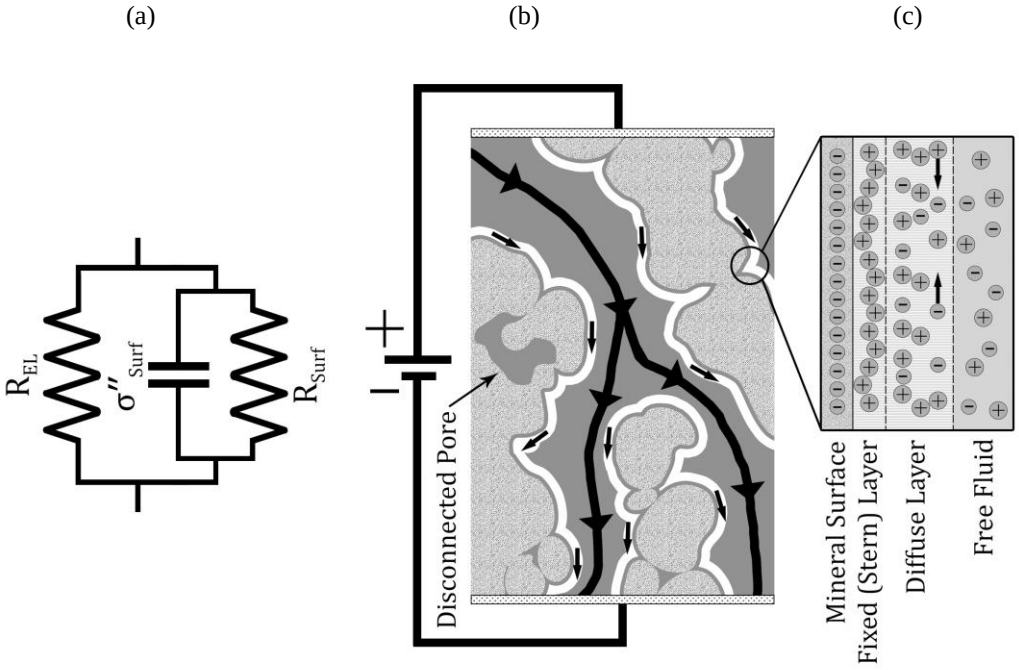

Figure 2.1: Electrical conduction pathways in porous media. (a) parallel electrical model of the earth media, (b) transportation of charge within pore-fluid and surface conduction, (c) simplified model of EDL (Modified from Binley and Slater, 2020, with permission)

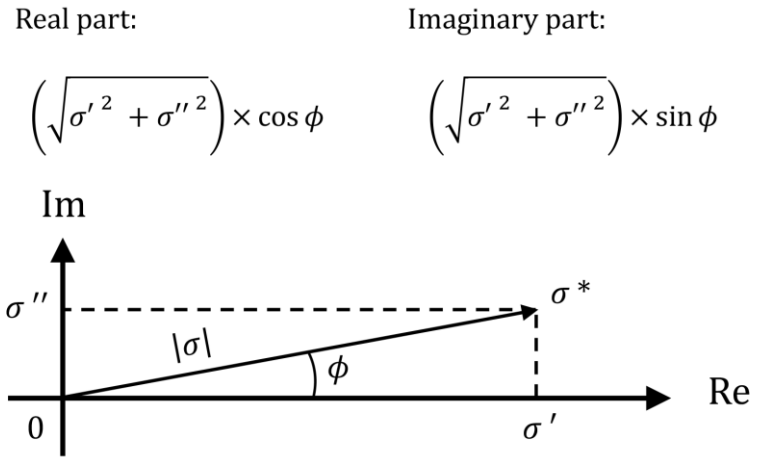

Figure 2.2: Complex conductivity in vector form. (With permission from Binley and Slater, 2020)

The real part of complex conductivity (real conductivity - σ') is purely ionic electromigration and represents energy loss, while the imaginary part (imaginary conductivity - σ'') is energy (charge) storage and is relatively small (in absence of conductors) in comparison to electromigration.

Assuming conductors/metallic particles are absent and soil grains act as insulators, at low frequency measurements the electrolytic conduction (σ_{ele}) in porous media is mainly controlled by saturation fluid conductivity (σ_w); therefore, it needs to be reduced to σ_w. This process is quantifiable by using electrical formation factor and Archie's law [*Archie*, 1942]. As σ_w depends on the availability of fluid in the interconnected pore space, formation factor (*F*) is a function of saturation (*S*) and porosity (φ) of the medium as well (Equations 2.4 and 2.5).

$$\sigma' = \sigma_{ele} + \sigma'_{surf} \tag{2.3}$$

$$\sigma_{ele} = \frac{1}{F}\sigma_w \tag{2.4}$$

$$F = S^{-n}\varphi^{-m} \tag{2.5}$$

where *S* is saturation, *n* is saturation exponent and *m* is cementation exponent which depends on arrangement of solid particles and tortuosity of the interconnected pore space.

The surface conduction is mainly controlled by the ionic conduction within the EDL (σ_{EDL}) and is a function of formation factor at the EDL (F_s). It is often assumed that $F_s = F$ so the surface conduction can be written as [*Weller and Slater*, 2012]:

$$\sigma'_{surf} = \frac{1}{F_s}\sigma_{EDL} \approx \frac{1}{F}\sigma_{EDL} \tag{2.6}$$

The σ_{EDL} is function of intrinsic conductivity of the diffuse layer (σ_{diff}), thickness of the EDL layer (δ) and pore volume normalized surface area (S_{por}); thus, the surface conductivity can be written as [*Weller and Slater*, 2012; *Weller et al.*, 2013]:

$$\sigma'_{surf} = \frac{S_{por}}{F}\delta\sigma_{diff} \tag{2.7}$$

However, in near surface applications, where fluid conductivity is relatively high, it is safe to assume $\sigma_{ele} \gg \sigma'_{surf}$ [*Slater and Lesmes*, 2002]; hence, the real conductivity can be written as equation 2.8:

$$\sigma' \approx \sigma_{ele} = S^n \varphi^m \sigma_w \tag{2.8}$$

In order to fully understand the electrical properties of the earth media, charge storage must be accounted for in addition to electromigration. In this model it is assumed that the earth is acting as a circuit in which a resistor and a capacitor are acting in parallel where the resistor is the electromigration through σ' and the capacitor is σ'' (Figure 2.1a).

At low frequencies (below 1000 Hz - where resistivity and IP measurements are made to prevent instrumental parasitic capacitive coupling [*Slater and Lesmes*, 2002; *Wang and Slater*, 2019]), the dominant mechanism controlling the charge storage (hereafter, polarization) is diffusion of the ions at the EDL in presence of an electrical field (Figure 2.1c). The polarization at the EDL (σ'') depends on ionic mobility, interfacial charge density and surface area. At frequencies higher than 1000 Hz and up to 10^8 Hz, the polarization is dominated by the Maxwell-Wagner mechanism within the dielectric materials (The frequency range for the IP measurements in this thesis is not exceeding 1000 Hz; thus, the Maxwell-Wagner mechanism is irrelevant not discussed) [*De Lima and Sharma*, 1992; *Lesmes and Morgan*, 2001; *Slater and Lesmes*, 2002; *Tabbagh et al.*, 2009].

Since σ'' is dominantly controlled by interfacial properties at the mineral-fluid interface (i.e., EDL), it is independent of electrolytic pathways. Therefore, σ'' does not follow Archie's law and can be assumed to purely follow surface conduction pathways (i.e., $\sigma'' = \sigma''_{surf}$) [*Lesmes and Morgan*, 2001].

2.1.2 Electrical resistivity

The electrical resistivity method is based on the same theory of electrical conduction in electrical circuits. In this method, usually a low frequency alternating current (sinusoidal or square wave) that is repeatedly switched on and off (current source direction switched at each on/off stage - time domain measurement) is injected into the medium and a potential drop is measured. The alternation of the current injection direction (+/-) reduces the polarization as well as the build-up of a large contact resistance at the current electrodes [*Binley and Kemna*, 2005]. Typically, electrical resistance is measured via a set of four electrode configuration (Figure 2.3 and Figure 2.4); where a pair is for current (I) injection and the other pair is to measure potential drop (ΔV). The general principles of this method follows Ohm's law (Equation 2.9):

$$R = \frac{\Delta V}{I} \tag{2.9}$$

where R is resistance (ohms), ΔV is potential drop (volts) and I is electrical current (amperes).

The measured electrical resistance depends on the electrode configuration and can vary with changing electrode spacing; thus, cannot be used as a reliable property of porous media. On the other hand, electrical resistivity (ρ) is an intrinsic physical property of the material and is independent of the measurement setup. To convert measured resistance to

resistivity, a geometric factor coefficient (*K*) is used (Equation 2.10). In the laboratory, *K* is a function of potential electrode spacing and the area that current flows through (Figure 2.3) and is measured in units of length (m). Therefore, the resistivity of the medium can be expressed as:

$$\rho = K \times R = K\frac{\Delta V}{I} \tag{2.10}$$

$$K = \frac{A}{L} \tag{2.11}$$

$$\rho = \frac{A}{L}\frac{\Delta V}{I} \tag{2.12}$$

where ρ is resistivity (Ohm.m), *A* is the cross section area (m^2) and *L* is distance between potential electrodes (m).

The field measurements follow the same rules of the laboratory measurements; however, the calculation of resistivity is slightly more complicated (as the petrophysical composition of subsurface is usually unknown). In the field, *K* is a function of electrode location and geometry of current flow lines in the subsurface (Figure 2.4). Since equation 2.10 is only true for a homogeneous half-space earth (and this is never true in reality), we use the term apparent resistivity (ρ_a) in electrical resistivity method:

$$\rho_a = K \times R \tag{2.13}$$

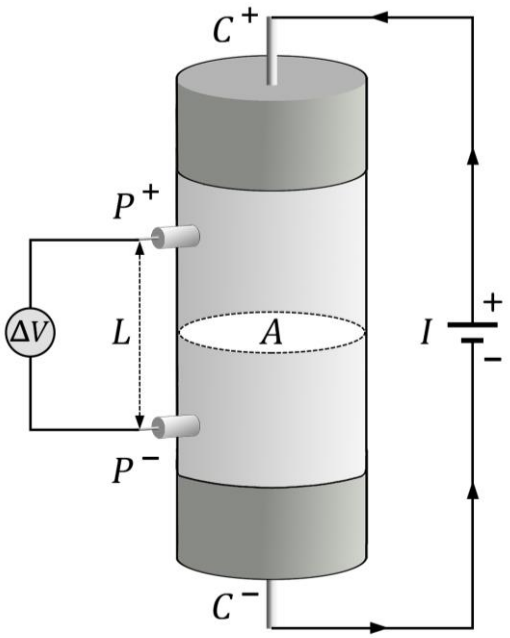

Figure 2.3: Schematics of a four electrode column setup in the laboratory for electrical resistivity measurements. (With permission from Binley and Slater, 2020)

In Electrical resistivity, it is assumed that the ground is acting as a pure resistor and opposes the applied electrical current (Equation 2.9). This method is mainly sensitive to subsurface variations in pore-fluid properties, moisture content, porosity, lithology and clay content; in other words, bulk changes in electrical properties. Therefore, the resistivity signal is less sensitive to interfacial changes and unable to separate the electrolytic and surface conduction apart. This makes the signal ambiguous especially when the dominant subsurface changes occur at the EDL (e.g., precipitation of a new isolator mineral) and there is no significant change in the pore-fluid conductivity or other bulk properties [*Slater and Lesmes*, 2002; *Binley and Kemna*, 2005].

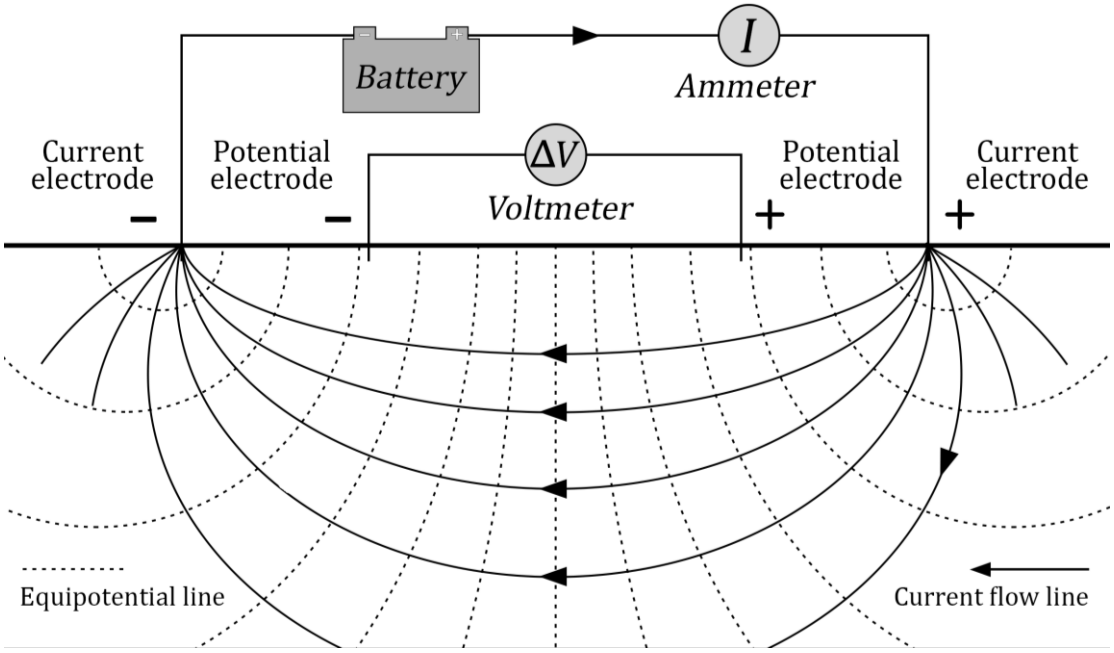

Figure 2.4: Schematics of electrical resistivity measurement of a four electrode setup. (With permission from Binley and Slater, 2020)

2.1.3 Induced polarization (IP)

IP was used in the mineral exploration field mostly and was considered mainly affected by metallic minerals until after the 1950s when the relationship between measured polarization signal in non-metallic environments became more interesting to scientists (e.g., in near-surface environmental applications). IP measurements use the same survey principles as electrical resistivity (four electrode configuration) and the measurements can be made in time-domain (TIPD) or frequency-domain (spectral IP).

Although resistivity and IP are controlled by the same porous media constituents, their effects are observed due to different physical expressions. While in electrical resistivity the signal in dominantly controlled by pore-fluid properties, the IP signal is sensitive to both pore-fluid and interfacial properties of the media. Thus, in the IP it is

assumed that the earth acts as a parallel resistor and capacitor circuit (Figure 2.1a). This is notably important as IP can resolve the ambiguity of the electrical resistivity signal when the main subsurface changes occur at the EDL [*Binley and Kemna*, 2005].

2.1.3.1 Time-domain IP

Theoretically, upon injection of an electrical current, the voltage should immediately increase to its maximum value and drop to zero when the current is shut off. This is the case for non-polarizable substances; however, in a polarizable medium a gradual voltage decay is observed when the current injection is stopped (Figure 2.5). In time-domain IP (TDIP) this effect is called apparent chargeability (M_a). In the porous medium, the gradual decay is due to charge storage at the mineral-fluid interface (at low frequencies and absence of interconnected metallic minerals) and is a complex function of electrical polarization at the EDL [*Binley and Kemna*, 2005].

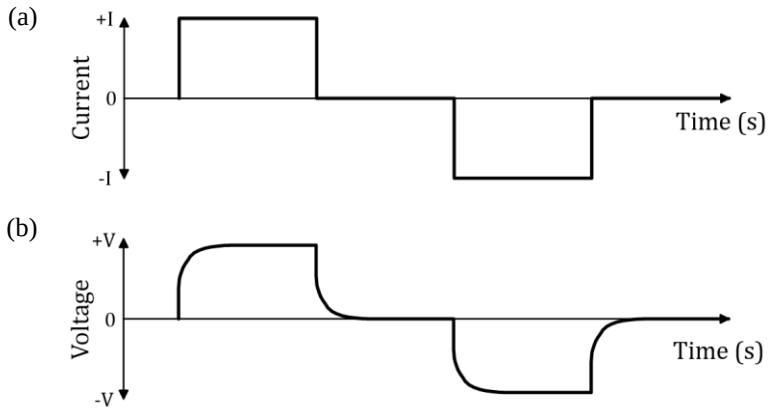

Figure 2.5: Schematics of TDIP signal. (a) DC current on/off over time, (b) measured voltage over time. Notice due to polarization, voltage does not abruptly reach the maximum magnitude and also does not reach to zero. (With permission from Binley and Slater, 2020)

M_a is quantifiable as the ratio of voltage right after the current is shut off (V_s) over the primary voltage during the current being on (V_p). M_a is unitless, although typically it is reported as mV/V (Figure 2.6 and equation 2.14) [*Seigle*, 1959]:

$$M_a = \frac{V_s}{V_p} \tag{2.14}$$

Although in theory equation 2.14 is correct, in practice V_s is significantly small and hard to measure instantaneously after the current shut off. Therefore, M_a is commonly quantified as the integral of the voltage decay curve over a period of time (Figure 2.6 and equation 2.15):

$$M_a = \frac{1}{(t_2 - t_1)} \frac{1}{V_p} \int_{t_1}^{t_2} V(t)dt \tag{2.15}$$

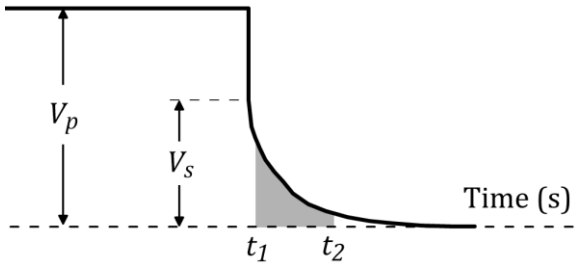

Figure 2.6: Voltage decay curve and measurement of V_s and V_p. (With permission from Binley and Slater, 2020)

2.1.3.2 Frequency domain IP

Unlike the electrical resistivity and TDIP, in frequency domain IP (hereafter spectral IP – SIP), a continuous alternating current is injected into the medium and a phase-shifted voltage (relative to injected current) is measured (Figure 2.7).

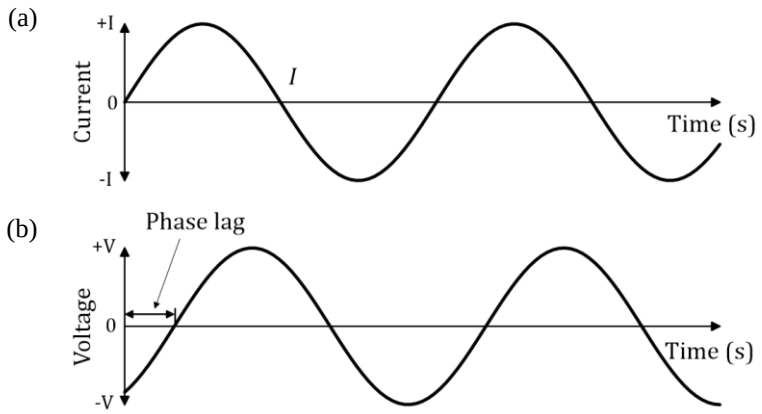

Figure 2.7: Schematics of SIP signal . (a) AC sinusoidal current wave, (b) measured voltage over time. Notice due to polarization, voltage has a phase lag relative to injected current. (With permission from Binley and Slater, 2020)

The typical frequency range of SIP instruments varies between 1 mHz to 10 KHz and measured parameters are voltage phase lag (ϕ) and impedance ($|Z|$). Impedance is function of bulk changes in the porous media (similar to resistivity) while in absence of conductors (e.g., interconnected metallic particles) phase lag is dominantly controlled by interfacial properties (and to a lesser degree fluid conductivity). SIP signal thus can be expressed in the form of complex conductivity (Equation 2.1) and real (σ') and imaginary (σ'') conductivity values can be calculated as:

$$\sigma' = |\sigma|\cos(\phi) \tag{2.16}$$

$$\sigma'' = |\sigma|\sin(\phi) \tag{2.17}$$

where $|\sigma|$ is conductivity magnitude (Equation 2.20) in S/m and ϕ is voltage phase lag (Equation 2.18) in radians. Figure 2.8 illustrates how the SIP parameters are obtained.

$$\phi = \frac{2\pi\Delta T}{T} \tag{2.18}$$

$$|Z| = \frac{|U|}{|I|} \tag{2.19}$$

$$|\sigma| = \frac{1}{K \times |Z|} \tag{2.20}$$

where K is geometric factor in units of meter.

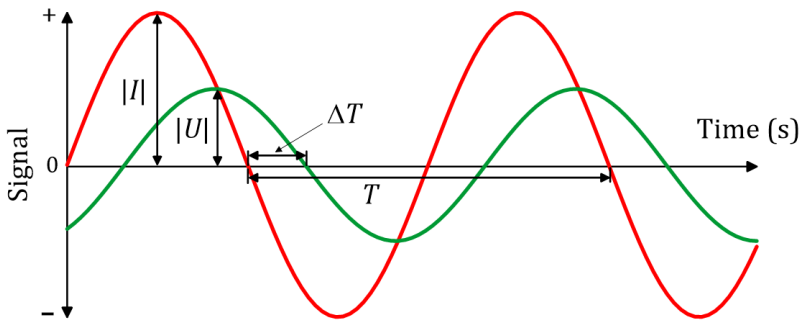

Figure 2.8: SIP signal parameters. Red: injected current (I) wave form. Green: measured potential (U) wave form.

2.2 Shear-wave velocity

In the field of geotechnical engineering, a common practice for soil quality assessment is to measure its small-strain shear modulus (G_{max}). G_{max} provides valuable information about soils' engineering properties, such as dynamic response of soil to loads, deformation characteristics and is used for liquefaction and soil stabilization assessments. Therefore, G_{max} can be used to measure cementation efficiency of the soils [*Lee and Santamarina*, 2005; *DeJong et al.*, 2006; *Choo et al.*, 2017]. G_{max} is obtained through measurement of shear-wave velocity (V_s) through equation 2.21 [*Santamarina et al.*, 2001].

$$G_{max} = \rho V_s^2 \tag{2.21}$$

where V_s is shear-wave velocity (m/s) and ρ is soil density.

In the laboratory scale measurements, shear-wave velocity is commonly measured in enclosed cells equipped with piezoelectric bender elements. Piezoelectricity is generation of electrical charge in certain material (e.g., quartz, certain ceramics) under mechanical stress. Conversely, the crystalline structure of piezoelectric material can be temporarily changed under applied electrical field [*Lee and Santamarina*, 2005].

A bender element is composed of two thin layers of piezoelectric ceramics connected to each other by a thin conductive metal plate. In parallel bender elements (the type used in this thesis) the two piezoelectric layer have same poling direction and the ground cable (current "-") is connected to the outer parts, while the signal cable (current "+") is connected to the inner part through the thin metal layer (Figure 2.9a). Alternating the ground and signal polarity, results in contraction of one piezoelectric layer and expansion of the other. Ultimately, the bender element moves up and down with change of electrical signal polarity (Figure 2.9b) and produces a shear-wave signal. It has been shown that a square-wave signal (step signal) generally produces highest signal to noise ratio of shear-wave signal (i.e., larger waves) [*Lee and Santamarina*, 2005].

(a) (b)

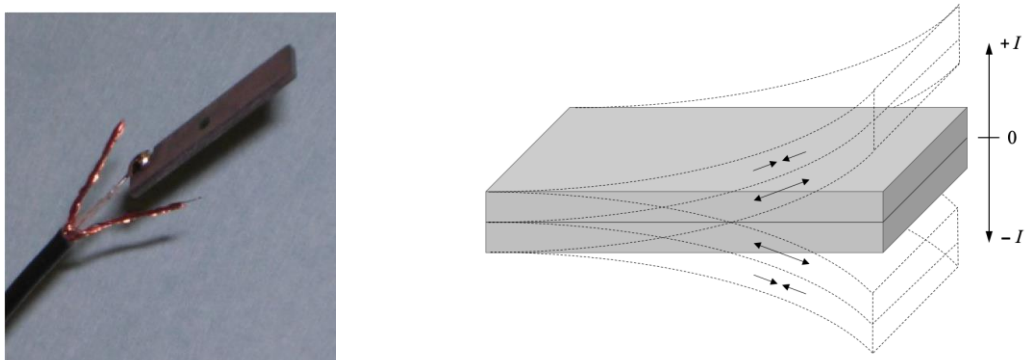

Figure 2.9: Piezoelectric bender elements with parallel setup. (a) actual bender element. The ground cable is attached to both outer sides of the bender element while the signal cable is attached to the thin intermediate metal plate. (b) schematics of bender element deformation under alternating electrical signal.

The shear-wave velocity is calculated based on the distance between two bender elements (Figure 2.10b) over the time it takes for the signal to travel this distance (Equation 2.22). Travel time is usually measured as the first arrival time for the first observed peak in the received signal (Figure 2.10a).

$$V_s = \frac{d}{t_s} = \left(\frac{G_{max}}{\rho}\right)^{\frac{1}{2}} \tag{2.22}$$

where d is distance between two bender elements (m) and t_s is first arrival time (s).

(a) (b)

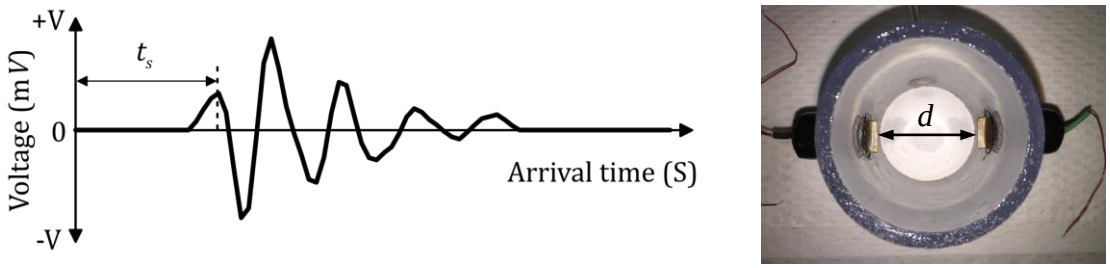

Figure 2.10: Shear-wave schematics. (a) Shear-wave response signal , (b) bender elements setup in a measurement cell. *d* is the diameter of the column and the travel distance of the shear-wave.

2.3 Microbial induced carbonate precipitation

Microbial carbonate precipitation is a common naturally occurring process that can be easily controlled and manipulated into an induced process [*Whiffin*, 2004]. The fastest and easiest method of microbial induced carbonate precipitation (MICP) is by utilizing urea hydrolysis (ureolysis). Ureolysis results in the production of urease enzyme which breaks down urea into carbonate (CO_3^{2-}) and ammonium (NH_4^+) ions. In presence of calcium (Ca^{2+}) ions, microbial produced carbonate ions react with Ca^{2+} and carbonate minerals (e.g., calcite, aragonite, etc.) will be precipitated (Equations 2.23 to 2.28) [*Hammes and Verstraete*, 2002]. Thus, the best agents for these processes are microbial communities capable of producing high amounts of urease. The dominant precipitated carbonate mineral through MICP is calcite [*Whiffin et al.*, 2007].

MICP is solely used in this thesis for the purpose of soil stabilization and in this regard, generally has three steps:

1. Microbial urea hydrolysis (Equation 2.23). In this step, ammonium (Equation 2.26) and carbonate ions (Equation 2.27) are released in to the system:

$$NH_2\text{-}CO\text{-}NH_2 + 3H_2O \rightarrow NH_2COOH + NH_3 \quad (2.23)$$

$$NH_2COOH + H_2O \rightarrow H_2CO_3 + NH_3 \quad (2.24)$$

$$H_2CO_3 \leftrightarrow HCO_3^- + H^+ \quad (2.25)$$

$$2NH_3 + 2H_2O \leftrightarrow 2NH_4^+ + 2OH^- \quad (2.26)$$

$$HCO_3^- + H^+ + 2OH^- \leftrightarrow CO_3^{2-} + 2H_2O \quad (2.27)$$

2. Reaction of available carbonate ions with calcium ions in calcium rich aqueous environment and precipitation of calcite:

$$Ca^{2+} + HCO_3^- + OH^- \rightarrow CaCO_3 \downarrow + H_2O \quad (2.28)$$

At this step usually calcium ions attach to microbial cells as well and result in precipitation of microbial calcite minerals as well [*Cheng and Cord-Ruwisch*, 2012; *Anbu et al.*, 2016]:

$$Ca^{2+} + \text{microbial cell} \rightarrow \text{Cell-}Ca^{2+} \quad (2.29)$$

$$\text{Cell-}Ca^{2+} + CO^{3-} \rightarrow \text{Cell-}CaCO_3 \downarrow \quad (2.30)$$

3. Binding of loose soil grains by calcite crystals (Figure 2.11).

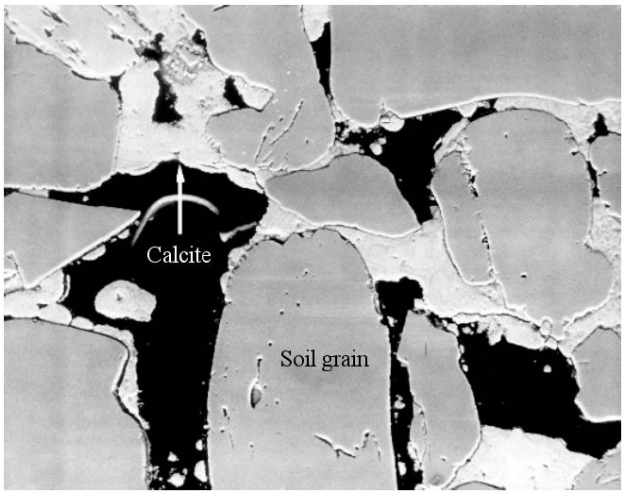

Figure 2.11: Cross section of soil (silica sand) cemented with calcite (Image credit: Calcite Technology Pty Ltd) [*Whiffin*, 2004].

2.3.1 Microbial selection and preparation

For this research, *Sporosarcina pasteurii* (*S. pasteurii* - strain 11859) was obtained from American Type Culture Collection (ATTC). *S. pasteurii* is an aerobic bacterium known for its high urease (enzyme that decomposes urea) production capabilities [*Whiffin*, 2004], ability to adapt to harsh environmental conditions [*Bhaduri et al.*, 2016] and to grow in low-cost media [*Omoregie et al.*, 2019]. Table 2.1 shows the growth medium constituents for growing these microbial cells [*Whiffin et al.*, 2007].

Table 2.1: ATTC growth medium for *S. pasteurii*

Constituent	***Amount***
Yeast extract (powder)	20.0 g/L
Ammonium sulfate ($(NH_4)_2SO_4$)	10.0 g/L
Tris buffer (to achieve pH 9.0)	15.75 g/L

Microbial communities initially were cultivated on solid growth media (on agar gel filled Petri dishes) from frozen batches for at least 24 hours at 32 ^{o}C and after obtaining visual confirmation of a healthy growth (Figure 2.12a), were transformed into conical flasks (Figure 2.12b) containing 100 mL of liquid broth growth media (Table 2.1).

(a) (b)

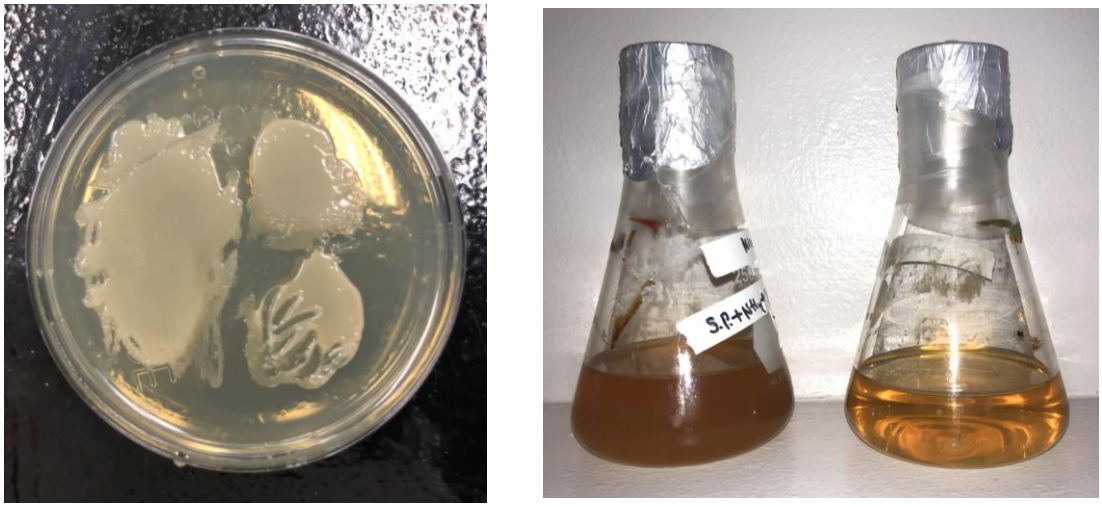

Figure 2.12: Growing *S. pasteurii*. (a) microbial culture of *S. pasteurii* growing on solid medium. Similar color and shape of the isolated and large colonies supports the fact that this culture is healthy and uncontaminated. (b) liquid state microbial culture of *S. pasteurii*. Right: uninoculated liquid broth. Left: turbid liquid broth, indicating presence of active microbial cells.

Inoculated liquid broth flasks were incubated under aerobic condition (shaking) at 32 ^{o}C until turbidity was observed (Figure 2.12b left). At this stage microbial cells were harvested by centrifuging the liquid media to obtain a pellet of concentrated cells at the bottom of the centrifuge tube. The pellet then was re-suspended in desired injection/treatment solution for the next step.

Chapter 3: Geophysical methods for monitoring soil stabilization processes[1]

Abstract

Soil stabilization involves methods used to turn unconsolidated and unstable soil into a stiffer, consolidated medium that could support engineered structures, alter permeability, change subsurface flow, or immobilize contamination through mineral precipitation. Among the variety of available methods carbonate precipitation is a very promising one, especially when it is being induced through common soil borne microbes (MICP – microbial induced carbonate precipitation). Such microbial mediated precipitation has the added benefit of not harming the environment as other methods can be environmentally detrimental. Carbonate precipitation, typically in the form of calcite, is a naturally occurring process that can be manipulated to deliver the expected soil strengthening results or permeability changes. This study investigates the ability of spectral induced polarization and shear-wave velocity for monitoring calcite driven soil strengthening processes. The results support the use of these geophysical methods as soil strengthening characterization and long term monitoring tools, which is a requirement for viable soil stabilization projects. Both tested methods are sensitive to calcite precipitation, with SIP offering additional information related to long term stability of precipitated carbonate. Carbonate precipitation has been confirmed with direct methods, such as direct sampling and scanning electron microscopy (SEM). This study advances our understanding of soil strengthening processes and permeability alterations, and is a crucial

[1] This chapter is published as: Saneiyan, S., Ntarlagiannis, D., Werkema, D.D., Ustra, A., 2018. Geophysical methods for monitoring soil stabilization processes. J. Appl. Geophys. 148, 234–244.

step for the use of geophysical methods as monitoring tools in microbial induced soil alterations through carbonate precipitation.

3.1 Introduction

Society is facing many challenges with ground quality, including soil stability, in densely populated areas [*DeJong et al.*, 2010]. The nature of soils, their use and induced changes (natural and/or anthropogenic) could lead to engineering problems [*DeJong et al.*, 2013]. Due to space limitations in densely populated areas, there is a need to enhance soil stiffness to address practical engineering problems, such as supporting standard foundations for building purposes [*DeJong et al.*, 2010], erosion prevention and dust control [*Montoya et al.*, 2013], crack remediation, and permeability reduction [*Abo-El-Enein and Ali*, 2012].

Soil stabilization methods, which increase soil stiffness and reduce permeability and porosity, have been introduced to address these engineering problems and risks to human health. *DeJong et al.*, 2010 discusses the cost of soil stabilization process and estimates US$6 billion/year for more than 40,000 soil improvement projects worldwide. Common soil stabilization methods use materials such as cement, epoxy, acrylamide, phenoplasts, polyurethane, and glass water, which are all materials typically harmful to the environment. These materials commonly produce large amounts of CO_2 during production and leachate to groundwater resources can be poisonous (e.g., acrylamides) [*Worrell et al.*, 2001; *Karol*, 2003; *Chang et al.*, 2015]. Additionally, these methods are expensive, difficult to maintain over long periods of time, result in heterogeneous application, and could negatively impact soil properties [*DeJong et al.*, 2006].

Methods are needed that could offer enhanced soil stability, without the problems current approaches face. Microbial induced carbonate precipitation (MICP) offers an alternative soil stabilization approach and, if applied properly, can be a cost efficient, long term, and a relatively environmental friendly approach (e.g., uses less synthetic material and consumes CO_2 in cementation process) [*Ivanov and Chu*, 2008; *Anbu et al.*, 2016]. MICP typically involves the use of common soil borne microbes to promote calcite precipitation; calcite in return acts as the cementing agent for loose soils [*Dhami et al.*, 2013]. MICP's final result is similar to geochemical calcite precipitation (or lime injection soil stabilization), where both utilize calcite as the cementation agent. However, MICP is less expensive and more energy efficient because it requires less mechanical energy and man-made materials to apply [*DeJong et al.*, 2010]. Finally, the MICP application is non-disruptive to existing subsurface structures and can enhance the soil stiffness over larger areas due to low viscosity and injection pressure requirements [*DeJong et al.*, 2013].

3.1.1 Monitoring process

Soil stabilization processes (such as MICP) are typically long term projects and require continuous, high resolution monitoring. Subsurface monitoring can be achieved through direct or indirect monitoring techniques. Direct monitoring involves high accuracy destructive sampling and analysis (e.g., SEM imaging, pH, microbial activity and chemical concentration changes) but the methods used are typically spatially limited, invasive, expensive, labor intensive and lacking in real-time monitoring capabilities. On the contrary, indirect measurements (e.g., geophysical methods) offer high temporal and spatial capability, cost efficiency, and noninvasiveness; but have accuracy limitations [*Weil et al.*, 2012]. Since biochemical processes during microbial activities (e.g., MICP) can alter

subsurface physical and chemical properties, geophysical methods can be used as monitoring tools [*Atekwana and Slater*, 2009a]. This is not uncommon since geophysical methods have been used for engineering and environmental purposes, such as ground quality characterization [*Arjwech and Everett*, 2015].

We utilize two geophysical methods, shear-wave velocity and spectral induced polarization (SIP) for this MICP experiment. Shear-wave velocity is chosen because shear-wave velocity is commonly used by engineers to measure soil stiffness for soil strengthening processes [*DeJong et al.*, 2010] and it has been shown to be sensitive to MICP [*DeJong et al.*, 2006]. Although shear-wave velocity measurements are sensitive to soil stiffness changes [*DeJong et al.*, 2010], long term implementation can be challenging. Furthermore, shear wave measurements provide information only on the soil properties, not on the biological processes, and this is not optimal for microbial induced treatments (such as MICP). SIP is an established geophysical method in the mineral exploration, with multiple recent environmental applications due to its unique sensitivity to interfacial and bulk properties of earth media [*Kemna et al.*, 2012]. SIP is also shown to be sensitive to microbial cells [*Ntarlagiannis et al.*, 2005], biofilm formation [*Davis et al.*, 2006], and biogeochemical processes [*Flores Orozco et al.*, 2011]. As a result, SIP is an attractive candidate for the monitoring of soil strengthening processes since it is sensitive to MICP products and processes (e.g., calcite precipitation) [*Ntarlagiannis et al.*, 2005; *Wu et al.*, 2010; *Martinez et al.*, 2013] and is suitable for long term, remote controlled, and autonomous operation [*Slater and Sandberg*, 2000].

3.2 Material and methods

The most important aspect of MICP is calcite precipitation. Hence, for the geophysical monitoring of MICP to be successful, it is necessary to characterize the geophysical signatures of calcite precipitation in common porous media. *Wu et al.* (2010) conducted a series of measurements on glass beads showing that calcite precipitation can be detected with SIP measurements. The research presented here builds on this previous successful research [*Wu et al.*, 2010] through increasing complexity by utilizing sand/clay mixtures as porous media in an attempt to replicate a closer approximation to field conditions and by measuring shear-wave velocity in order to assess possible seismic property alterations due to MICP.

3.2.1 Geochemistry

$CaCl_2$ and Na_2CO_3 are the two solutions required for precipitating calcite [*Wu et al.*, 2010]. Calcite will be precipitated upon contact of $CaCl_2$ with Na_2CO_3 (Equation 3.1) and the precipitation will continue along the solution mixing zone [*Laabidi and Bouhlila*, 2016]. Equation 3.2 shows the ionic reaction resulting in calcite precipitation. Chemical modeling [*Gustafsson*, 2016] suggests that the resulting solution of this mixture, under our experimental conditions, will be over saturated with a stable form of solid phase calcite. In addition, other unstable forms of calcium carbonate (e.g., Vaterite, Aragonite and Monohydrocalcite) could be precipitated (Table 3.1).

Table 3.1: Minerals resulting from $CaCl_2$ and Na_2CO_3 mixture based on geochemical modeling (Visual MINTEQ).

Mineral	***Saturation index***
Calcite	1.976
Aragonite	1.832
Other carbonate minerals	>1 (oversaturated)
Non-carbonate minerals	<1 (undersaturated)

$$Na_2CO_3\,(aq) + CaCl_2\,(aq) = CaCO_3\,(s) + 2\,NaCl\,(aq) \quad (3.1)$$

$$CO_3^{2-} + Ca^{2+} = CaCO_3 \quad (3.2)$$

3.2.2 Spectral induced polarization

Electrical current in the subsurface typically travels through electrolytic (σ_{ele}) and surface (σ_{surf}) conduction. Additionally, electronic (σ_{elc}) conduction occurs in the presence of interconnected metallic minerals. Both electrolytic and surface conduction pathways are ionic in nature, the former through the fluids in the interconnected pore space, and the latter through the electrical double layer (EDL) at the available solid – fluid interfaces [*Binley and Kemna*, 2005]. Electrolytic conduction is a purely real term whereas surface conduction is a complex one [*Weller et al.*, 2010]. Fluid properties are captured through σ_{ele}, while σ_{surf} is primarily controlled by the surface properties (e.g., surface area, pore size distribution, surface charge density) and with less dependence on fluid properties [*Lesmes and Frye*, 2001; *Binley and Kemna*, 2005; *Weller et al.*, 2013].

Spectral induced polarization is an extension of the commonly used DC resistivity method by allowing for measurement of the complex electrical properties of earth media [*Binley and Kemna*, 2005; *Kemna et al.*, 2012]. For the application of SIP, the conductivity

magnitude ($|\sigma|$) and phase (ϕ) are measured and then converted to the real (σ') and imaginary (σ'') components of complex conductivity (σ^*):

$$\sigma^* = |\sigma|e^{i\phi} = \sigma' + i\sigma'' \quad (3.3)$$

$$\sigma' = |\sigma|\cos(\phi) \quad (3.4)$$

$$\sigma'' = |\sigma|\sin(\phi) \quad (3.5)$$

where $i^2 = -1$. Assuming a parallel conduction pathway [*Waxman and Smits*, 1968]:

$$\sigma' = \sigma'_{ele} + \sigma'_{surf} \quad (3.6)$$

$$\sigma'' = \sigma''_{surf} \quad (3.7)$$

In this model, σ' represents electromigration (energy loss), and σ'' represents charge polarization (energy storage).

Phenomenological models, such as Debye decomposition (DD) and Cole-Cole, are commonly used to describe the spectral shape of SIP data [*Nordsiek and Weller*, 2008; *Ustra et al.*, 2016; *Weigand and Kemna*, 2016]. Debye relaxation, as applied on porous media, is related to the mineral grain charge transport properties, and could provide additional information on the rock - mineral matrix. Using DD models, the relaxation time distribution (RTD) can be retrieved, from which the grain and pore size distribution can be estimated [*Florsch et al.*, 2014; *Kruschwitz et al.*, 2016; *Ustra et al.*, 2016]. Since the dominant process of soil stabilization methods is the formation and evolution of a new mineral phase (e.g., calcite), RTD could be used to track precipitation and dissolution processes, especially over long periods of times.

3.2.3 Shear-wave velocity

Many soil properties (from an engineering perspective, e.g., stiffness) can be derived from small-strain shear modulus (G_{max}). The value of G_{max} can be obtained from shear-wave velocity measurement by the use of piezoelectric bender elements[*Lee and Santamarina,* 2005; *Choo et al.*, 2017] through equation 8. A piezoelectric bender element is a thin, two-layer plate that can be installed in most soil cells [*Lee and Santamarina*, 2005] and is designed for shear-wave velocity measurements in laboratory scale experiments [*DeJong et al.*, 2006]. Piezoelectricity results in deformation of a crystalline structure of the piezoelectric substance by applying an electrical field. Interestingly, even a different polarity of the electrical field can result in different deformations. Piezoelectric substances can produce polarized electricity by applying load (deformation of the crystalline structure) [*Lee and Santamarina,* 2005] which can be monitored by designated instruments.

$$V_s = \left(\frac{G_{max}}{\rho}\right)^{\frac{1}{2}} \tag{3.8}$$

where V_s is the shear wave velocity, G is the shear modulus, and ρ is the soil density [*Santamarina et al.*, 2001].

3.2.4 Column setup

Laboratory experiments were conducted in PVC sample holders that were optimized for both SIP and shear-wave velocity measurements (Figure 3.1). The column is equipped with three ports (two for injection, one for outflow) allowing flow control and including an effluent fluid sample collector. Two bender elements were mounted at the top and bottom and two at the sides of column. Two electrodes (at top and bottom) were

designated for current injection and two middle electrodes (at the sides) were designated for electrical potential measurements (Figure 3.1). Non-polarizing Ag-Cl electrodes, placed outside the current flow, were used here to minimize any spurious polarization effects [*Vanhala and Soininen*, 1995; *Abdulsamad et al.*, 2016]. SIP measurements on fluid filled samples holders confirmed that the non-conductive epoxy coated bender elements used do not interfere with the electrical signals.

3.2.5 Sample preparation

Two different types of porous media were evaluated: (1) Ottawa sand (Diameter: 0.6 – 0.85 mm), and (2) Ottawa sand - kaolinite mixture (95% by weight (BW) Ottawa sand, 5% BW kaolinite). The sand – kaolinite mixture was mechanically mixed, following standard laboratory procedures, for homogeneous mixing [*Heenan et al.*, 2013]. Following the process described in *Wu et al.* (2010), a mixture of 20mM $CaCl_2$ and 20 mM Na_2CO_3 was used to precipitate calcite.

All columns were wet packed (where the soil was dumped slowly in the $CaCl_2$ solution and settled with gravitational forces, to minimize the chance of air bubble presence in the medium) by following identical packing procedures in an effort to minimize discrepancies between different columns. To ensure that the columns reached chemical equilibrium before the experiment commenced, we performed daily SIP and shear wave measurements on the packed columns until reaching consistent results [*Personna et al.*, 2013].

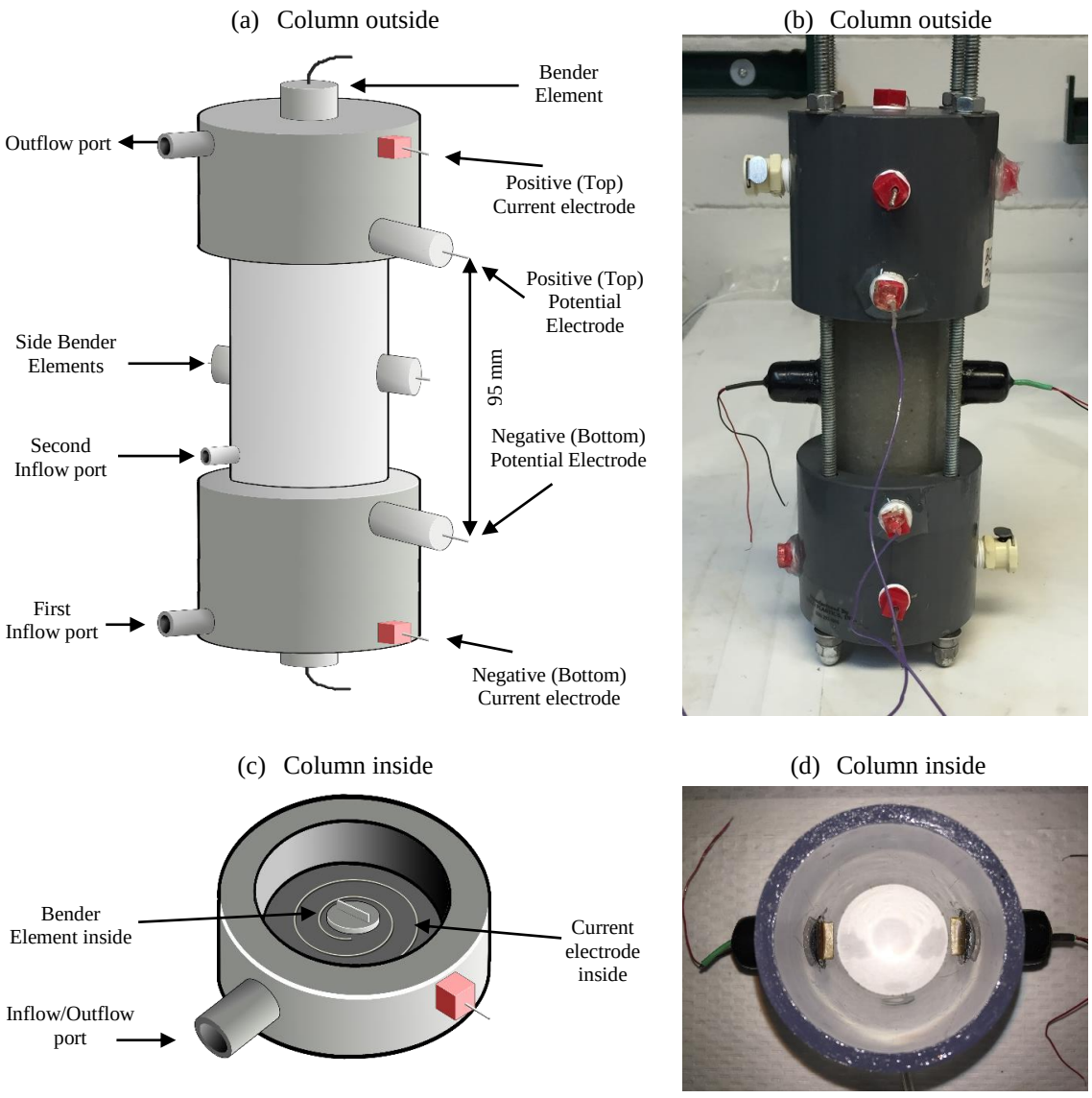

Figure 3.1: Column setup , (a, c) Schematic setup, (b, d) Actual column

3.2.6 Experiment procedure

Each soil sample involved duplicate active columns (promoting calcite precipitation), and a single control column (no calcite precipitation). All experiments started after the columns reached equilibrium, which was 72 hours under our experimental conditions. At time zero [0], background SIP and shear-wave velocity were measured as

well as influent/effluent pH and conductivity. The fluids were also collected and properly stored for detailed chemical analysis. We used an open flow regime with a flowrate of 0.04 ml/min, which was chosen to mimic common ground water flow velocity in porous media and prevent particle loss from the column. Figure 3.2 schematically describes the experiment process (inside of the columns) highlighting the injection ports, and estimated area of precipitation.

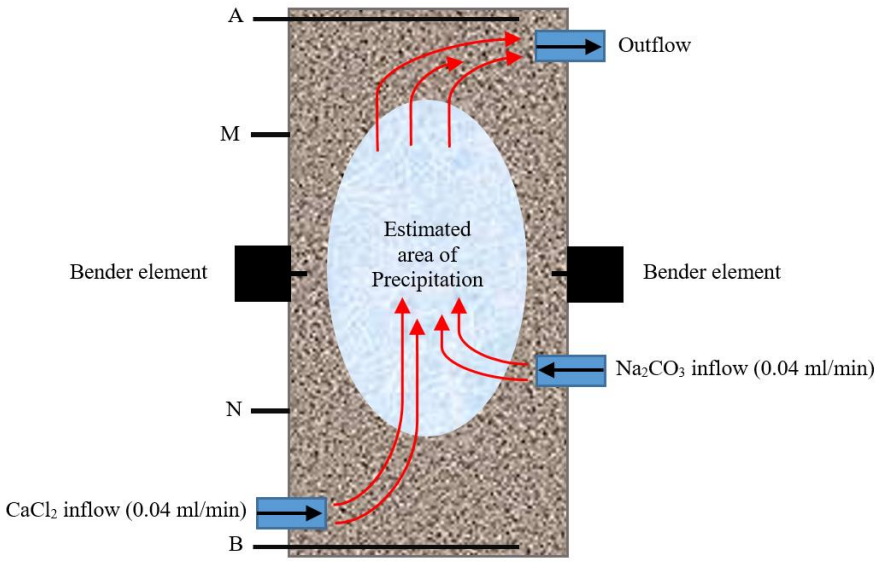

Figure 3.2: Schematic of injection process and estimated area of precipitation. A, B are current and M, N are potential electrodes.

We performed continuous SIP monitoring for the duration of the experiment using the following parameters: 4.5 hours' cycle, frequency range of 1 mHz to 24 KHz, with 5 measurements per logarithmic cycle. Shear wave velocity measurements were carried out daily. Fluid samples were collected daily, from the outflow sealed container. For the 100% sand sample we also conducted hydraulic conductivity (HC) measurements using the constant head method [*Head*, 1994] prior to injection and after the experiment.

Unfortunately, due to the loss of clay in the process of HC measurement, we could not perform this experiment on the sand + clay samples. The entire experiment including all measurements, were performed in a temperature controlled laboratory (25 ^{o} C, ±1^{o} C).

At the end of the experiment, destructive sampling was performed on all columns (Figure 3.3). Columns were drained and core samples were taken for scanning electron microscope imaging (SEM). The core samples were oven dried to eliminate any moisture, as is required for SEM imaging.

(a) Coring

(b) Remained hole after sampling

Figure 3.3: Destructive sampling for SEM , (a) Taking a core sample by pushing an open (both sides) PVC tube in the soil, (b) the open hole not collapsing after soil sampling, suggests a stiff sand formation

3.3 Results

Mixing the two solutions (Table 3.2) leads to observable change in conductivity and pH (Figure 3.4a and b). For both active columns, the conductivity decreased, while the pH increased; changes observed in the control column are minimal, probably associated with the effect of flow, and small preparation differences within the saturation media (e.g., fluid temperature) [*Akiya and Savage*, 2002]. Inductively coupled plasma (ICP) analysis showed a decrease in effluent dissolved calcium concentration right after the injection started, although this decrease for the sand + clay sample was more dramatic at the beginning (Figure 3.4c).

The hydraulic conductivity (K) of the sand sample was measured in two stages, immediately after packing, then before the injection of the mixing solutions, and again at the end of the experiment (240 hours). K reduced an order of magnitude over that period; (Table 3.3), while no changes in K were observed for the control column (Table 3.3).

Table 3.2: Inflow fluid properties

Solution	***pH***	***Conductivity* (*S*/*m*)**	***Concentration* (m*M*)**
$CaCl_2$	4.9	0.289	20
Na_2CO_3	10.9	0.374	20

Table 3.3: Hydraulic conductivity (K) changes

Sample	***Initial K* (cm/s)**	***Final K* (cm/s)**
100% Sand	0.22	0.04
Control	0.23	0.23

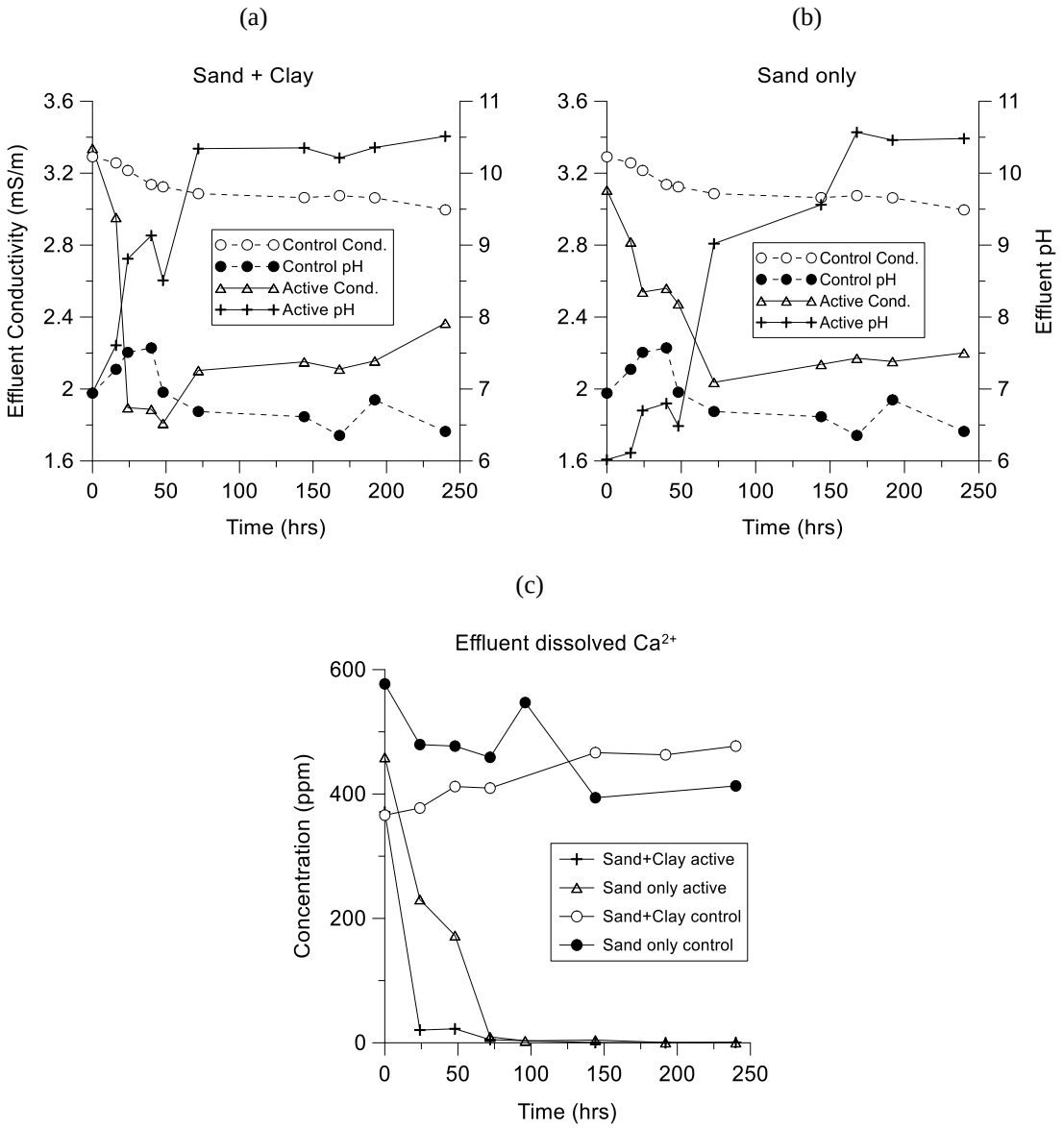

Figure 3.4: Evolution of saturating fluid over time sampled in the outflow; time = 0 hrs represents the injection zero [0] time. Two different porous media used, (a) sand + clay, (b) Sand only, (c) Effluent calcium concentration (ppm)

The imaginary component of the complex conductivity changed as the experiment progressed, presumably in response to calcite precipitation (Figure 3.5). Although we monitored changes every 4.5 hours, we present a subset of the data that presents visually cleaner figures while preserves the trend observed (24 hour cycles). For both active samples, the magnitude of the imaginary conductivity response is developing two distinctive peaks at frequencies of 1 Hz and 1 mHz; the low frequency peak might not be

fully captured since the lowest operating frequency of our system is 1 mHz. The sand sample imaginary conductivity at 1 mHz initially increased until time 72 hours (figure 5c) and after a small decrease, increased with a relatively slower trend until the end of the experiment (240 hours of injection). The 10 mHz peak behaved differently with maintaining a relatively constant value toward the end of the experiment (figure 5d). The sand + clay sample showed an initial increase until time 120 hours (figure 5a) and after a decrease, reached a constant value (at both 1 Hz and 1 mHz) until the end of the experiment (Figure 3.5b).

The most dominant changes occur around 1 Hz and 1 mHz; for both active columns, where the same spectral and temporal behavior are observed (Figure 3.5 and Figure 3.6). In contrast, the control column does not show any noticeable changes (Figure 3.6a and b). Although the observed trends are relatively similar for both samples, the magnitude of the observed change is greater, and with earlier peak response, for the sand only column (Figure 3.6a).

Based on the imaginary conductivity trend (Figure 3.5 and Figure 3.6) we identified three different stages in the experimental progress, interpreted to be associated with calcite precipitation. Stage one represents background conditions with no calcite precipitation. Stage two occurs during the initial calcite addition with increasing precipitation and primarily occurs in the form of fine mineralization and subsequent aging primarily with increasing crystal growth. During stage three steady state is reached as the amount of calcite occurrence equals the amount of calcite precipitating as it is flushed due to flow or clogged pores, which prevents further mixing of the 2 solutions [see discussion for details].

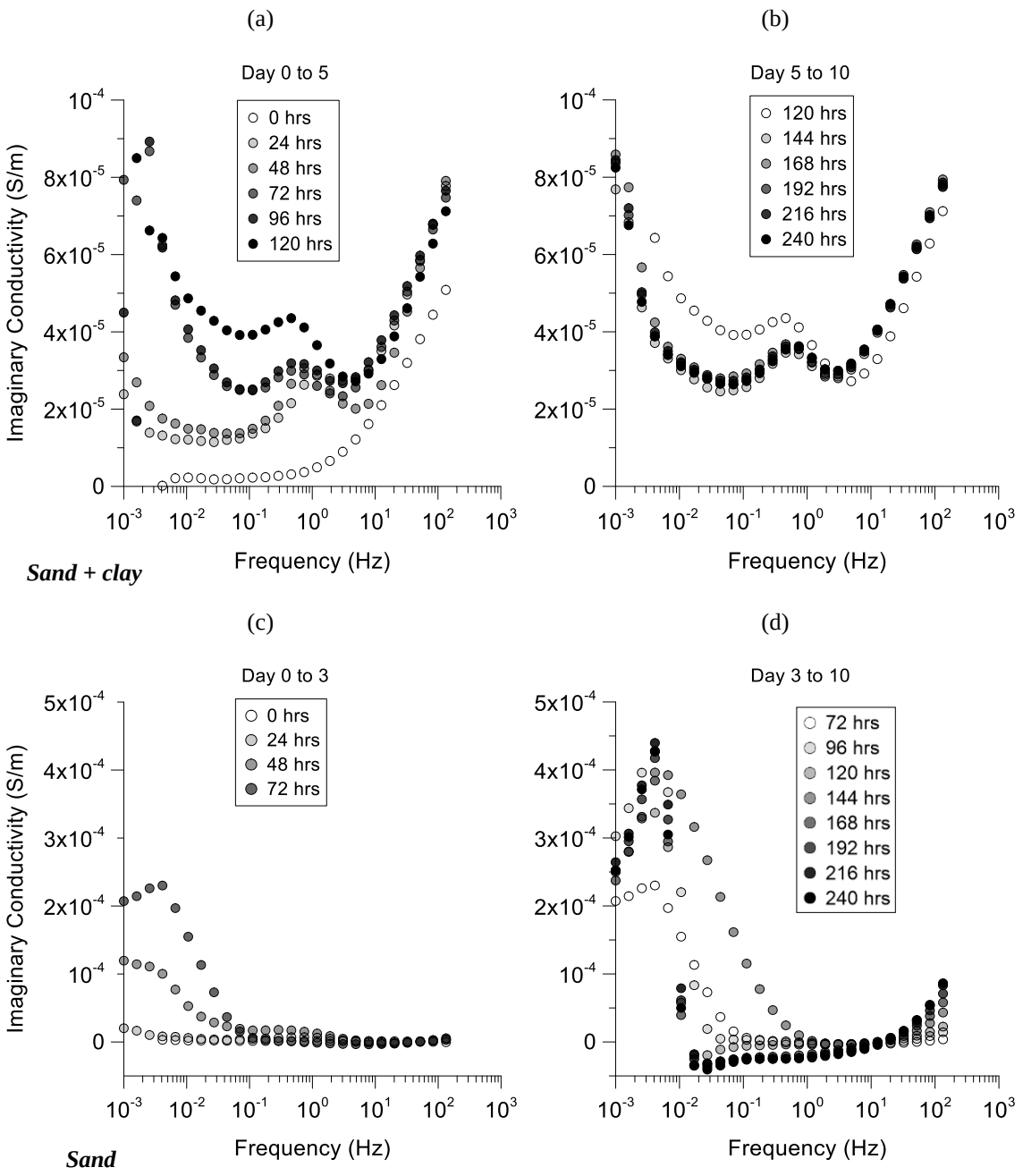

Figure 3.5: Imaginary conductivity spectra , time = 0 hrs represents the background signal (prior to injection), (a) Initial increase phase for sand + clay sample, (b) late decrease and equilibrate phase for sand + clay sample, (c) Initial increase phase for sand sample, (d) late decrease and equilibrate phase for sand sample

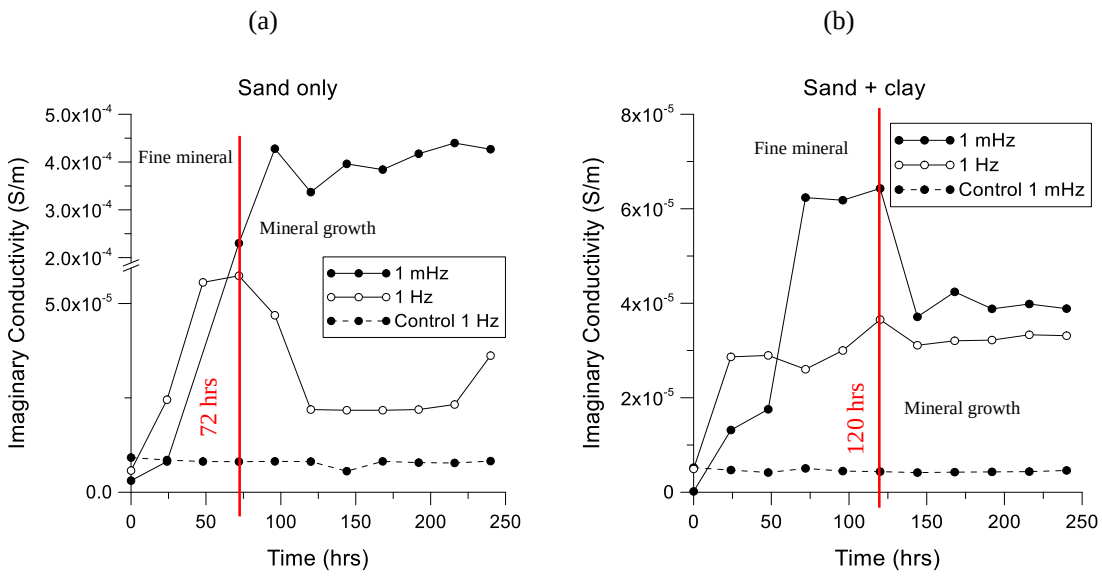

Figure 3.6: Imaginary conductivity behavior over time for two active and one control columns at two distinctive frequencies, time = 0 hrs represents the background signal (prior to injection) – red line separates the fine mineral formation stage from mineral growth stage, (a) Sand only sample, (b) Sand + clay sample

We used empirical DD models to processes all the complex conductivity data; the model fits the measured data very well (Figure 3.7b and Figure 3.8b) except stage 3 for the sand only experiment (Figure 3.9b). The relaxation time distribution (RTD) peaks identified by DD show the development of unique and consistent peaks in response to calcite precipitation (Figure 3.8a and Figure 3.9a) as there is no such peaks in stage one (prior to injection, Figure 3.7a). The observed RTD peaks do not move over time, with only the magnitude of the peak changing, which suggests no change in the polarization mechanisms over time. The change in peak magnitude might be due to changes in the polarization mechanism relative intensity. DD revealed two relatively (to background) distinct RTD peaks for the sand + clay sample, at 3×10^{-1} and 3×10^{2} seconds (Figure 3.8a and Figure 3.9a, black line), similarly there are two large peaks in RTD for the sand sample at 30 and 3×10^{2} seconds (Figure 3.8a, blue line). No significant peaks were observed in the control column.

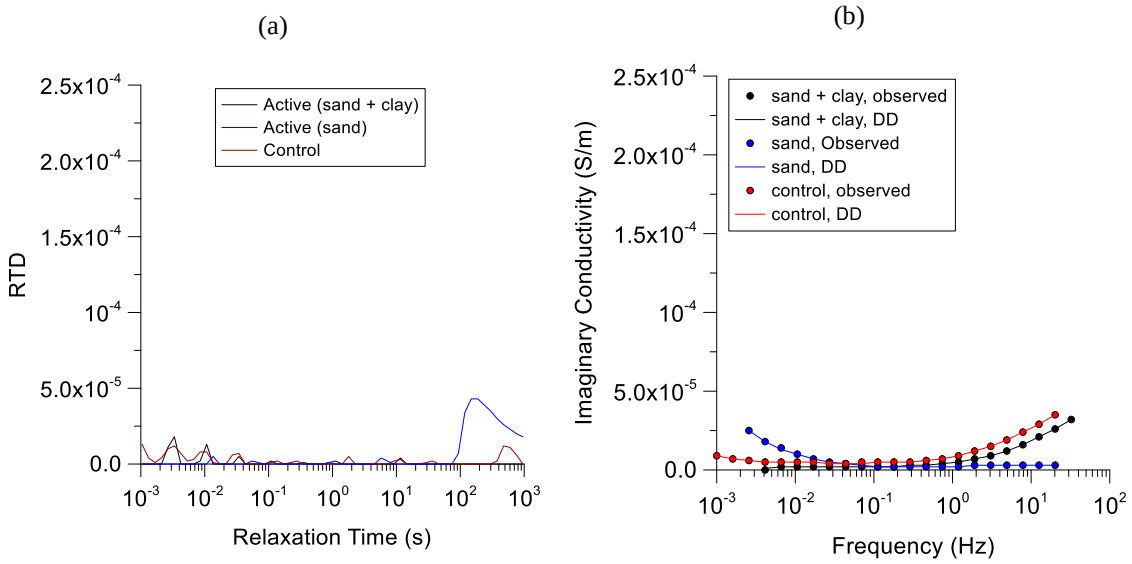

Figure 3.7: Debye Decomposition inversion at *stage one* (prior to injection), (a) RTD, (b) Imaginary conductivity observed (circles) and inverted (lines)

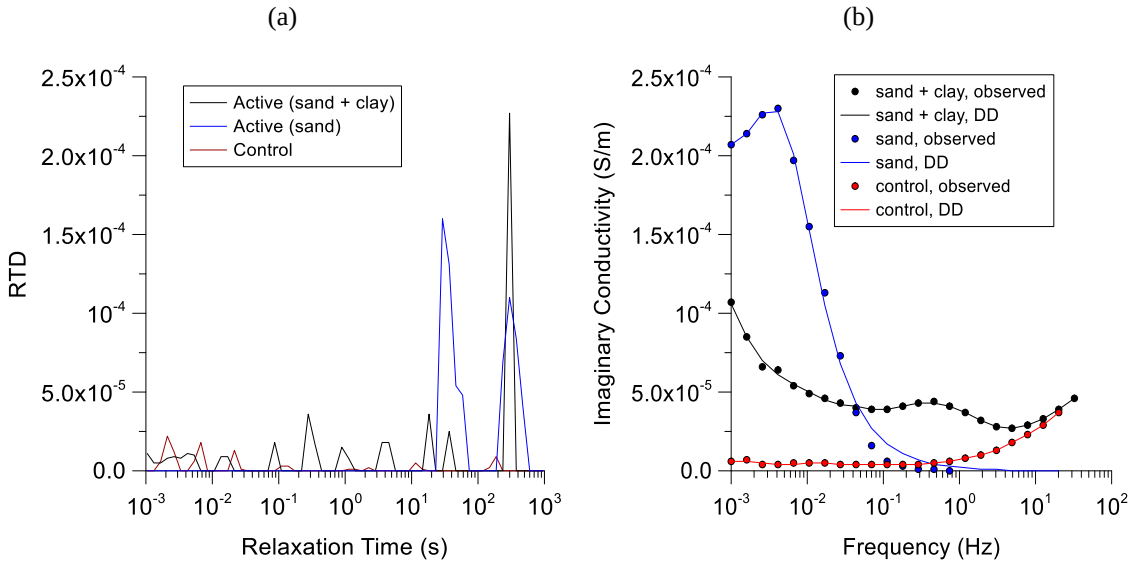

Figure 3.8: Debye Decomposition inversion at *stage two* (50% of the experiment injection period was done), (a) RTD, (b) Imaginary conductivity observed (circles) and inverted (lines)

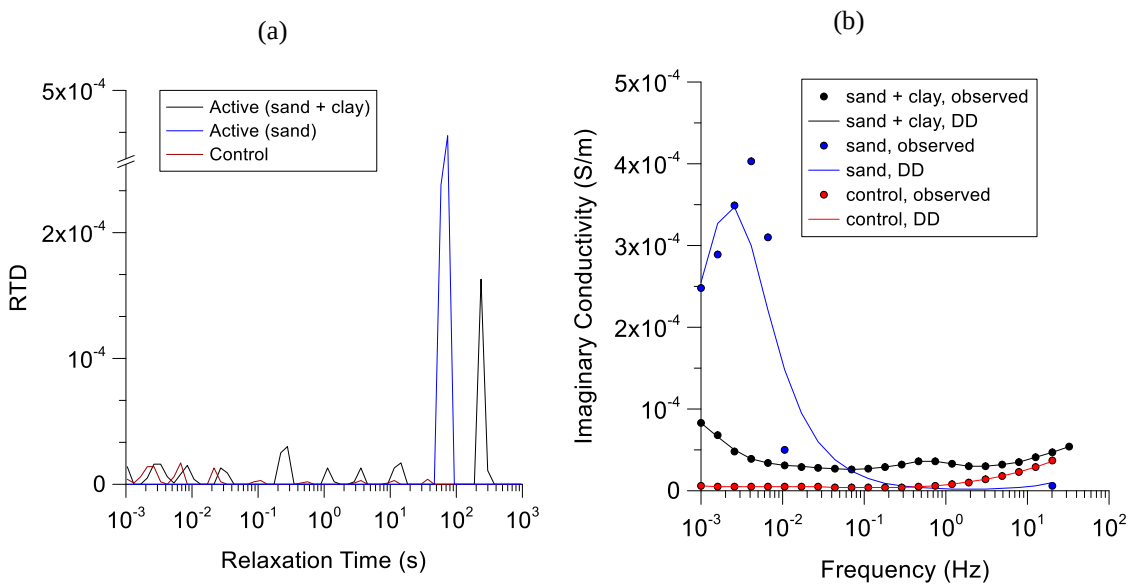

Figure 3.9: Debye Decomposition inversion at *stage three* (the end of the experiment), (a) RTD, (b) Imaginary conductivity observed (circles) and inverted (lines)

The changes in shear-wave velocity are shown in Figure 3.10. We used the first observed peak in each measurement as the first arrival signal, as highlighted by the red line (Figure 3.10a). The shear-wave velocity is increasing as the experiment progresses, presumably in response to calcite precipitation (Figure 3.10b). The data presented are only for the clay samples. Unfortunately, due to receiver malfunction in the control column, data collection was impossible, so we do not have any additional data for direct comparison. Also during the sand experiment (which preceded the clay experiment), we used a sub-optimal acquisition protocol that resulted in poor quality data.

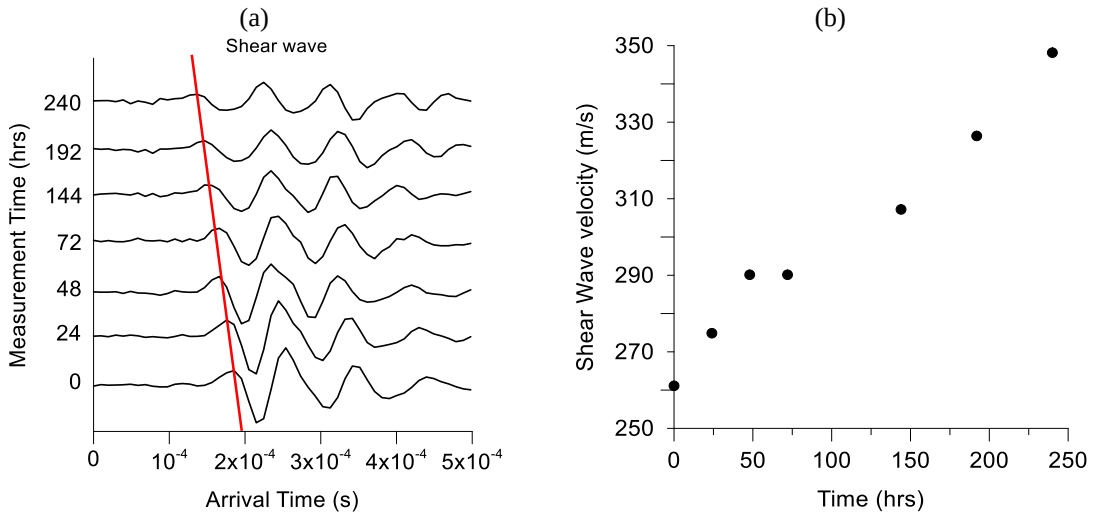

Figure 3.10: Shear-wave velocity measurement , time = 0 hrs represents the background signal (prior to injection), (a) Actual received wave forms (red line shows the first arrival peaks), (b) Shear-wave velocity (m/s) based on the identified first arrivals

At the end of the experiment all the columns underwent destructive sampling for SEM analysis. This SEM analysis confirmed calcite precipitation in the active columns, with clean round sand grains in the control columns, and (Figure 3.11a to c) and calcite precipitation on the active ones (Figure 3.11d to f).

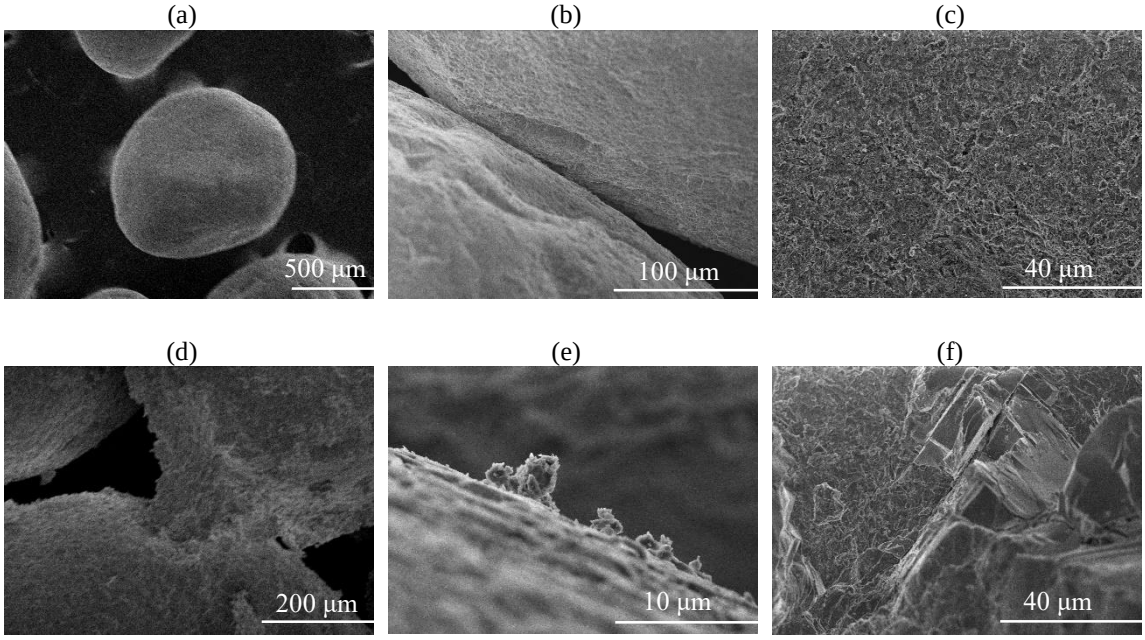

Figure 3.11: SEM imaging , (a, b, c) Control column, (d, e, f) Active columns

3.4 Discussion

Visual observations and destructive sampling confirmed that direct mixing of the two solutions, Na_2CO_3 and $CaCl_2$, induced calcite precipitation as expected (Figure 3.11). Changes in the geochemical properties of the fluid and the reduction in K further support successful calcite precipitation under the experimental conditions (Figure 3.4). ICP analysis on outflow solutions is also consistent with calcite precipitation since it shows reduction in dissolved calcium concentration. Based on the geochemical monitoring, and modeling (Table 3.1), it is safe to assume that calcite precipitation is the dominant process in these experiments.

The presence of kaolinite in the "sand + clay" samples appears to have affected the availability of calcium ion for calcite formation. The ~120 ppm difference in initial effluent concentration of dissolved calcium between 'sand only' and 'sand + clay 'samples (Figure 3.4c) along with the dramatic drop in the effluent dissolved calcium concentration within the first 24 hours of the experiment (Figure 3.4c), can be explained only with calcium sorption in kaolinite. In addition, the increase in effluent concentration of dissolved calcium in the sand + clay control column leads to the hypothesis that the clay structure is getting more and more saturated with calcium ions, hence more ions can reach the effluent. It is estimated that after 24 hours (Figure 3.4c), all the calcium in the solution was available for calcite formation since the decreased rate has significantly slowed down (showing similar behavior as the "sand only" column ~75 hrs).

Calcite precipitation appears to have had a significant effect on geophysical signatures. The SIP and shear-wave measurements both showed changes as the calcite precipitation was progressing. Imaginary conductivity, heavily dependent on interfacial

properties, appears to be an accurate marker of the calcite formation process. As discussed earlier, the magnitude of the signal and the signal shape changed over time. For both experiments, the imaginary conductivity trends are similar but vary in absolute magnitude, possibly due to calcium availability as a result of the interaction with kaolinite clay. The similar imaginary conductivity trends (Figure 3.5) suggest the same dominant polarization mechanisms. This interpretation further supports that calcium availability, hence calcite precipitation, controls the signal magnitude. DD modeling is in direct agreement with this interpretation, suggesting that the dominant polarization processes are the same in all experiments, but vary in contribution.

The observed imaginary conductivity responses seem to track calcium carbonate precipitation progress in response to the mixing of the 2 injected fluids. Upon injection and subsequent mixing, calcite precipitates almost instantly and continues for the duration of the mixing. Carbonate precipitation due to mixing of highly concentrated solutions typically leads to the formation of isolated micro/nanometric crystals, or spherical/spheroidal aggregates and under lower concentrations carbonate minerals tend to grow on pre-existing surfaces as layers (laminae) [*Van Driessche et al.*, 2017]. Imaginary conductivity is in direct agreement with this precipitation model. The 1 Hz data, representative of finer mineral grains, show that the new mineral phase forms at a higher rate in the early times of the experiment for the ‘sand-only’ column, as expected due to the increased availability of Ca, and then it reaches a steady state, as the column is Ca saturated. Conversely, the ‘clay-sand’ column exhibits different behavior, due to the calcium limitations previously described, and reaches a steady state earlier (Figure 3.6). Changes in the 1 Hz data should reflect the amount of fine calcite present in the columns. The 1

mHz data can offer additional insight on calcite forming progress, since these data are sensitive to the presence of larger mineral grains. Since we established that the only process in our system is calcite formation, the lower frequency data suggest the formation of larger grains, or more accurately, the growth of existing grains due to the accumulation or addition of new layers. Broad spectrum SIP imaging appears to reveal the complete calcite precipitation story, with information not only on the precipitation process, but also on the calcite growth progress.

Shear-wave velocity measurements are in agreement with calcite precipitation and suggest increased soil stiffness (Figure 3.10). Although both SIP and shear-wave measurement show that calcite is precipitating, the observed trends are different. Shear wave velocity keeps increasing, suggesting increasing stiffness with continuous fluid mixing. On the other hand, SIP reaches an early peak, followed by a small decline before reaching steady state conditions. Although seemingly different, the SIP trend supports continuous increasing stiffness. It is known SIP is sensitive to available surface area per pore volume. Due to the onset of calcite precipitation, the available surface area per volume rapidly increases up to a threshold value. Further precipitation begins to limit available surface area due to coagulation or pore blockage, until equilibrium is achieved. Furthermore, it is important to note that precipitation stage 2 has significantly higher SIP magnitude than pre-injection conditions (Figure 3.12), suggesting that calcite is present and stable in the porous media. This observation could lead to the assumption that SIP is more sensitive to the cementation process and new mineral phase evolution.

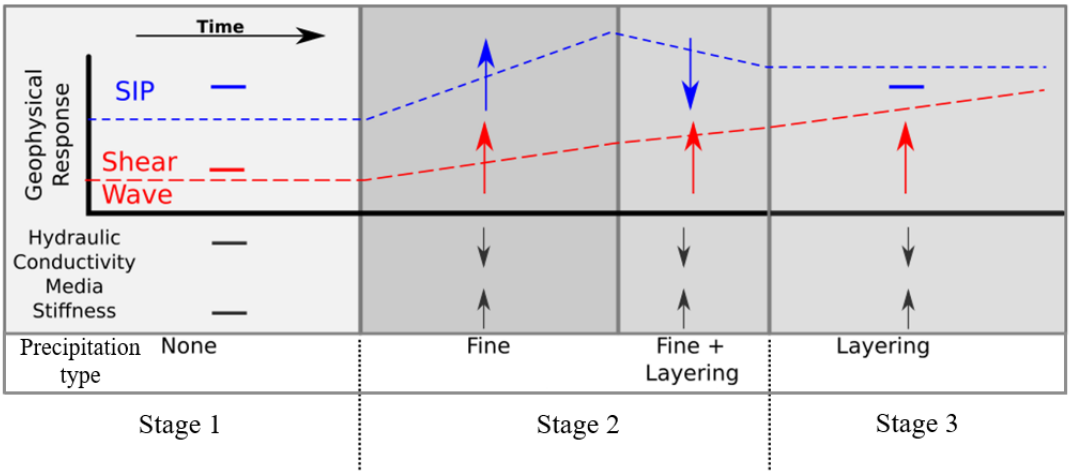

Figure 3.12: Mineralization mechanism stages with arrows depicting increasing or decreasing measured parameter per carbonate precipitation stage. Stage 1: Background, no calcite precipitation. Stage 2: Increased precipitation, increased crystallization, σ'' increases to threshold value, shear-wave velocity increasing. Stage 3: Steady state conditions.

Empirical models, such as DD, can be used to provide additional insight into the geophysical signal sources [*Weigand and Kemna*, 2016]. The DD based RTD approach used in our study further supports the development of two distinct polarization mechanisms – early time fine mineral precipitation, followed by late time mineral grain growth/layering – as a result of our experimental processes (Figure 3.8a and Figure 3.9a). The two processes seem to be complimentary and could be present in parallel; but each process is dominant during different stages of the experiment. A comparison between Figure 3.8a and Figure 3.9a for the sand sample (blue line) shows the observed peak at 3×10^2 seconds for the middle injection stage (stage 2) is eliminated at stage two (the end of the experiment). This may be due to changes in the calcite formation type from initially powder form (fine structure), to a layered structure toward the end.

Furthermore, since the effluent properties (e.g., fluid conductivity) showed a stable trend shortly after the injection started, we assumed the electrolyte in the pore space is not changing significantly; therefore, the charge density, mobility, and thickness at the EDL,

which is mostly controlled by pore fluid properties [*Wu et al.*, 2010], will not be changed toward the end of the experiment. Hence, we are assuming the only parameter that controls the polarization within our samples would be the surface area changes due to precipitation of the calcite within the pore space.

The main finding of our results is that joint shear wave and SIP measurements can provide comprehensive monitoring of calcite precipitation monitoring. Geophysical monitoring not only provides information on the overall stiffness, permeability, and porosity of the porous media, but also provides detailed information on the calcite forming stages.

This study conclusively shows that SIP is sensitive to calcite precipitation processes and can be used as a soil strengthening characterization tool. Furthermore, the ability to distinguish between different forms of calcite precipitation renders SIP as a promising monitoring tool. The monitoring capability of SIP could be especially beneficial for MICP field implementations where continuous long term assessment of the microbial performance on calcite formation is essential. However, further studies are required to investigate the efficiency of SIP in monitoring MICP processes, especially under complex field scale conditions.

3.5 Conclusion

The abiotic experiment on calcite precipitation as a cementing agent for soil strengthening, permeability, and porosity alterations clearly shows that SIP measurements can be an effective monitoring tool. SIP is sensitive to the calcite precipitation as well as aging and growth processes. SIP measurements are in direct agreement with shear-wave

velocity, showing increased stiffness as precipitation progresses. Although both methods showed calcite is acting as a cementation agent, different types of information can be retrieved from each method since they respond to different physical properties. This idea could highlight that carbonate precipitation changes both the electrical and mechanical properties of the media as realized through the SIP and shear-wave measurements. This study provides the basis needed for a fundamental understanding of calcite based cementing processes and the use of geophysical monitoring for studying MICP in field and laboratory experiments whether the objective is to stiffen soil or reduce permeability for subsurface fluid flow alterations. SIP and shear-wave velocity measurements both are expected to be efficient non-destructive and indirect measurement for future MICP processes related to engineering or environmental purposes. Further experimentation of increasing complexity and field measurements are required to realize the full applicability and potential of geophysical measurements to achieve these ends.

Acknowledgements

Special thanks to Dr. Ashaki Rouff for providing us the opportunity to use ICP-OES device in her laboratory at Rutgers University – Newark (NSF grant #1530582). This project was funded by National Science Foundation grant #1363224. The views expressed in this article are those of the authors and do not necessarily represent the views or policies of the U.S. Environmental Protection Agency. This document has been reviewed by the U.S. Environmental Protection Agency, Office of Research and Development, and approved for publication. Any mention of trade names, products, or services does not imply an endorsement by the U.S. Government or the U.S. Environmental Protection Agency. The EPA does not endorse any commercial products, services, or enterprises.

Chapter 4: Induced polarization as a monitoring tool for in-situ microbial induced carbonate precipitation (MICP) processes[1]

Abstract

Microbial induced carbonate precipitation (MICP) is a promising soil stabilization method performed by stimulating soil microbes that are naturally occurring and ubiquitous in soil systems. The precipitated carbonate acts as a cementation agent to bind loose soil at grain to grain contacts. MICP has been extensively tested and proven in laboratory environments, as well as in limited field trials; however, long term field applications still remain challenging, partly due to quality control and monitoring issues. Induced polarization (IP), an established geophysical method in mineral exploration, is a prime candidate for MICP monitoring and characterization. This study presents the geophysical results of a 15-day field-scale MICP project. The MICP treatment involved the injection of molasses (carbon source for microbial proliferation) and urea in a Ca^{2+} rich aquifer. IP monitoring successfully delineated, spatially and temporally, the propagation of MICP in the treatment area, while common resistivity measurements failed to capture any MICP related changes. Reduced hydraulic conductivity in the treatment area versus untreated area, further supports that MICP has changed the physical properties of the subsurface. Furthermore, conventional geochemical monitoring as well as X-ray diffraction analysis confirmed carbonate precipitation in samples from discrete wells in the treatment area.

[1] This chapter is published as: Saneiyan, S., D. Ntarlagiannis, J. Ohan, J. Lee, F. Colwell, and S. Burns (2019), Induced polarization as a monitoring tool for in-situ microbial induced carbonate precipitation (MICP) processes, Ecol. Eng., 127, 36–47

4.1 Introduction

Development in densely populated urban environments has often resulted in construction of infrastructure on deposits of loose, saturated sands, which are prone to liquefaction during dynamic loading, such as earthquakes. Collapse of the soil's pore space during a seismic event or other anthropogenic loadings (e.g., blasting) results in degradation of soil fabric, causing surface settlement or other engineering problems [*DeJong et al.*, 2010, 2013]. Ground improvement (soil stabilization) projects aim at enhancing the properties of the subsurface (e.g., strength, stiffness, or hydraulic conductivity) for a variety of purposes such as crack remediation and permeability reduction [*Abo-El-Enein and Ali*, 2012], erosion prevention and dust control [*Montoya et al.*, 2013], as well as infrastructure supporting foundations [*DeJong et al.*, 2010].

Common ground improvement techniques utilize either mechanical methods (e.g., deep dynamic compaction) or chemical grout injections. In large areas, mechanical methods can consume significant energy and are not always feasible. Chemical grouting can overcome the energy consumption problem of the mechanical methods; however, these materials (e.g., cement, epoxy, acrylamide, phenoplasts, polyurethane, and glass water) can be harmful to the environment and human health [*Worrell et al.*, 2001; *Karol*, 2003; *Chang et al.*, 2015; *Wang et al.*, 2017]. Furthermore, chemical methods are expensive, difficult to apply homogenously and create permanent changes to the soil properties due to their synthetic nature [*DeJong et al.*, 2006]. Additionally, the most common ground improvement methods (e.g., deep dynamic compaction) are impossible to apply in heavily developed areas with buildings and infrastructure already in place [*Burbank et al.*, 2013].

In recent years, multidisciplinary research showed the potential of microbial induced carbonate precipitation (MICP) as an alternative ground improvement approach that offers enhanced soil stability, without the issues common methods face [*Gomez et al.*, 2015; *Wang et al.*, 2017]. MICP can be cost efficient, environmentally friendly, suitable for long term applications and can be applied in areas with existing infrastructure [*Ivanov and Chu*, 2008; *Burbank et al.*, 2013; *Anbu et al.*, 2016].

MICP results in the biomineralization of carbonates (mainly calcite), with calcite acting as a cementation agent for binding soil grains [*Dhami et al.*, 2013]. Biomineralization is a naturally occurring process and MICP stimulates the in situ microbes, resulting in the precipitation of calcite through urea decomposition by soil borne microbes [*Burbank et al.*, 2012; *Gat et al.*, 2014]. MICP requires less chemical injection and is energy efficient due to incorporating low/no mechanical energy. Finally, MICP is non-disruptive to existing structures and is suitable for large-area applications [*DeJong et al.*, 2010, 2013].

4.1.1 Monitoring MICP process

Various methods are discussed in literature for monitoring the MICP processes (e.g., *Anderson et al.*, 2003; *Mitchell and Santamarina*, 2005; *Dejong et al.*, 2006; *Rodriguez-Navarro et al.*, 2012; *Gomez et al.*, 2015), and they can be categorized as being direct and indirect methods. Direct monitoring methods (e.g., chemical analysis, X-ray diffraction, microbial analysis, triaxial load test, etc.) are known to be accurate techniques. However, these methods are typically invasive because they require sampling, and are spatially limited, labor intensive, expensive, and incapable of real-time monitoring. Indirect monitoring techniques (e.g., geophysical methods) on the other hand, are

noninvasive and cost efficient methods that can deliver high temporal and spatial subsurface imaging [*Weil et al.,* 2012]. The main disadvantage of geophysical monitoring can be limited accuracy, true for every indirect method, and erroneous data interpretation that are typically associated with the user/operator (examples of common errors are poor survey configuration, survey systematic errors, erroneous data processing, over interpretation, etc.) [*Maclennan,* 2013]. The ideal monitoring approach should utilize both indirect and direct methods, the former for continuous high resolution monitoring and the latter for selective, high accuracy, ground-truthing.

Geophysical methods have been widely used in the recent past to enhance the reliability and efficiency of geotechnical projects [*Anderson et al.*, 2008; *Arjwech and Everett*, 2015]. For this project we focus on the use of induced polarization (IP), an emerging geophysical method on environmental applications, to evaluate the progress of MICP at a field site. IP is a well-established method in the mineral exploration industry [*Moon et al.*, 2006] and is increasingly being used for near surface environmental applications (e.g., *Williams et al.*, 2009; *Flores Orozco et al.*, 2012; *Ntarlagiannis et al.*, 2016). We consider IP an important method for MICP projects because it is sensitive to carbonate formation and dissolution [*Saneiyan et al.*, 2018], and also can be used for autonomous long term monitoring – a characteristic crucial for successful soil stabilization efforts that is currently not being offered by any other methods. Additionally, we had the opportunity to briefly utilize another emerging environmental geophysical method, nuclear magnetic resonance (NMR), which is sensitive to water content and pore geometry in earth media [*Walsh et al.*, 2013] and conceptually can be diagnostic for MICP processes [*Saneiyan et al.*, 2018]. Although we have a very limited NMR dataset (logistical problems

prevented us from using the NMR tool for the duration of the experiment), we believe that the presentation of the results is important due the significant potential NMR holds for future MICP applications. With this paper, we focus on the IP results of this unpreceded field scale experiment, and discuss the suitability of the method as a long term monitoring aid for MICP projects.

4.2 Study site description

The Rifle Integrated Field Research Challenge (IFRC) site is a decommissioned vanadium and uranium processing facility field located 0.3 miles southeast of the city of Rifle, Colorado [*U.S. Department of Energy*, 1999]. Previously, it was shown that MICP treatment can be successfully performed at this site due to abundant amounts of Ca^{2+} ions and necessary microbes in the aquifer [*Smith et al.*, 2012]. A 1.75 m engineered clay cap was compacted over alluvial sediments of the Colorado River's riverbank as a part of site remediation during 1990s. The average depth of groundwater at this site is about 3.5 m below ground surface (bgs). At the depth of 6.1 m bgs, an impermeable layer of the Wasatch formation is present [*U.S. Department of Energy*, 1999; *Anderson et al.*, 2003; *Flores Orozco et al.*, 2011; *Fox et al.*, 2012]. In 2012 an array of cased and open observation wells was installed at plot B (Figure 4.1a) [*Fox et al.*, 2012] to allow direct injection and sample withdrawal from the aquifer at depths of 3.66, 4.57, 5.49, 6.4, 7.3, and 7.62 m bgs. Open wells had a diameter of 10.2 cm, wide enough for inserting borehole geophysical instruments. For this study, we used cased wells 12, 13 and 14 for injection and wells 25 and 26 for withdrawal; samples for geochemical analysis were collected from wells 1, 2, 3, 4, 25 and 26 (Figure 4.1b). In open well 1, we introduced artificial substrate core samples (ASCs) made from coarse grain Colorado silica sand mixed with archived

sediment from the IFRC site at a 1:1 ratio by volume and packed into slotted PVC pipes. These introduced core samples remained in the well (to undergo similar processes with the surrounding environment) until the end of the study after which X-ray diffraction was used to determine whether calcite was present or not.

4.3 Material and methods

4.3.1 Chemical and microbiological processes

MICP is the result of microbial activity in subsurface. The process involves the microbially mediated production of CO_2 as well as the products of urea decomposition (ureolysis), which include NH_4^+. *Sporosarcina pasteurii* (formerly known as *Bacillus pasteurii*), an aerobic, naturally occurring bacterium in soils, is commonly utilized in MICP projects [*DeJong et al.*, 2006; *Anbu et al.*, 2016]. During MICP, *S. pasteurii* will decompose urea (Equation 4.1) and in presence of Ca^{2+} ions, calcite will precipitate (Equation 4.6) [*DeJong et al.*, 2010; *Burbank et al.*, 2011, 2013; *Dhami et al.*, 2013; *Wang et al.*, 2017].

$$NH_2\text{-}CO\text{-}NH_2 + 3H_2O \rightarrow NH_2COOH + NH_3 \quad (4.1)$$

$$NH_2COOH + H_2O \rightarrow H_2CO_3 + NH_3 \quad (4.2)$$

$$H_2CO_3 \leftrightarrow HCO_3^- + H^+ \quad (4.3)$$

$$2NH_3 + 2H_2O \leftrightarrow 2NH_4^+ + 2OH^- \quad (4.4)$$

$$HCO_3^- + H^+ + 2OH^- \leftrightarrow CO_3^{2-} + 2H_2O \quad (4.5)$$

$$Ca^{2+} + HCO_3^- + OH^- \rightarrow CaCO_3 \downarrow + H_2O \quad (4.6)$$

$$Ca^{2+} + \text{microbial cell} \rightarrow \text{Cell-}Ca^{2+} \quad (4.7)$$

$$\text{Cell-}Ca^{2+} + CO^{3-} \rightarrow \text{Cell-}CaCO_3 \downarrow \quad (4.8)$$

(a)

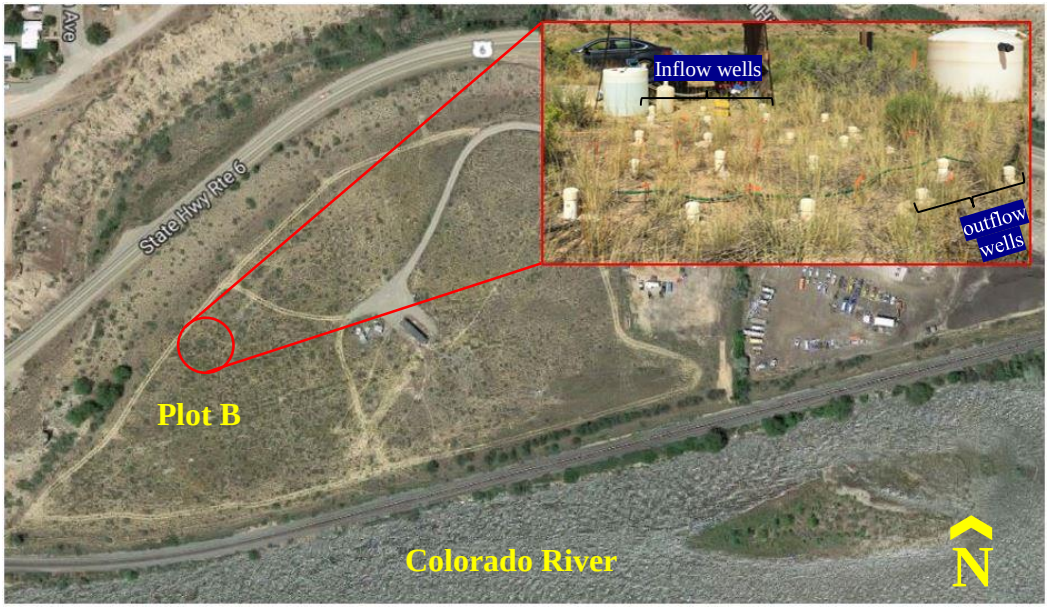

(b)

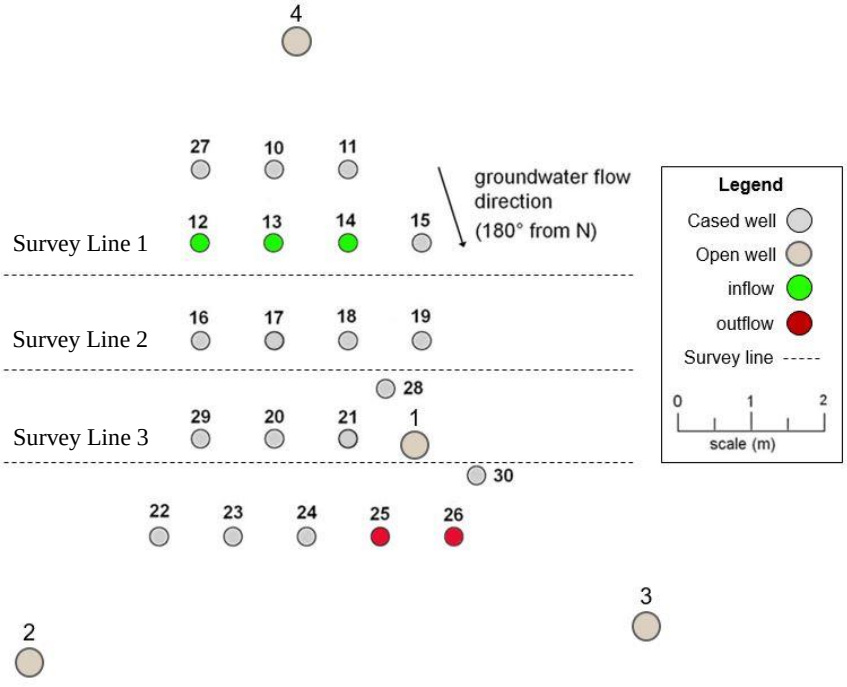

Figure 4.1: Study site. (a) The IFRC at Rifle, CO. Top right inset, view of existing wells used in this study, (b) schematic of existing wells at plot B of the IFRC and used during this project. Survey lines are clipped horizontally for simplicity.

If the concentration of Ca^{2+} is sufficient in solution, Ca^{2+} ions will attach to microbial cells (Equation 4.7) and in presence of CO_3^{2-} ions (Equation 4.5), calcite precipitation will also occur at the surface of microbial cells (Equation 4.8) [*Anbu et al.*, 2016]. The general distribution of microbial cells in the saturated, shallow subsurface environments and the common occurrence of ureolytic microbes in aquifers [*Smith et al.*, 2012] leads to calcite precipitation when native microbes are properly stimulated [*Boquet et al.*, 1973; *Mitchell and Santamarina*, 2005; *Al Qabany et al.*, 2012; *Ng et al.*, 2012]. Additionally, with the mentioned parallel path ways of calcite precipitation (Equation 4.6 and 4.8), MICP generally results in a more homogenous spatial distribution of calcite precipitation inside the porous medium [*Cheng and Cord-Ruwisch*, 2012] compared to chemical induced calcite precipitation.

4.3.2 Geophysical monitoring

4.3.2.1 Induced polarization

In most soils, where metallic minerals are not present, electrical current travels in the subsurface through electrolytic (σ_{ele}) and surface (σ_{surf}) conduction (Equation 4.9) [*Waxman and Smits*, 1968; *Slater and Lesmes*, 2002]. Both electrolytic and surface conduction pathways are ionic, the former through the fluids in the interconnected pore space, and the latter through the electrical double layer (EDL) at the available matrix-fluid interfaces [*Binley and Kemna*, 2005]. σ_{ele} is controlled solely by fluid properties, while σ_{surf} is a complex property dependent on surface properties (e.g., surface area, pore size distribution, surface charge density) and to a lesser degree on fluid properties [*Lesmes and Frye*, 2001; *Binley and Kemna*, 2005; *Weller et al.*, 2013]. These two conduction pathways are commonly modeled to act in parallel for simplicity [*Waxman and Smits*, 1968; *Lesmes*

and Frye, 2001]. The real component (σ') of the complex conductivity (σ^*) represents electromigration in subsurface, while the imaginary one (σ'') represents charge polarization (Equation 4.9). The common geophysical method, electrical resistivity imaging (ERI), measures only the real component while the induced polarization (IP) method, which can be considered an extension of ERI, allows the measurement of the complex electrical properties of the subsurface. The measured parameters in frequency domain measurements are conductivity magnitude ($|\sigma|$) and phase angle (ϕ); the complex parameters are then calculated using equation 9:

$$\sigma^* = \sigma' + i\sigma'' = |\sigma|e^{i\phi} \tag{4.9}$$

where $i = \sqrt{-1}$. Most commonly though, field IP measurements are performed in the time domain and the parameters measured are the resistance magnitude (R) and the apparent chargeability (m_a) (Equation 4.10):

$$M_a = \frac{V_s}{V_p} \tag{4.10}$$

where m_a is chargeability at time t, V_s is the measured secondary voltage at time t after current shut-off and V_p is the primary voltage (current is on). It is important to highlight that V_s is measurable only when subsurface polarization mechanisms are significant. Since V_s is small relative to V_p we measure an integral of m_a (Equation 4.11) over a decay curve for a certain time (t) after the current injection is turned off:

$$m_a = \frac{1}{(t_2 - t_1)} \frac{1}{V_p} \int_{t_1}^{t_2} V(t)dt \tag{4.11}$$

At low frequencies (below 10Hz), the measured IP parameters in the frequency (ϕ) and time (m_a) domains are proportional since they both describe the polarization relative to electromigration (Equation 4.12) [*Van Voorhis et al.*, 1973; *Slater and Lesmes*, 2002]:

$$m_a = -\kappa \phi \tag{4.12}$$

where κ is a proportionality constant and can be experimentally derived.

4.3.2.2 Borehole nuclear magnetic resonance

Nuclear magnetic resonance (NMR) is a well-established method in the oil industry to obtain permeability of the subsurface. Recently, the method has been used in near-surface applications for hydrological and environmental applications (e.g., measuring subsurface hydraulic conductivity, water content, pore size distribution, etc.) [*Dlubac et al.*, 2013; *Walsh et al.*, 2013]. In this method, a static magnetic signal will be transmitted into the ground resulting in polarization of hydrogen atoms in the parallel to the emitted magnetic field. Then, a relaxation decay time (T_2) will be measured (when the static magnetic field is extinguished) which is the time for polarized atoms to return to their natural state. In saturated zones (below water table), T_2 distribution reflects the water-filled porosity (φ). Generally, larger pores result in longer relaxation times and smaller pores will have shorter observed relaxation times in the NMR measurements. Then, hydraulic conductivity (K) can be derived from various empirical equations (e.g., equation 4.13) [*Walsh et al.*, 2013; *Knight et al.*, 2016].

$$K_{NMR} = b\, \varphi^{m} (T_{2ML})^2 \quad [m/day] \tag{4.13}$$

where K_{NMR} is the hydraulic conductivity, φ is NMR determined porosity, T_{2ML} is the arithmetic mean of log T_2, b and m are empirically determined constants.

4.3.3 Experiment setup and procedure

According to *Whiffin et al.*, (2007), laboratory bio-cementation experiments have four successive stages: (1) initial water flush - to rinse the soil, (2) microbial injection, (3) reaction fluid injection - to initiate cementation immediately after microbial injection, following by a no-flow reaction period, (4) final rinse - to flush the microbes out. Furthermore, effective cementation occurs at higher concentration of initial solutions (e.g., higher concentrations of urea) [*DeJong et al.*, 2006; *Burbank et al.*, 2011; *Anbu et al.*, 2016].

In this study, we designed the following steps to conduct a field scale MICP project:

(1) injecting the needed nutrients (360 liters of 0.13 g sugarcane molasses/L, Figure 4.1b) to stimulate the ureolytic microbes known to exist at the IFRC site [*Fox et al.*, 2012],
(2) microbial growth period (24 hours),
(3) urea injection (360 liters – Day 2 to 4: 0.5 g urea/L, Day 8 to 14: 7.78 g urea/L) to promote calcite bio-mineralization,
(4) groundwater pumping from downgradient well(s) (Figure 4.1b) to support the preferential flow path, and collect fluid samples for geochemical monitoring.

For all injections, we combined extracted groundwater from the site with the needed urea and/or molasses. For the duration of the experiment, solution samples were collected at downgradient wells (25, 26), middle wells (18 and 1), and one upgradient well 4 (Figure 4.1b) and analyzed for ammonia concentration (using 50mL solution samples, analyzed with commercially available colorimetric test kits – CHEMetrics V-200 photometer and Vacu-vials, at the filed laboratory) and changes in other physical and chemical properties (e.g., fluid conductivity, pH, dissolved oxygen, etc.) by using portable sample analyzers (e.g., Thermo Scientific, Orion 4 Star Plus) [*Ohan et al.*, 2017].

Surface electrical measurements (IP/resistivity) were made daily (15 days in total). Graphite electrodes were used for these measurements; prior to the field experiment we tested the use of both stainless steel and graphite electrodes and we found that graphite offers superior performance (consistent low contact resistances – below 2 kOhm, while stainless steel had larger variability) consistent with literature findings [*LaBrecque and Daily*, 2008; *Kemna et al.*, 2012]. We used 24 electrodes (1 m spacing) and extended the lines about 9 m off the treatment area (at each side) to ensure adequate imaging resolution. Three survey lines were utilized in this study to capture the MICP progress in subsurface in three different cross sections: near injection wells, in the middle of the plot and near the withdrawal wells (Figure 4.1b). A mixed survey array was utilized, offering high S/N and optimized for the multichannel instrument used (IRIS instruments Syscal Pro 48). For each dataset, we set the injection current period at 1 second and the stacking to minimum 2 and maximum 4, with 2% error threshold. Finally, we collected a complete reciprocal set of measurements for error analysis [*Koestel et al.*, 2008; *Robinson et al.*, 2012].

A single NMR measurement was collected for the treated (well 1) and untreated areas (wells 2 and 3) on day 7 (middle of the experiment) using the Javelin 350 tool (sensitive to water at a radius of about 7.5″) [*Walsh et al.*, 2013]. The data were used for the qualitative comparison of K in the treated versus untreated area.

Small (20 grams) destructive samples from middle of the ASCs (that were incubated in the wells for the duration of this study) were collected and dried in the oven for 48 hours. These coarse samples directly underwent X-ray diffraction (XRD) analysis to detect whether calcite was present in them or not. Control ASCs (not incubated in the

wells, preserved at -80°C before drying in the oven for XRD analysis) also underwent the same procedure.

4.4 Data processing

After data acquisition, the following processing steps were taken to prepare the data for inversion and analysis (Figure 4.2):

1) Initial filtering: removing duplicate measurements, nested measurements (potential electrode(s) placed between current electrodes), voltage overloads (>15000 *mV*), low current measurements (<10 *mA*), dummy measurements (added by the instrument for efficiency) and abnormal chargeability values for this field site (>20 *mV/V*).
2) Error analysis (explained in section 4.1).
3) Final filtering:
    a. removing individual measurements with >10% reciprocal error, and
    b. datasets with an insufficient number of measurements (total number of measurements after all filtering steps less than 60% of initial number of measurements, before all filters).

Processed data were inverted using CR2 (a complex conductivity inversion code developed by Dr. Andrew Binley) [*Binley and Kemna*, 2005]. To use CR2, time-domain chargeability values were converted to phase angle values. A linear relationship between chargeability and phase angle was calculated (e.q. 12) by assuming constant frequency phase angle response in time-domain IP measurements [*Marshallt and Madden*, 1959; *Seigle*, 1959; *Vinegar and Waxman*, 1984; *Kemna et al.*, 1997]. A factor 1.2 was used (based on the intrinsic features of the instrument and previous laboratory analysis) to convert chargeability into phase angle values; the conversion details are described in *Mwakanyamale et al.*, (2012).

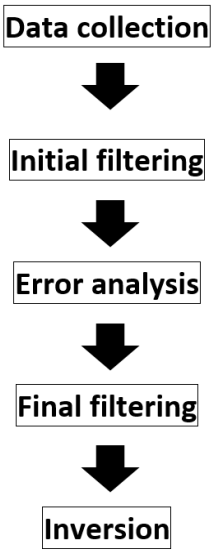

Figure 4.2: Flowchart of data collection, processing and inversion

4.4.1 Error analysis

Reciprocal measurements were carried out to estimate the appropriate data error models and calculate resistance and phase angle errors. For simplicity, the error models are presented only for 3 days (day 1/background, day 6/middle stage of the study and day 15/end of study) for each line (Figure 4.3 and Figure 4.4); all days showed similar error models.

Error models were calculated based on the multi-bin analysis (for more details of the method, see *Koestel et al.*, 2008; *Orozco et al.*, 2012). Equations 4.14 and 4.15 show the power law fits used for error models construction, based on the observed data distributions.

Resistance error model:

$$R_{error} = \alpha R_{avg}^{\beta} \; [ohm\ (\Omega)] \tag{4.14}$$

where: α and β are constants obtained from best fit,

$R_{error} = \left|R_{normal} - R_{reciprocal}\right|$ and $R_{avg} = \frac{R_{normal} - R_{reciprocal}}{2}$

Phase angle error model:

$$s(\phi) = aR^{b} \; [mRad] \tag{4.15}$$

where: *a* and *b* are constants obtained from best fit,

$s(\phi) = \left|\phi_{normal} - \phi_{reciprocal}\right|$ and $R = R_{normal}$

To illustrate the impact of filtering processes on data cleaning, measurements before and after all filtering steps are presented in Figure 4.5. Phase angle values are presented in plots of M (position number of the first potential electrode) versus A (position number of the first current electrode) for the first dipole-dipole skip in a 4 electrode (A-B/current pair, M-N/potential pair) measurement [*Orozco et al.*, 2013]. Days 1/background, 6/middle stage and 15/end of study were chosen for all 3 survey lines except day 1 for line 3, where no background data was available.

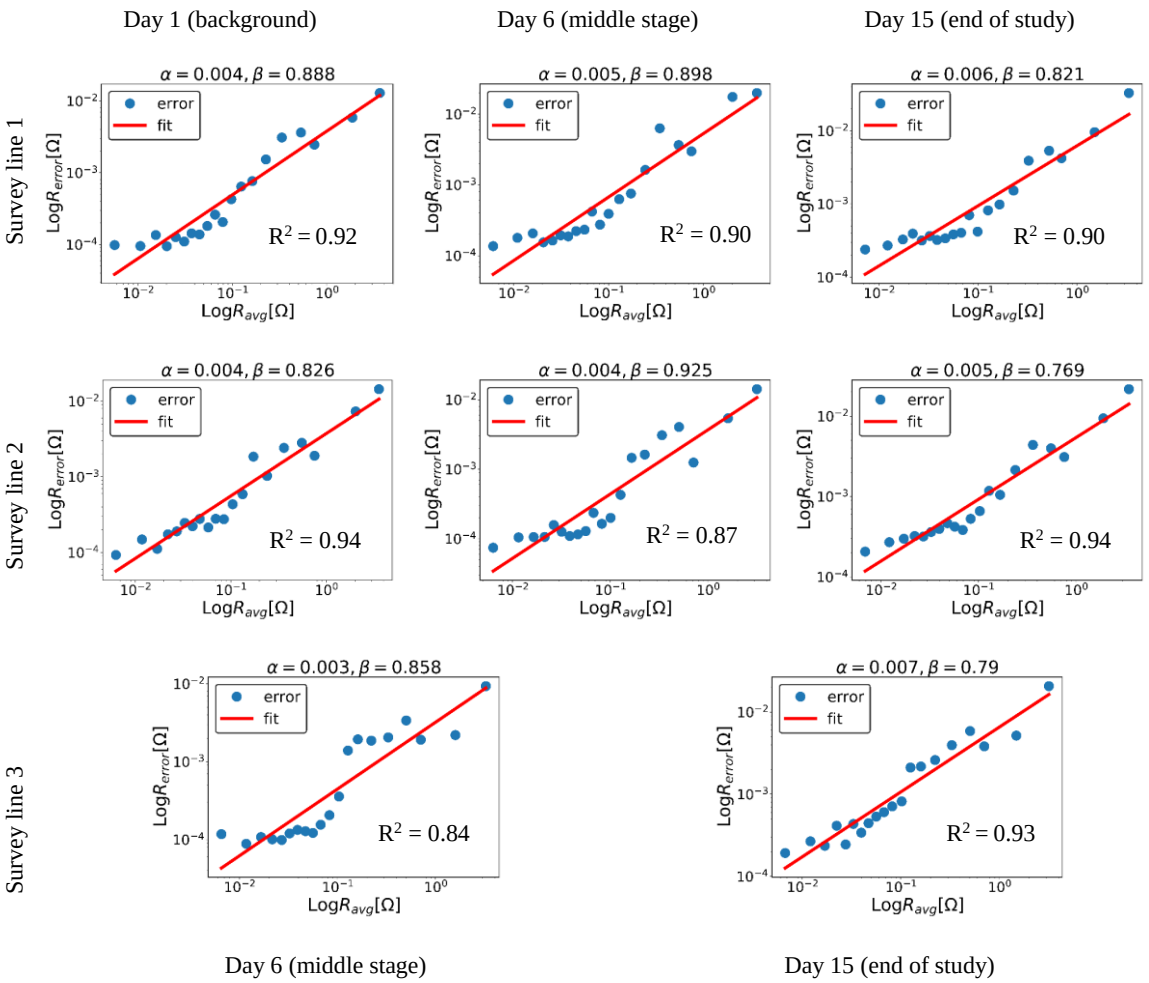

Figure 4.3: Power law resistance error model plots for the three survey lines. $R_{error}\ [\Omega] = \alpha R_{avg}^{\beta}$. Background data is not available for survey line 3

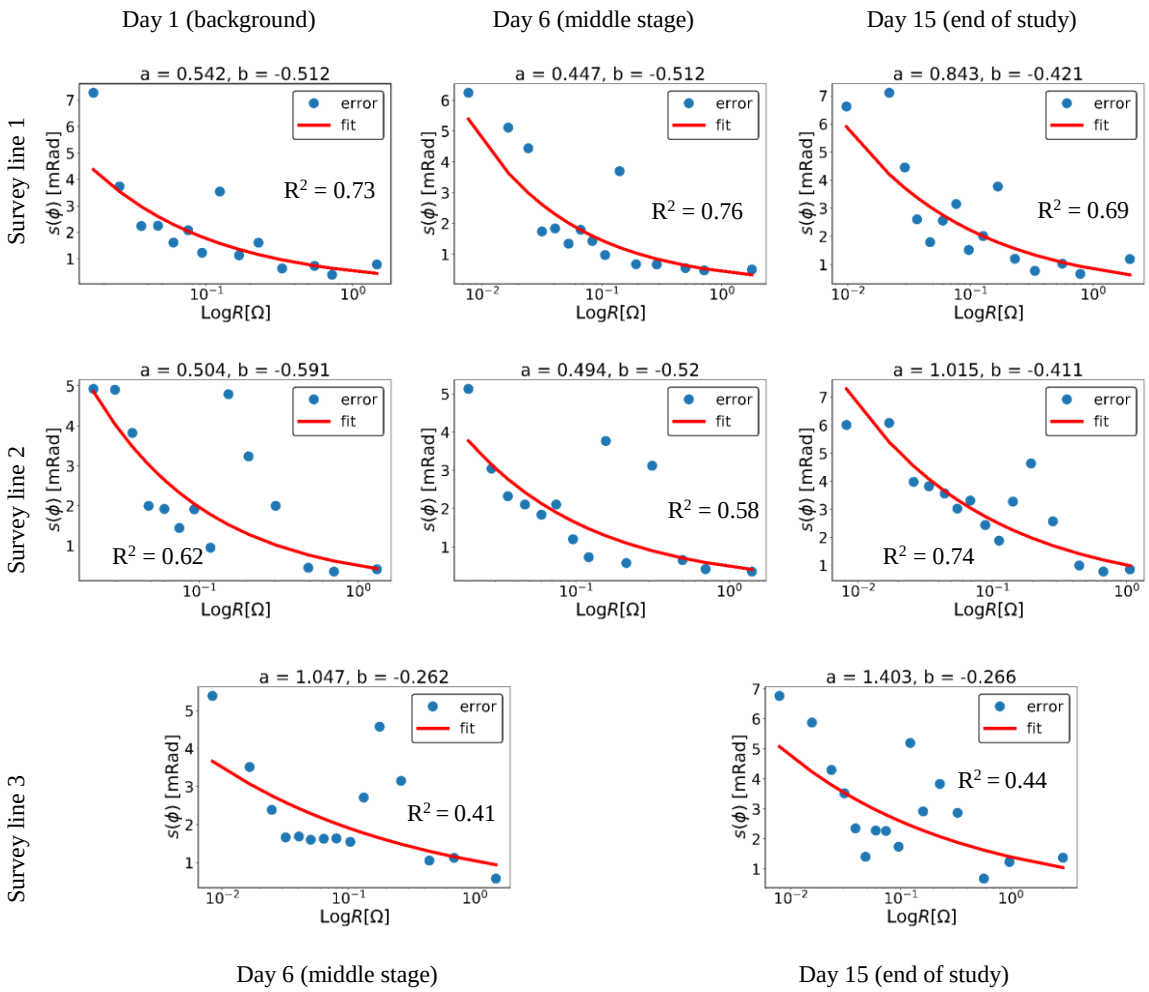

Figure 4.4: Power law phase angle error model plots for the three survey lines. $s(\phi)[mRad] = aR^b$. Background data is not available for survey line 3

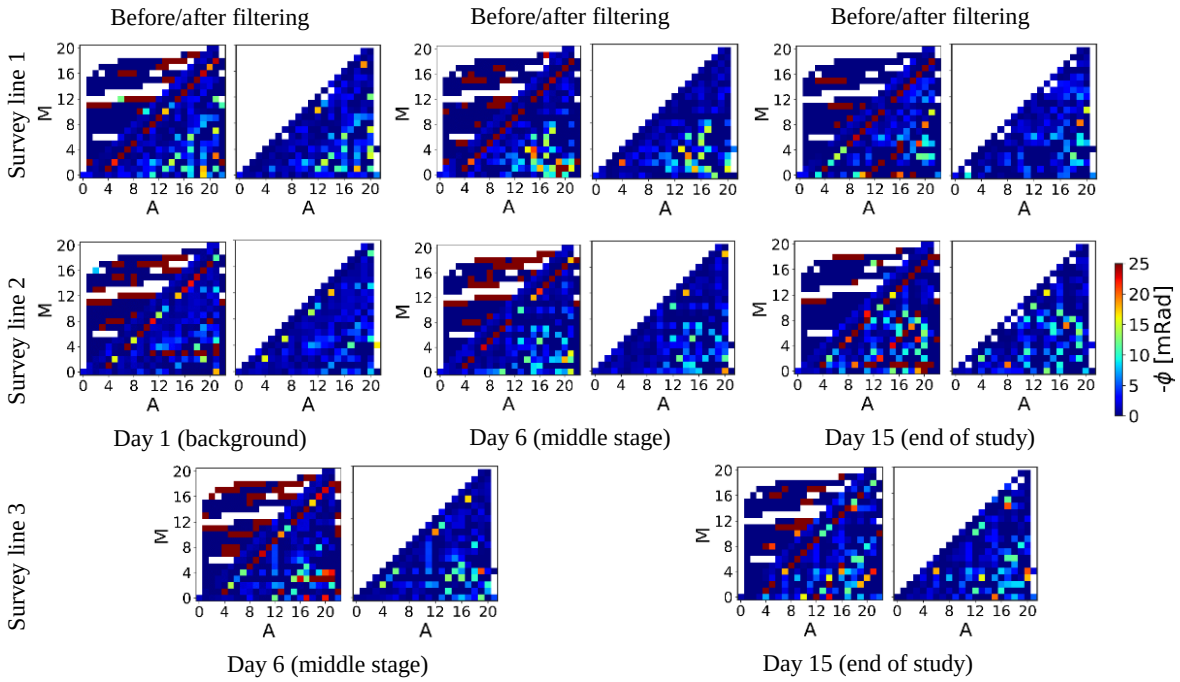

Figure 4.5: Plots of measured phase angle values before (left) and after (right) filtering. Each measurement is represented by a colored pixel where the x coordinate is position number of the first current electrode (A) and y coordinate is position number of first potential electrode (M) for a 4 electrode (A-B/current pair, M-N/potential pair) measurement. $-\phi > 25$ values are represented as dark red in raw plots and white pixels represent "no data" points. These graphs are plotted based on the first dipole-dipole skips in each dataset.

4.5 Results

Resistivity imaging, the electromigration term of IP surveys, provides a clear and consistent subsurface image that agrees very well with the site's well described geology (Figure 4.6a), but fails to provide temporal changes that could be associated to the MICP treatment (Figure 4.6b). On the other hand, imaginary conductivity, the polarization term of IP surveys, shows temporal changes that coincide with the location, and timing, of the MICP treatment (Figure 4.6b). Imaginary conductivity images show an overall 500% increase in signal while resistivity increased roughly 30% versus background. Subsurface phase images show similar behavior to imaginary conductivity; we chose to present the

detailed IP results in terms of resistivity and phase since these are the field parameters used during IP surveys.

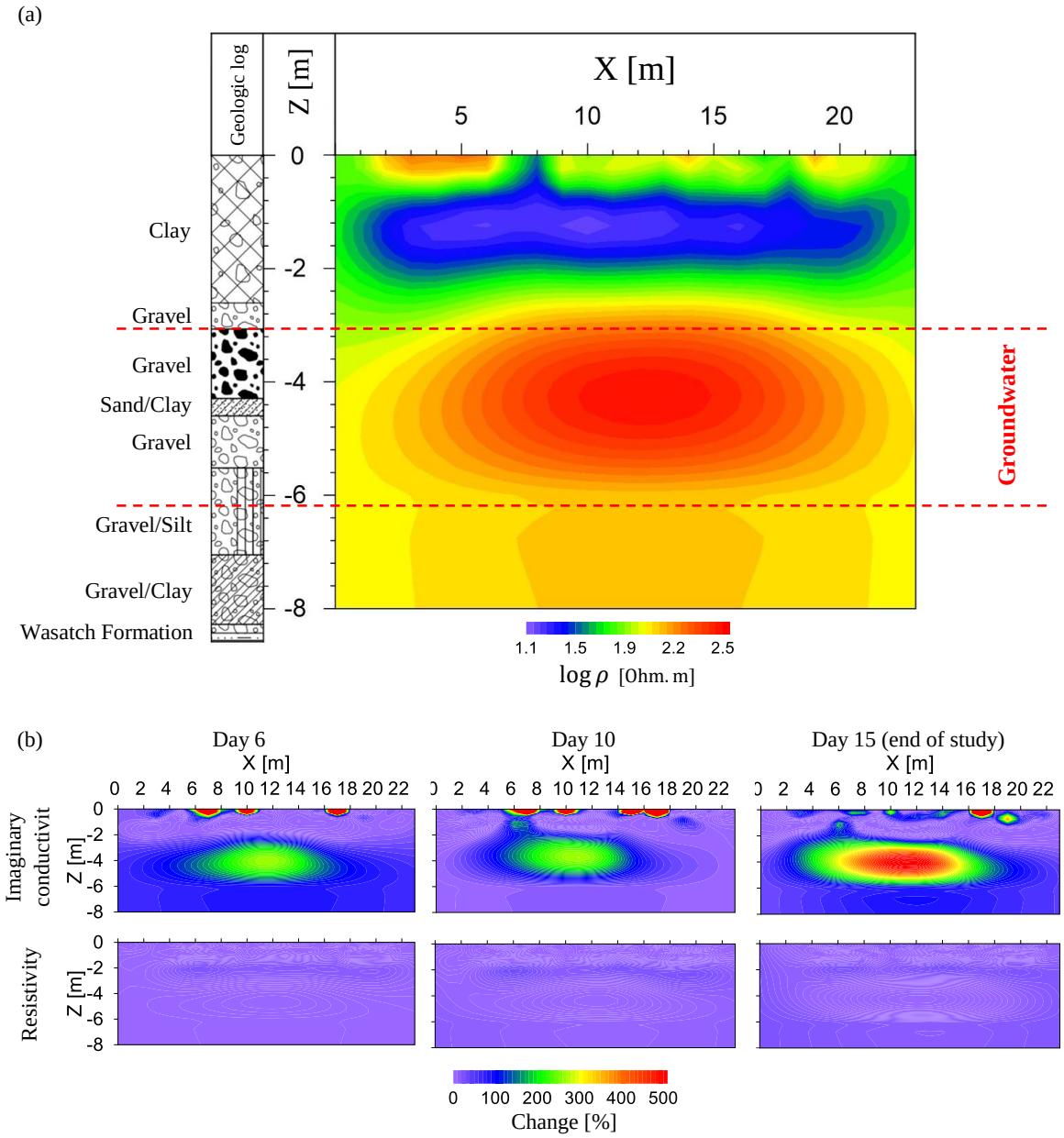

Figure 4.6: (a) Resistivity profile of the treatment plot (middle line – background data/before treatment) along with its geologic log (from extracted cores during borehole drilling at well 1) [*Fox et al.*, 2012], (b) Changes in imaginary conductivity (top) and resistivity (bottom) from background (day 1) for line 1. Other lines showed similar behavior.

Inverted phase angle subsurface images for each of the survey lines show clear changes from day 6 onward, in the groundwater zone, at depths of 3 to 6 meters (Figure 4.7 to Figure 4.9). Both the magnitude of the observed phase angle and the area that was impacted increased over time.

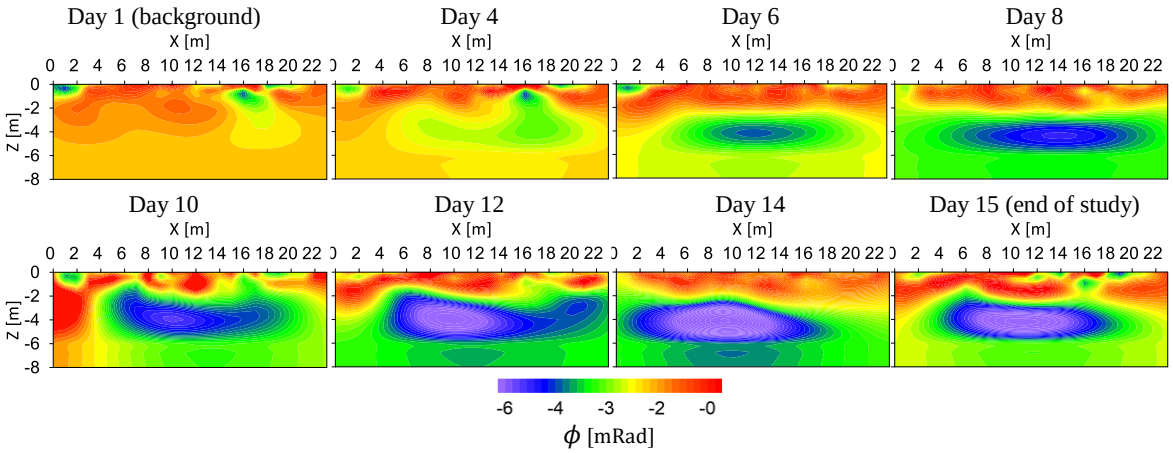

Figure 4.7: Phase angle changes over time for survey line 1.

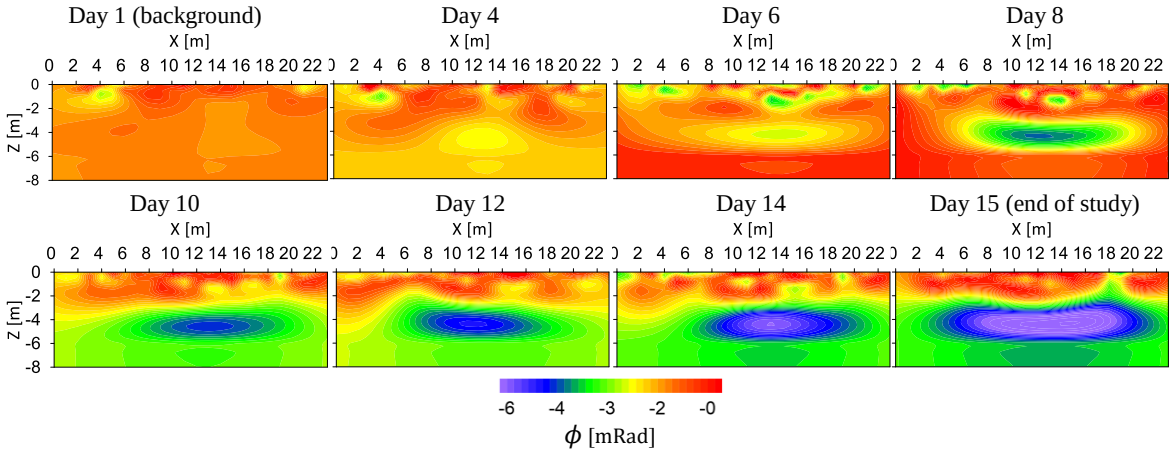

Figure 4.8: Phase angle changes over time for survey line 2.

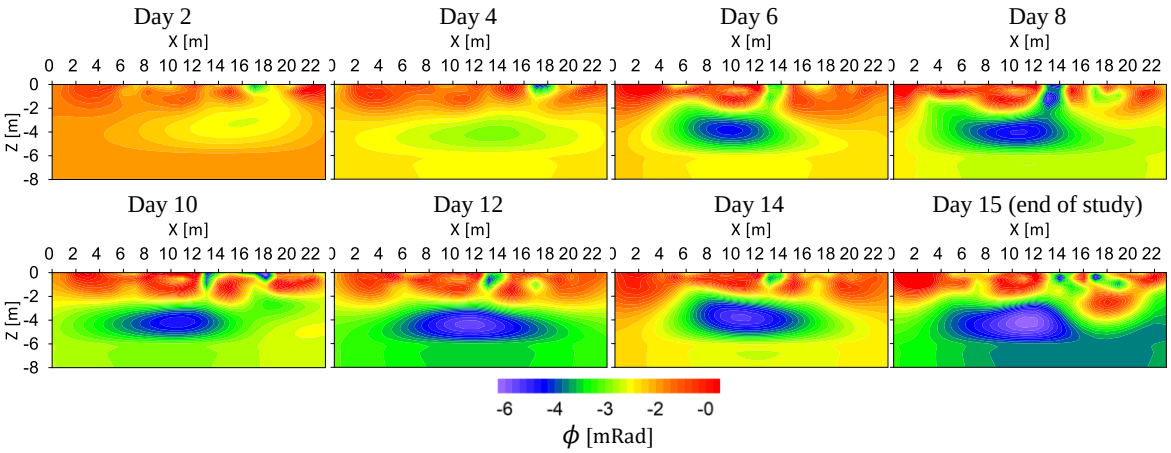

Figure 4.9: Phase angle changes over time for survey line 3. No background data is available.

A single day borehole NMR measurement was collected halfway through the experiment (day 7) and the data were used to estimate hydraulic conductivity (*K*) at three open boreholes. The *K* calculated is an order of magnitude lower for the center of the treatment area (well 1: $K = 3x10^{-2}$ m/day), compared to the wells peripheral to the treatment (well 2: $K = 6x10^{-1}$ m/day and well 3: $K = 10^{-1}$ m/day, Figure 4.1b) at the depth of interest (5 m).

At the end of the study, artificial substrate core samples were collected from open hole well 1 and then analyzed by X-Ray diffraction (XRD) to detect calcite. A peak at angle of 2Theta = 29.4^{o}, characteristic of calcite (green vertical lines, Figure 4.10), was observed in the treated soil sample only (Figure 4.10). In contrast, no calcite peak was observed for the same soil sample that was not incubated in the aquifer during the field study (control/untreated sample).

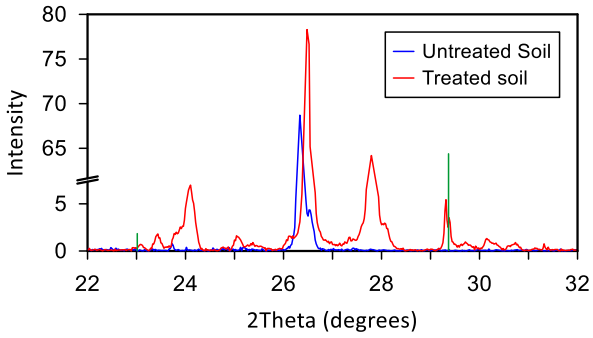

Figure 4.10: Results of XRD analysis of treated (after 15 days) and control/untreated soil samples for artificial substrate core samples retrieved from well 1. Green vertical lines show the 2Theta angle (ICDD PDF reference 00-005-0586) for pure calcite mineral [*JCPDS*, 2013]

4.5.1 Field observations

From day 11 until the end of the study, back pressure was observed during the injection process at well 14 resulting in a fluid backflow out of the well. Increase in the levels of ammonia [*Ohan*, 2018], indicative of ureolysis, was also observed initially in well 18 (middle of the treatment plot) and then in well 4 towards the end of the study (Figure 4.11). The difference in the solution conductivity between injection fluid (mixture of urea and molasses) and background (aquifer groundwater conductivity: ~1.54 mS/cm) was negligible. Average groundwater flow velocity was calculated at 0.63 m/day [*Fox et al.*, 2012].

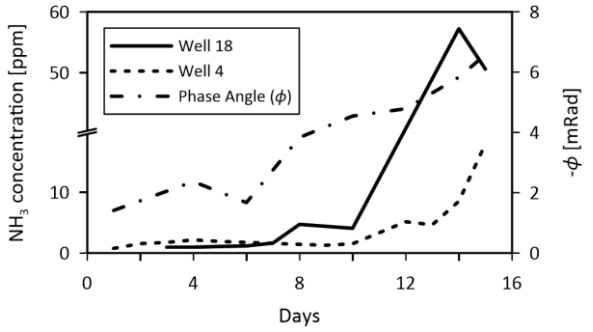

Figure 4.11: Daily measurements of ammonia (NH_3) concentration at wells 18 (middle of plot), well 4 and phase angle (ϕ) changes at location of 13 m (right above well 18) and depth of 4.5 m (ammonia sampling depth).

4.6 Discussion

Geochemical monitoring and field observations strongly suggest that the MICP treatment was successful. The confirmed presence of calcite precipitation in sediments that were incubated in the treated aquifer (XRD, Figure 4.10), and the higher ammonia concentration in the sampled groundwater (Figure 4.11), fully support active MICP in the target area. Additionally, the observed backflow in well 14 (Figure 4.1b) can be explained by pore clogging (due to calcite precipitation and/or biofilm development), further supports calcite precipitation at the treated area. Furthermore, the NMR measurements showing lower hydraulic conductivity in treated wells versus untreated wells are in complete agreement with calcite formation as a result of MICP processes. Pore clogging has been observed in previous MICP experiments and has been attributed to calcite precipitation and/or biofilm development [*Fujita et al.*, 2008].

Resistivity imaging provided clear images of the site geology but showed no changes in the subsurface that could be related to the MICP treatment. The conductive top layer (Figure 4.6a) correlates well with the engineered clay cap that was added to this site as a part of site remediation during the 1990s. Furthermore, the resistive bottom layer (~3.5 m bgs) coincides with the top of aquifer groundwater (Figure 4.6a) [*U.S. Department of Energy*, 1999].

On the other hand, subsurface imaginary conductivity images show clear and increasing changes in the treatment area over the duration of the experiment (Figure 4.6b). Unlike resistivity that shows bulk changes in subsurface, imaginary conductivity signal is sensitive to interfacial changes and since the imaginary component changes are far more dominant in the treatment area than the resistivity changes, it is safe to assume that

interfacial processes are the main driving mechanism [*Slater and Lesmes*, 2002], in agreement with calcite formation processes.

Subsurface images of phase angle, a common IP field parameter, closely follows the imaginary conductivity changes (Figure 4.7 to Figure 4.9). The phase angle changes were centered in the groundwater zone of injection, and propagated in the direction of fluid flow in the aquifer (groundwater/pumping). Phase angle anomalies increased (spatially) with time and the peak magnitude (~6 mRad) progressively reached larger volumes (Figure 4.12). The observed phase angle changes can safely be attributed to the MICP treatment, in agreement with the geochemical monitoring, and in the absence of any other possible subsurface processes (e.g., no rain or other influential event happened during this study). Indeed, phase angle anomalies can be linked to MICP processes; laboratory research has shown that calcite precipitation in porous media generates strong IP signals with recorded phase angles higher than 4 mRads [*Wu et al.*, 2010; *Saneiyan et al.*, 2018].

The results of the current field experiment strongly suggest that IP can be used to monitor MICP processes. Figure 4.12 presents a conceptual model of the MICP progress based solely on IP imaging (phase angle). Phase angle anomalies that were observed from approximately day 6 onward for all three lines highlight the onset of significant calcite formation, suggesting delay before optimal conditions (high concertation of ureolytic microbes) were achieved for MICP (given the groundwater velocity was ~0.63 m/day). We should also mention that the delayed observation can be related to the resolution of the geophysical imaging method, that might not be sensitive to early processes. Some calcite precipitation could have started earlier, but needed to be significant enough to generate a detectable signal by the IP survey.

For the conceptual model we chose the cutoff value of 4.5 mRad as the indicator of calcite precipitation based on laboratory experiments, and from published literature [*Wu et al.*, 2010; *Saneiyan et al.*, 2018]. This proof-of-concept field project validated the IP method as a potential monitoring aid in MICP projects (Figure 4.12). Following day 6, we note the advantage that geophysical monitoring can offer. From this point on, we saw the phase angle change expanding at higher rates. If we assume that the observed phase angle was due to calcite concentration, then IP can spatially and temporally monitor the status of soil strengthening (Figure 4.12). Such information can be helpful during the active soil strengthening projects, and also during integrity assessment of the treatment over the lifespan of such projects. Since some MICP changes may be reversible, IP may be able to identify 'weakening' areas that need to be retreated [*Saneiyan et al.*, 2018].

This project conclusively showed that MICP is a mature method for field applications of soil stabilization. There are still concerns over environmental issues, namely the generation of byproduct ammonia that can be harmful to aquatic organisms under certain conditions. Indeed, during our experiment the concentration of ammonia did reach levels up to 60 ppm in the wells directly downgradient from injection but only for a short period of time; we saw an increase after day 9 and a sharp decline after day 15 (Figure 4.11). The observed decline was likely due to the fact that the microbes were not being actively "fed" urea (towards the end of the study), decreasing the rate of conversion to ammonia. This evidence, combined with the fact that the old Rifle site has very fast recharge (20,000 L/day) [*Fox et al.*, 2012] means that ammonia would reach pre-injection levels quickly. Nonetheless, it is important to track the byproducts of any soil or aquifer amendment to ensure that no harmful compounds accumulate in the groundwater.

Future research should focus on field experiments designed for quantitative interpretation of MICP processes supported by complete geochemical data that can be used to constrain, and help define, the geophysical values. Furthermore, forward modeling before the actual field experiment is recommended to help design the optimal survey configuration for each specific. The results of our experiment can be used to guide future modeling efforts.

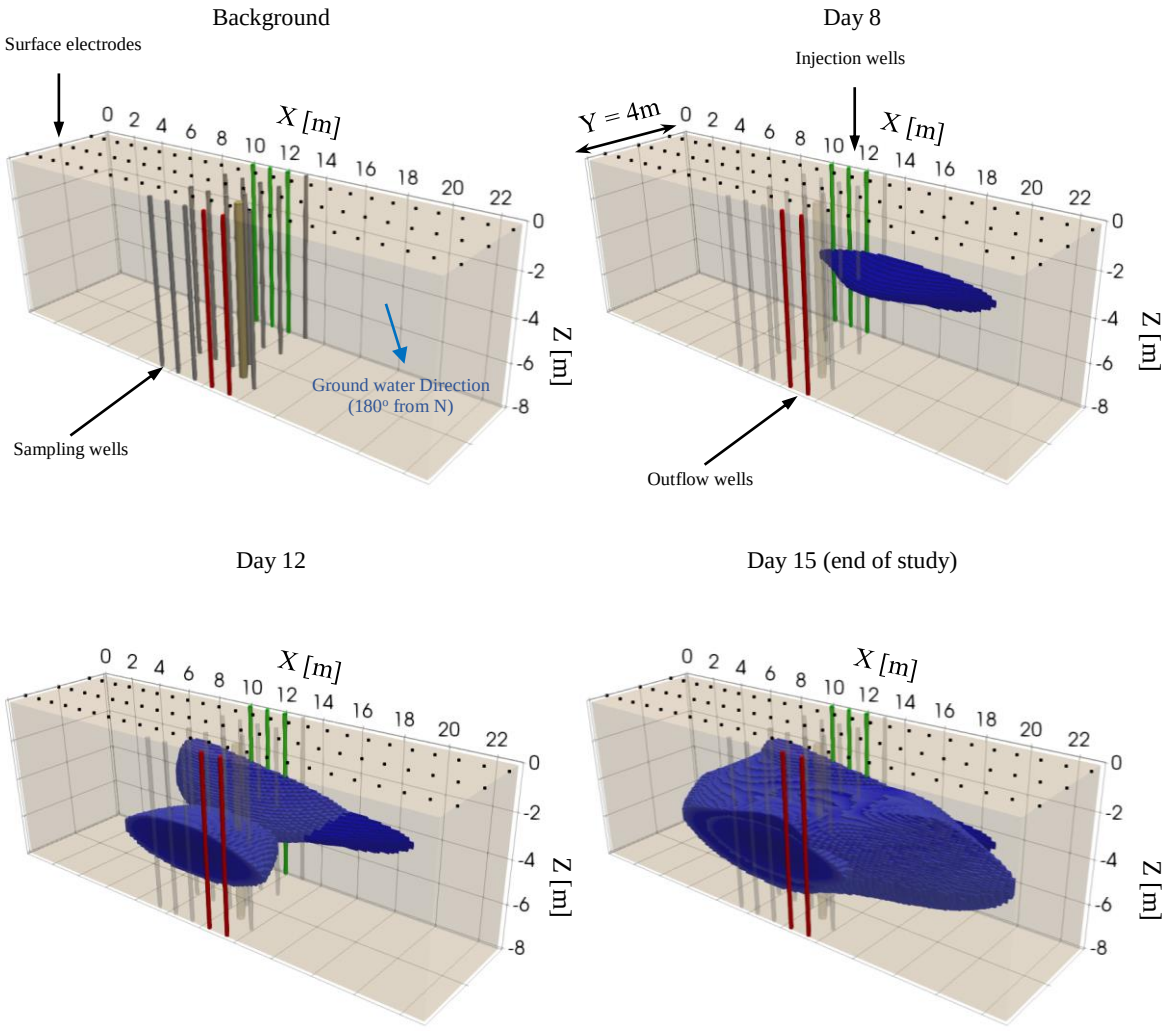

Figure 4.12: Conceptual 3D model of the progression of MICP in subsurface at the IFRC site from the beginning of the field study to the end, based on geophysical imaging. The cutoff value for the phase angle anomaly was $4.5 < -\phi < 6$ [mRad], which was based on laboratory experiments [*Wu et al.*, 2010; *Saneiyan et al.*, 2018]. Green vertical lines: injection wells, red vertical lines: withdrawal wells

4.7 Conclusion

Field applications of geophysical methods have long been accepted as standard and cost efficient techniques to monitor subsurface changes with minimal impact to the environment. ERI, commonly used in such investigations, failed to provide information on MICP processes, but needed information on local geology that was used for improving the IP data processing. This study clearly shows that the IP method can successfully monitor ground improvement processes as a result of MICP. IP is able to provide the direction and magnitude of these changes in real time. Conceptually, IP can be used for the long term autonomous monitoring of MICP treated sites, with complementary support of limited direct geochemical measurements. Further studies are needed to develop the quantitative links between IP signals and the degree of ground improvement.

Acknowledgements

We thank Dr. Andrew Parsekian (Department of Geology and Geophysics, University of Wyoming) for providing the Javelin 350 NMR tool and Dr. Bradley J. Carr (Wyoming Center for Environmental Hydrology and Geophysics) for conducting the NMR measurements. Special thanks to Dr. Ken Williams, Rifle IFRC site manager for providing access to the site, background information and on-site support. This project was funded by National Science Foundation [grant #1363224]. The data used in this paper will be available through the Rutgers University research data portal.

Chapter 5: Geophysical tools for monitoring bio-mediated soil stabilization processes[1]

Abstract

Soil stabilization processes aim at enhancing soil engineering properties. Although the concept is straight forward, it involves physical and chemical changes to the subsurface and includes utilizing complex processes and delicate balances. Bio-mediated soil stabilization, particularly microbial induced calcite precipitation (MICP), is no exception and needs to be well understood before real life applications. Hence, methods with high spatial and temporal resolution are required to monitor and characterize MICP application characteristics and the treatment long term performance. Spectral induced polarization (SIP), an established geophysical method, has shown to be sensitive to products of MICP before (e.g., calcite). In here, we performed a two-phase study to explore its suitability for field applications. Phase one involved a laboratory scale MICP study in a controlled environment and phase two a field scale study under real life conditions. In the laboratory, MICP was promoted through the introduction of ureolytic microorganisms, while in the field, indigenous soil microbes were stimulated; in both cases traditional geochemical monitoring along with temporally dense SIP monitoring were performed. The success of MICP was confirmed, in both phases, by chemical analysis. Over the course of the laboratory study, SIP successfully tracked the MICP progress as well as the microscale calcite precipitation behavior. Similarly, the SIP results of the field scale study showed to be sensitive to the subsurface changes due to MICP. SIP offered high resolution, temporal

[1] This chapter is under preparation for submission in Ecological Engineering.

and spatially dense, information on the MICP progress and status. Equally important, SIP signals related to field applications can be successfully studied in controlled laboratory environments despite complexity differences.

5.1 Introduction

Global population is increasing, and according to the United Nations, 55% of the total human population is located in urban areas and is expected to increase to 68% by 2050 [*United Nations, Department of Economic and Social Affairs*, 2018]. Increased urbanization has led to an increase in construction of buildings and infrastructures on smaller areas, where soils may suffer from substandard geotechnical characteristics (e.g., weak, loose or highly porous materials). To address this problem, engineers need to enhance the engineering properties (e.g., stiffness) of soils to bring these materials to within acceptable standards prior to any construction projects [*DeJong et al.*, 2010, 2013]. Currently, soil enhancement (stabilization) procedures include the use of synthetic, and in some cases natural, stabilizing agents (e.g., cement grouting, lime grouting) into the ground or use of purely physical forces (e.g., deep dynamic soil compaction). These procedures mostly depend on man-made material and processes that result in high application cost. Furthermore, synthetic material can be harmful to the environment and sometime to human health, for example, in instances where these materials contaminate groundwater. Traditional engineering procedures can also cause irreversible damage to soil microorganism viability and ecosystems [*Worrell et al.*, 2001; *Karol*, 2003; *Chang et al.*, 2015; *Mujah et al.*, 2017; *Wang et al.*, 2017].

A cost efficient and environmentally friendly method for soil stabilization is microbial induced calcite precipitation (MICP). MICP enhances soil's engineering

properties by using soil borne microorganisms to promote calcite formation that in turn acts to bind unconsolidated materials. MICP is suitable for construction purposes, and for anywhere that porosity/permeability reduction is required (e.g., crack remediation, confining contamination, erosion prevention and dust control) [*DeJong et al.*, 2010; *Abo-El-Enein and Ali*, 2012; *Montoya et al.*, 2013; *Mujah et al.*, 2017]. Additionally, MICP is suitable for long term applications and could be used in already developed areas (e.g., under existing buildings) [*Ivanov and Chu*, 2008; *Burbank et al.*, 2013; *Anbu et al.*, 2016].

Although MICP is an effective soil stabilization method in laboratory scale and in limited field applications [*DeJong et al.*, 2006; *Gomez et al.*, 2015; *Saneiyan et al.*, 2019], practical field implementations require further testing, and especially characterization during application and long term performance. Geophysical methods, routinely used for characterization and long term monitoring of subsurface processes [*Caterina et al.*, 2017; *Day-Lewis et al.*, 2017], can be used to support MICP applications [*Saneiyan et al.*, 2018]. The advantages of geophysical methods over conventional monitoring methods for evaluating the progress of MICP have been previously discussed [*Saneiyan et al.*, 2019].

The micro scale processes during MICP require elaborate studying and analysis that are usually followed by destruction of the samples. Thus, methods are required to obtain such information while preventing the destructive procedures. This research introduces a new geophysical technique, the spectral induced polarization (SIP), for the purpose of MICP characterization/monitoring and compares and contrasts with previously used approaches. SIP signals appear to be sensitive to multiple processes during MICP (e.g., calcite precipitation and microbial activity) [*Saneiyan et al.*, 2018, 2019] and could offer additional information on MICP that could be used to optimize application and long

term monitoring performance. To investigate the use of SIP as a method for non-destructive evaluation of progress of MICP in geological systems we conducted laboratory and field studies in which we added amendments to porous media to create conditions known to promote calcite precipitation. Our findings indicate that SIP could track MICP processes in the media (both in laboratory and field) and provide micro scale information about these processes without disrupting the media.

5.2 Background and theory

5.2.1 Microbiology of MICP

For MICP to proceed, microbes capable of urea hydrolysis must be present under conditions enriched with urea and calcium ions (Ca^{2+}). Among the microorganisms capable of ureolysis (decomposing urea), *Sporosarcina pasteurii* (*S. pasteurii*) is one of the most established candidates for MICP purposes. This ubiquitous soil bacterium efficiently decomposes urea (Equation 5.1) that could result in calcite precipitation in a calcium rich environment (Equation 5.2). Additionally, it has been shown that *S. pasteurii* produces large calcite crystals and offer better distribution of the precipitation (i.e., more homogeneous precipitation) by attaching to calcium ions (Equation 5.3), resulting in better overall soil's engineering qualities [*Mitchell and Ferris*, 2006; *Dhami et al.*, 2013; *Anbu et al.*, 2016; *Mujah et al.*, 2017; *Wang et al.*, 2017].

$$NH_2\text{-}CO\text{-}NH_2 + H_2O \rightarrow CO_3^{2-} + 2NH_4^{+} \quad (5.1)$$

$$Ca^{2+} + CO_3^{2-} \rightarrow CaCO_3 \downarrow \quad (5.2)$$

$$\text{Microbial cell-}Ca^{2+} + CO^{3-} \rightarrow \text{Cell-}CaCO_3 \downarrow \quad (5.3)$$

5.2.2 Geophysical monitoring

Geophysical methods are prime candidates for monitoring subsurface processes as they are cost efficient, minimally- or non-disruptive to the environment and subsurface, suitable for long-term monitoring applications and can offer real-time monitoring abilities along with high spatial and temporal resolution (e.g., *Binley and Kemna*, 2005; *Atekwana and Slater*, 2009; *Kemna et al.*, 2012).

5.2.2.1 Spectral induced polarization

Induced polarization (IP) is an established geophysical method used to study the low frequency resistive and capacitive characteristics of soils [*Binley and Kemna*, 2005; *Kemna et al.*, 2012]. IP can be measured in both time-domain (TDIP) and frequency-domain (spectral IP - SIP). Generally, electrical current in the subsurface travels through ionic and electronic pathways; the former, through electrolytic (σ_{ele}) and surface (σ_{surf}) conduction pathways [*Waxman and Smits*, 1968; *Lesmes and Frye*, 2001] and the latter, through electronic conductors (σ_{elc}) in the presence of interconnected conductive material (e.g., metallic minerals). In near-surface applications where redox processes are not involved and electronic conductors are sparse or absent, and the electrical conduction is dominated by ionic electro-migration [*Kemna et al.*, 2012]. σ_{ele} is primarily controlled by the physical properties of pore fluid and σ_{surf} is a complex electrical property and mainly controlled by surface properties (e.g., surface charge density, surface area and pore size distribution) at the electrical double layer (EDL) (i.e., is less dependent on fluid properties). These conduction pathways are typically modeled to act in parallel [*Waxman and Smits*, 1968; *Lesmes and Frye*, 2001; *Binley and Kemna*, 2005; *Kemna et al.*, 2012; *Weller et al.*, 2013].

SIP parameters (conductivity magnitude, $|\sigma|$, and phase shift, ϕ) are typically measured through a 4-electrode configuration (similar to DC resistivity), two current injection and two for potential measurement. The imaginary (σ'') and real (σ') components of complex (σ^*) conductivity can be calculated from the measured parameters (Equations 5.4 to 5.6) [*Binley and Kemna*, 2005; *Kemna et al.*, 2012].

$$\sigma^* = \sigma' + i\sigma'' = |\sigma|e^{i\phi} \tag{5.4}$$

$$\sigma' = \sigma'_{ele} + \sigma'_{surf} \tag{5.5}$$

$$\sigma'' = \sigma''_{surf} \tag{5.6}$$

where $i = \sqrt{-1}$, $\sigma' = |\sigma|\cos(\phi)$ and $\sigma'' = |\sigma|\sin(\phi)$.

5.2.2.2 Shear-wave velocity

Shear-wave velocity measurement (V_s) is a commonly used method in geotechnical engineering for characterizing small-strain shear modulus (G_{max}) in soils [*Stokoe et al.*, 1999; *Yang and Liu*, 2016]. In the laboratory, V_s is measured by piezoelectric bender elements [*Lee and Santamarina*, 2005; *Choo et al.*, 2017]. G_{max} is related to soil stiffness and can be calculated through shear-wave velocity (Equation 5.7).

$$V_s = (G_{max}/\rho)^{1/2} \tag{5.7}$$

where V_s is the shear wave velocity (m/s), G_{max} is the shear modulus, and ρ is the soil density [*Santamarina et al.*, 2001].

As a non-invasive method, V_s is sensitive to calcite precipitation during MICP, with signal increase directly correlated with calcite precipitation density [*Martinez et al.*, 2013; *Gomez et al.*, 2017; *Saneiyan et al.*, 2018].

5.3 Experiment setup and procedure

Two phases have been designed for this research. Phase 1 was conducted as a laboratory scale study in a controlled environment to study the mechanisms of MICP and develop monitoring protocols. Phase 2 was conducted as a field scale study in a natural setting, to study the effectiveness of the MICP treatment in typical field conditions.

5.3.1 Phase 1: laboratory scale study

5.3.1.1 Sample preparation

As porous media we used a mixture of 95% by weight (weight %) clean Ottawa sand (Diameter: 0.6 – 0.85 mm) and 5% pure Kaolinite powder. The soil mixture was mechanically mixed to reach a homogeneous grain distribution, following standard laboratory procedures [*Heenan et al.*, 2013], resulting in a total porosity of 26.5%. The mixture was prepared in this fashion to simulate natural conditions, ensure a better shear-wave velocity signal [*Cardoso et al.*, 2018; *Saneiyan et al.*, 2018] and allow free movement of microbial cells [*DeJong et al.*, 2006]. To minimize microbial contamination, soil samples were autoclaved before the experiment.

S. pasteurii (ATCC 11859) samples were batch cultivated at 30 ^{o}C for 24 h on solid growth medium (cultivation medium mixed with agar) and then transferred to sterile liquid cultivation medium (Table 5.1). Inoculated cultivation medium was incubated at 30 ^{o}C for 24 h prior to harvesting the microbial cells (to reach optimum turbidity). Turbid medium was centrifuged (5000 rpm for 15 min) and cells were harvested from bottom of the container, then resuspended in 25 ml of sterile calcite precipitation medium prior to MICP treatment (Table 5.1) [*Ferris et al.*, 1996; *Whiffin*, 2004; *DeJong et al.*, 2006; *Whiffin et al.*, 2007].

Table 5.1: Summary of laboratory scale MICP treatment solutions

Solution	***Constituents***
Cultivation medium	20 g/L yeast extract 8 mM $(NH_4)_2SO_4$ 13 mM Tris buffer (to adjust at pH 9)
Calcite precipitation medium	3 g/L Dehydrated nutrient broth (Difco) 25 mM $CaCl_2$ 25 mM $NaHCO_3$ 333 mM Urea
Microbial treatment medium	Suspended microbial cells in 25 ml of Calcite precipitation medium
Rinse	0.2 - 0.3 S/m KCl

5.3.1.2 Column design

Measurements were conducted in PVC sample holders (columns) equipped with four electrodes and two shear-wave velocity sensors (bender elements) (Figure 5.1). The non-polarizing Ag-AgCl potential electrodes were placed outside of the current flow to minimize spurious polarization effects [*Vanhala and Soininen*, 1995; *Abdulsamad et al.*, 2016]. One column was used as active and the other as control. Both columns were washed in isopropyl alcohol (70%) bath prior to packing to minimize potential contamination.

5.3.1.3 Laboratory experiment setup and procedure

Treatment medium preparation:

Sterile PVC columns were wet packed with soil mixture to minimize air bubbles which are known to cause erroneous SIP and shear-wave velocity measurements. Columns were rinsed with deionized water at 0.5 ml/min for 4 h prior to the introduction of calcite precipitation solution (Table 5.1). Then, columns were saturated with calcite precipitation medium (Table 5.1) at 0.5 ml/min for 6 h which was the time needed for complete saturation as evidenced by equivalent conductivity and pH values for inflow and outflow.

Background SIP and shear-wave velocity measurements were performed for 72 h until the columns reached an equilibrium condition as determined by constant geophysical signals [*Ustra et al.*, 2012; *Personna et al.*, 2013].

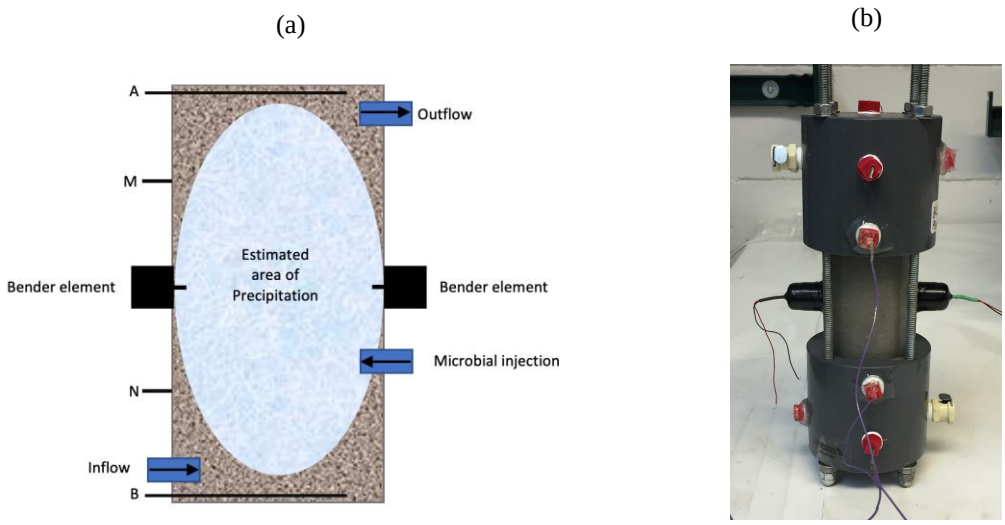

Figure 5.1: Experimental column. (a) Column schematics. A, B are current and M, N are potential electrodes. (b) Photo of the column.

MICP treatment:

In the active column, under no-flow conditions, the microbial treatment solution (Table 5.1) was introduced to the column (Figure 5.1). After 24 h effluent samples were collected, and the columns were rinsed with KCl solution (conductivity: 0.2 – 0.3 S/m) at 0.04 ml/min for 24 h (Table 5.2). This rinse stage was designed to: 1) simulate actual observed field conditions, where the treatment region was under constant groundwater flow regime [*Saneiyan et al.*, 2019] and 2) minimize geophysical noise due to unusual increase in pore fluid conductivity as a result of the microbial treatment [*Saneiyan et al.*, 2016]. After rinsing, pH and conductivity were measured at inflow and outflow ports to ensure

complete saturation, and SIP and shear-wave velocity measurements were carried out (Table 5.2).

Table 5.2: Treatment and measurement procedure

Step	***Procedure***
1. MICP treatment	24 h of microbial treatment (no-flow condition)
2. KCl rinse	24 h of flushing with KCl solution (conductivity: 0.2 – 0.3 S/m) at 0.04 ml/min
3. Effluent sample collection	Solution samples were collected at the outflow port for ammonia measurements
4. Geophysical measurement	SIP and shear-wave velocity measurement
5. Repeat	Back to step 1

The control column underwent exactly the same procedure as the active column except that it lacked the microbial injection. Additionally, to ensure prevention of any microbial growth/activity, 150 mg/L $HgCl_2$ was added to the injection fluid.

Measurements procedure:

SIP measurements were performed in a 4.5 h cycle covering a frequency range of 1 mHz to 24 KHz with five measurements per logarithmic cycle. Shear-wave velocity measurements used square wave forms with frequency of 20 Hz and amplitude of 5 V. SIP and shear-wave velocity measurements as well as outflow solution samples for assessing pH, solution conductivity and ammonia concentration were measured at the end of each treatment stage (Table 5.2). The MICP treatment was repeated eight times over 16 days until no further changes in the geophysical signal (SIP) were observed. The experimental columns were kept in controlled laboratory temperature (25 ^{o}C, ± 1 ^{o}C) for the entirety of the study. At the end of the experimental cycle columns were drained then the soil samples

were extracted and oven-dried for 72 h. Dried samples were destructed for collecting smaller pieces to undergo XRD analysis.

5.3.2 Phase 2: field scale study

5.3.2.1 Study site description

The field study was performed at the Rifle Integrated Field Research Challenge (IFRC) site in city of Rifle in western Colorado. The Rifle IRFC site is the ideal choice for MICP studies since there is confirmed abundance of Ca^{2+} ions and the microbes needed to stimulate MICP in the aquifer [*Smith et al.*, 2012]. Furthermore, the site has been extensively studied in the recent past providing us with detailed geological and hydrogeological characterization (e.g., *U.S. Department of Energy*, 1999; *Anderson et al.*, 2003; *Flores Orozco et al.*, 2011; *Fox et al.*, 2012; *Saneiyan et al.*, 2019).

A series of cased and open wells were available at the IFRC for injection and collection of fluid samples from the aquifer at ~3.5 m below ground surface (bgs). The stratigraphic profile consisted of alluvial sediments of the Colorado River atop the impermeable layer Wasatch formation, capped with 1.75 m of engineered compacted clay (as a part of 1990's remedial processes) [*U.S. Department of Energy*, 1999; *Fox et al.*, 2012]. For this study, we injected stimulation and urea solutions (Table 5.3) into the aquifer from wells 12, 13, 14 and pumped groundwater from wells 25 and 26 to support the preferential flow path; samples for geochemical analysis were collected from wells 1, 2, 3, 4, 18, 25 and 26 (Figure 5.2b).

(a)

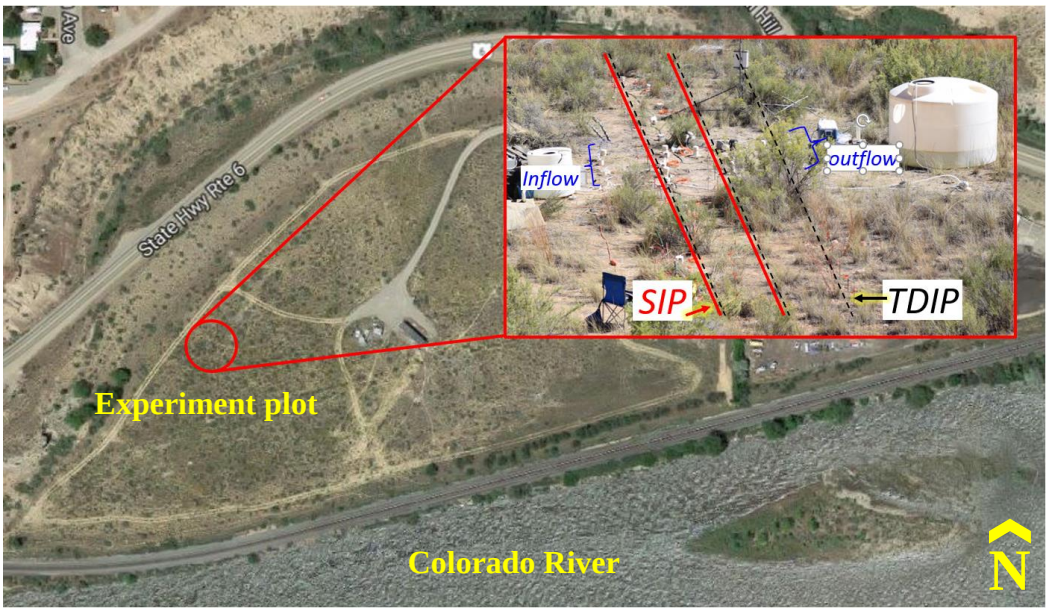

(b)

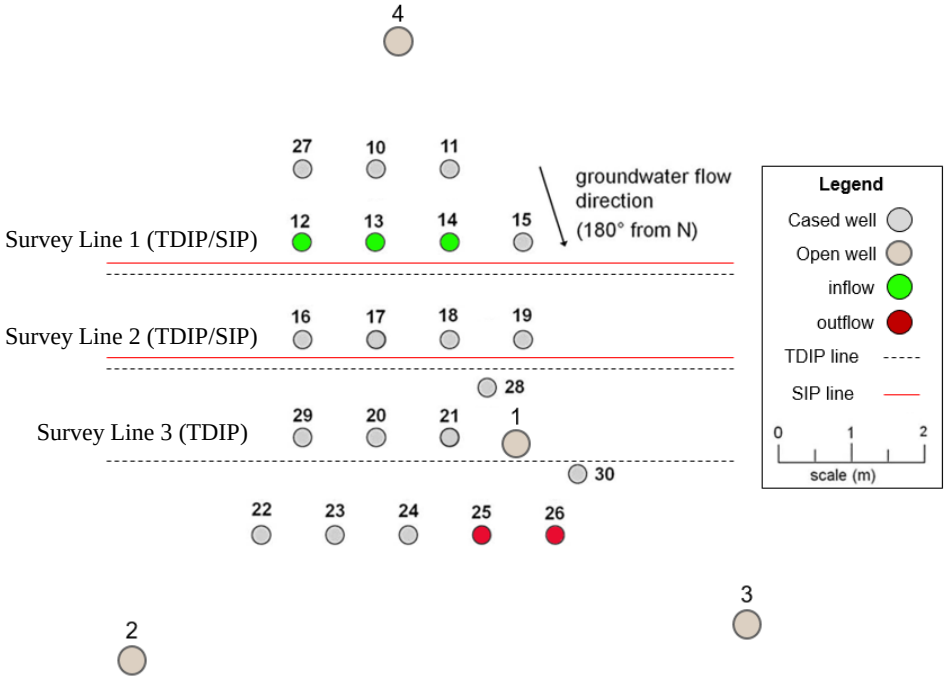

Figure 5.2: Study site. (a) The IFRC at Rifle, CO. Top right, view of survey setup and existing wells used in this study, (b) schematic of survey setup and existing wells at experiment plot (survey lines are clipped horizontally for visualization purposes) (modified from *Saneiyan et al.*, 2019)

5.3.2.2 Field experiment setup and procedure

Details of microbial treatment procedure can be found elsewhere [*Saneiyan et al.*, 2019]; in summary, microbial communities were initially stimulated by injecting the stimulation fluid (Table 5.3) at target treatment region (groundwater zone – 3.5 mbgs) followed by a 24 h waiting period to allow microbial growth (similar to laboratory cultivations). After the waiting period, the urea solution (Table 5.3) was injected in the treatment region on daily basis. MICP treatment was carried out for 15 days and geophysical measurements were performed on a daily basis during the treatment process.

SIP measurements were performed using SIP 256c (Radic Research) using 2 survey lines, each line with an array of maximum available 16 pairs of electrodes, and mixed electrode spacing (Figure 5.3) to cover the same area as TDIP measurements using Syscal pro (IRIS instruments); this paper is focused on the SIP data and compares the results with the TDIP results that were discussed in details in *Saneiyan et al.*, (2019). The 24 m long survey lines were centered around the treatment area, with the ends extended into the background area (unaffected by MICP) (Figure 5.2). SIP256c instrument uses separate current and potential electrode channels, and transmits signals through fiber optic to prevent electromagnetic coupling [*Schmutz et al.*, 2014]. Additionally, we used separate electrodes for current injection and potential measurement (current and potential electrodes were 10 cm offset on the y direction, same x location) for further reduction of electromagnetic coupling. We used graphite for potential measurements, since it has been shown to offer less noisy data [*LaBrecque and Daily*, 2008; *Kemna et al.*, 2012]. Survey configurations allowed for data collection at frequency range of 160 mHz to 500 Hz with maximum output voltage of 400 V and maximum output current of 100 mA.

Figure 5.3: Schematics of SIP and TDIP surface arrays used for the survey lines – 24 m long.

Table 5.3: Summary of field study's injection solutions.

Solution	***Constituents***
Stimulation	360 liters of 0.13 g sugarcane molasses/L of groundwater
Urea	360 liters – Day 2 to 4: 0.5 g urea/L, Day 8 to 14: 7.78 g urea/L
Groundwater pumping	From downgradient wells (Figure 5.2b) to support the preferential flow path, and collect fluid samples for geochemical monitoring.

5.3.2.3 Data processing

SIP data underwent similar processing approach discussed in *Saneiyan et al.*, (2019). In summary, bad measurements (-ϕ > 25, reciprocal error > 10 %) and nested measurements were removed. Based on *Saneiyan et al.*, (2019), a power-law error model was applied on the data (Equations 5.8 and 5.9). Data inversion was performed using BERT (pyGIMLi) [*Günther et al.*, 2016; *Rücker et al.*, 2017].

Resistance error model:

$$R_{error} = \alpha R_{avg}^{\beta} \; [ohm\ (\Omega)] \tag{5.8}$$

where: α and β are constants obtained from best fit,

$R_{error} = \left|R_{normal} - R_{reciprocal}\right|$ and $R_{avg} = \frac{R_{normal} - R_{reciprocal}}{2}$

Phase error model:

$$s(\phi) = aR^b\ [mRad] \tag{5.9}$$

where: *a* and *b* are constants obtained from best fit,

$s(\phi) = \left|\phi_{normal} - \phi_{reciprocal}\right|$ and $R = R_{normal}$

5.4 Results

5.4.1 Phase 1: laboratory scale study

5.4.1.1 Geophysical measurements

Laboratory measurements revealed a time-dependent response as the experiment progressed. Figure 5.4 shows formation of a distinct peak in imaginary conductivity signal at ~40 Hz with a consistent increase in magnitude over time until 192 h (Figure 5.4a). After 192 h, the magnitude of the peak response decreased over time and reached a constant level until end of the experiment at 384 h (Figure 5.4b). Although an increase in response was observed for a broad range of the frequency spectrum (~5 to ~500 Hz), the highest signal magnitude was observed at 40 Hz. The real conductivity component of the complex conductivity also shows temporal changes, but no spectral dependency (Figure 5.5). On the contrary to the active column, no noticeable changes in imaginary or real conductivity were observed in the control column response signal (Figure 5.6).

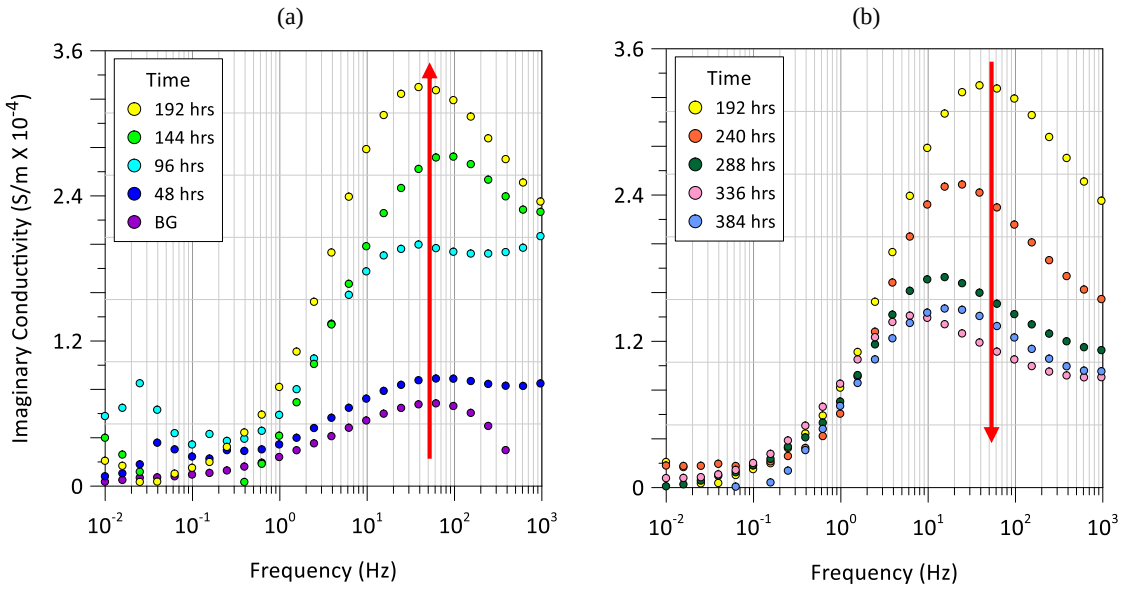

Figure 5.4: Imaginary conductivity spectra of active column. (a) Increasing signal over time until 192 h, (b) decreasing signal and reaching a constant level until the end of experiment (time 384 h). Red arrows show the signal trend.

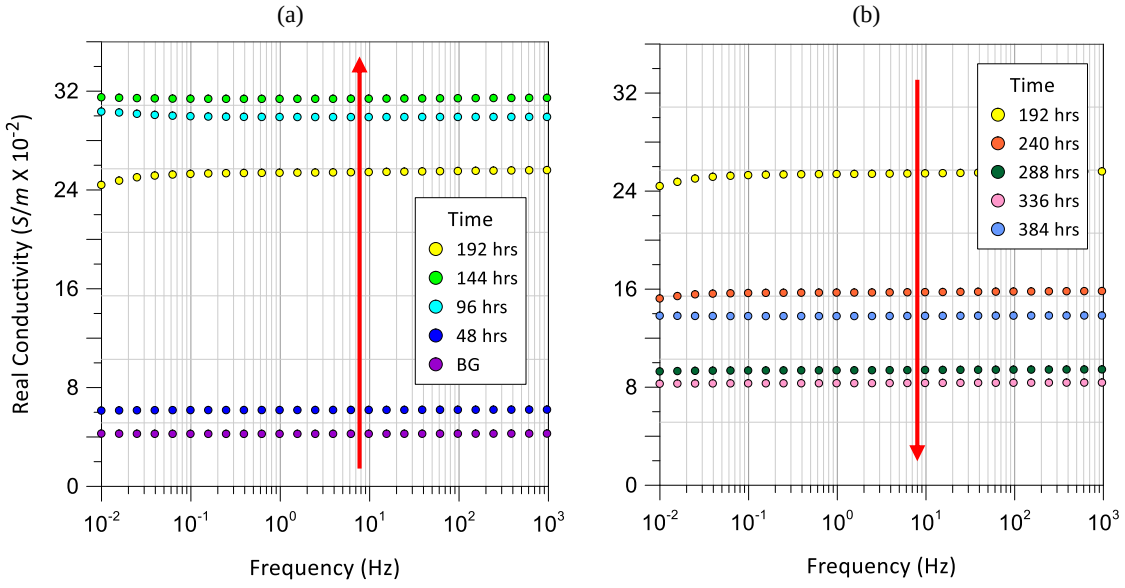

Figure 5.5: Real conductivity spectra of active column. (a) Increasing signal over time until 192 h, (b) decreasing signal until the end of experiment (time 384 h). Red arrows show the signal trend.

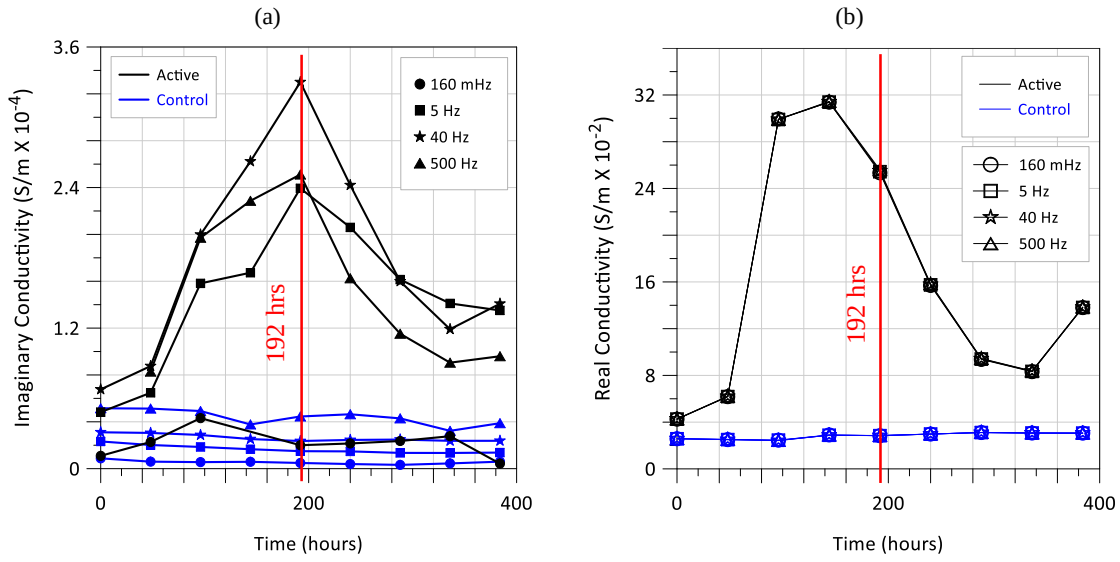

Figure 5.6: Single frequency response of (a) imaginary conductivity and (b) real conductivity, over time (at 160 mHz, 5, 40 and 500 Hz) for active (black) and control column (blue). Notice, markers ovelap for (b).

Shear-wave measurements were also affected by the treatment in the active column, where an overall ~34% increase in velocity was observed. Similar to the SIP measurements, no noticeable changes were observed in shear-wave measurements in the control column (Figure 5.7b).

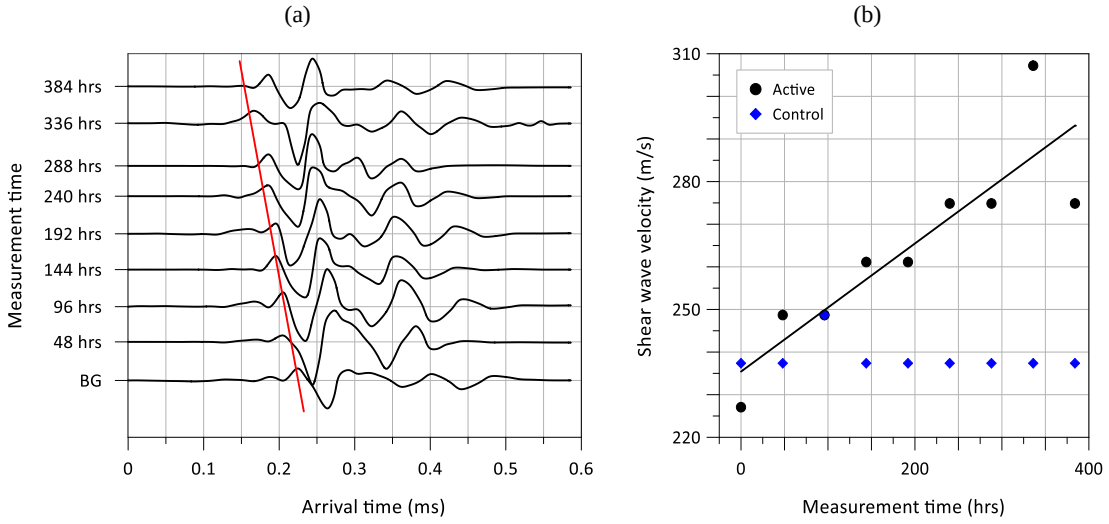

Figure 5.7: Shear-wave velocity response. (a) First arrival wave traces (red line shows the trend of first arrival signal), (b) shear-wave velocity values for active (black) and control (blue) columns.

5.4.1.2 Non-geophysical (direct) measurements

Chemical analysis on collected effluent samples (prior to flushing with KCl) from active column revealed elevated levels of ammonia concentration (NH_3) following each treatment application (Figure 5.8a) as would be expected if the cells were actively hydrolyzing urea. Additionally, XRD confirmed the formation of calcite after MICP treatment (Figure 5.8b). Expectedly, no such changes were observed in the control column.

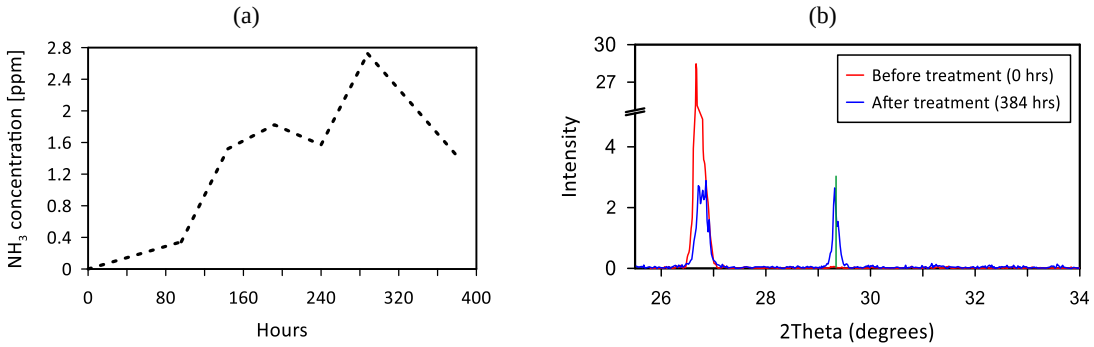

Figure 5.8: Non-geophysical measurements of fluids present in the column and solids from the column at the end of the experiment. (a) Ammonia concentration in solution, (b) XRD results for treated versus untreated soil sample. The green vertical line shows the 2Theta angle (ICDD PDF reference 00-005-0586) for pure calcite mineral [*JCPDS*, 2013]).

After the experiment was finished, samples were drained and dried in the oven for 72 h to visually verify the cementation efficiency. Figure 5.9 shows the before and after MICP experiment soil column samples. Control columns that did not receive microbial treatment were not consolidated at the end of the study.

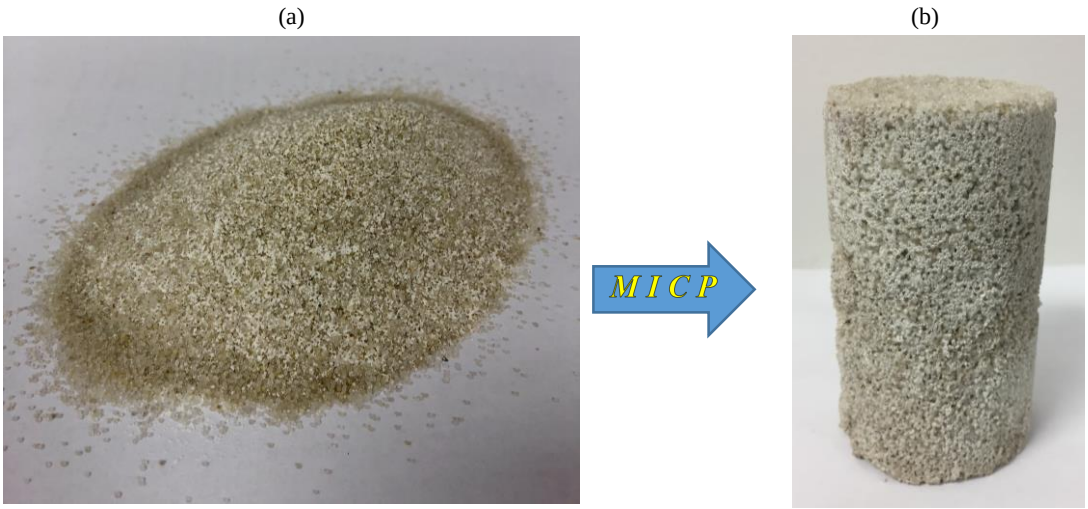

Figure 5.9: Soil mixture (a) before and (b) after 384 h of MICP processes. Unconsolidated soil mixture turned into consolidated state.

5.4.2 Phase 2: field scale study

SIP measurements were collected on daily basis, for 15 days at the field site during the experiment to stimulate MICP. Here we present only characteristic inversion profiles for days 0 (background signal – prior to MICP treatment), 5, 10 and 15 (end of study), that clearly show the MICP induced changes. The real component of complex conductivity (resistivity) shows a clear subsurface structure (Figure 5.10). The conductive top layer (0 to 1.75 mbgs) is consistent with the clay layer added during the Rifle IFRC site remediation, and the resistive layer (below 3.5 mbgs) is consistent with depth to fresh groundwater at the IFRC site [*U.S. Department of Energy*, 1999; *Fox et al.*, 2012; *Saneiyan et al.*, 2019]. However, resistivity fails to provide any temporal changes associated with the MICP treatment (Figure 5.10 and Figure 5.11). The minor, very localized, deviations from zero % change are present unchanged in all time lapse slices, suggesting systematic survey error (Figure 5.11). Consistent with laboratory measurements, the resistivity profile tends to be independent of frequency (Figure 5.10).

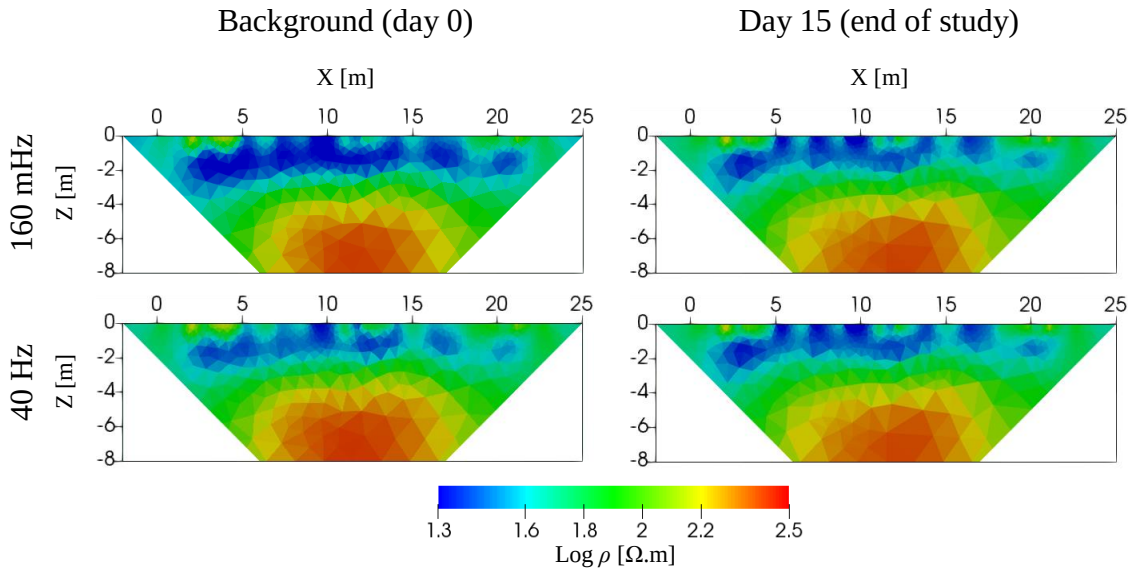

Figure 5.10: Resistivity measurements for line 1. Background (day 0) and day 15 (end of study) at frequencies 160 mHz and 40 Hz.

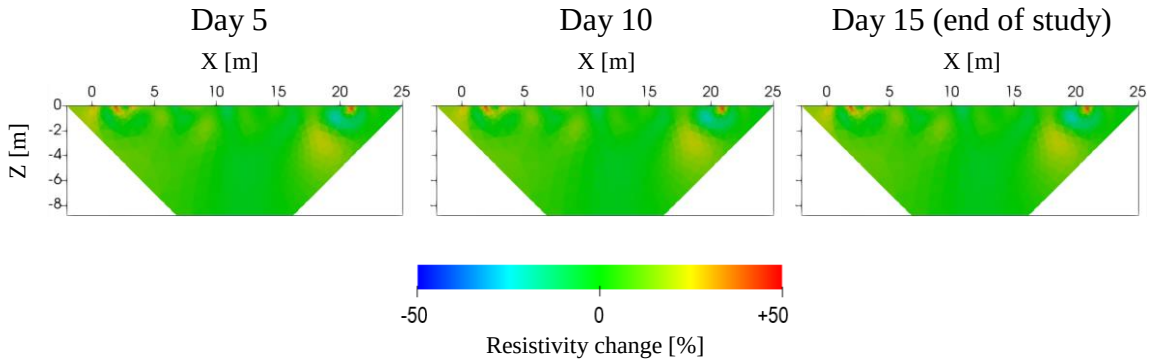

Figure 5.11: Percent changes against background (day 0) for line 1 at 40 Hz. Zero percent changes observed below 3.5 mbgs.

Contrary to resistivity, phase shift (field measured SIP parameter) measurements showed both temporal changes and frequency dependency, as the treatment progressed in the target treatment area (groundwater zone – below 3.5 mbgs) (Figure 5.12). Higher signal magnitude changes were observed at 40 Hz. Although not very clear, the background phase

measurements also show the subsurface structures, in agreement with both resistivity measurements and geological profile of IFRC site.

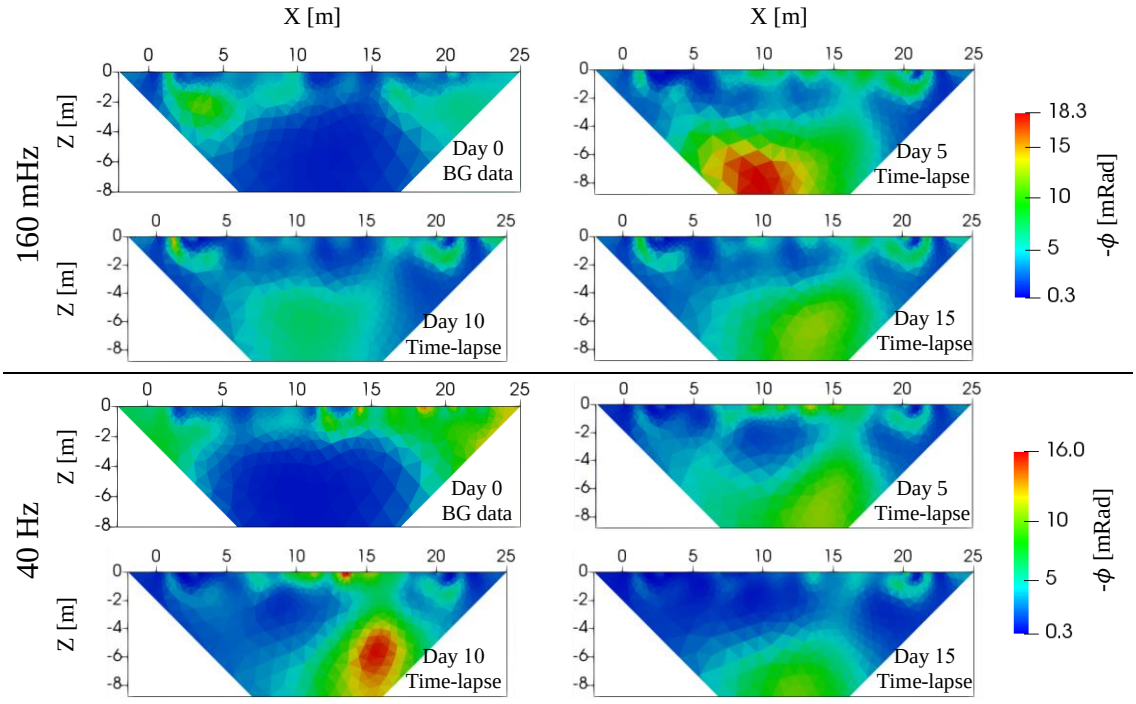

Figure 5.12: Time-lapse phase shift changes against background signal (day 0) for line 1 (line 2 behaved similarly with less pronounced magnitude) at frequencies 160 mHz and 40 Hz.

5.5 Discussion

The laboratory experiment phase confirmed that the soil column was improved (i.e., stabilized as a result of consolidation of soil grains) as a result of the MICP treatment. XRD analysis on the final consolidated soil sample (Figure 5.8b, Figure 5.9) verified the presence of calcite minerals in the active column confirming that urea hydrolysis had occurred resulting in formation of calcite. In addition, elevated ammonia (a byproduct of microbial ureolysis) concentrations at each treatment step (Figure 5.8a) indicates the presence of an active microbial community in the column capable of ureolysis, strongly suggesting the progressive activity of the microbes in this system [*Mitchell and Ferris*,

2006; *van Paassen et al.*, 2010]. Ammonia concentration is a common metric used during field application to confirm/monitor ureolysis; indeed, similar behavior was observed in the field project (phase 2), under a constant groundwater flow [*Saneiyan et al.*, 2019] and has been observed in previous MICP-related studies at the Rifle IFRC [*Smith et al.*, 2012].

Geophysical measurements (SIP and shear-wave) successfully monitored MICP progress in the laboratory scale experiment. The imaginary conductivity response in the active column showed both temporal and frequency dependency to MICP processes. The signal magnitude increased until 192 h and then decreased to reach a constant level, higher than pre-treatment values, for the remaining of the experiment (Figure 5.4 and Figure 5.6). This behavior is consistent with previous studies, focused on abiotic calcite precipitation [*Saneiyan et al.*, 2018], but the changes in this microbial driven process are observed over a broad frequency range (1- 500 Hz), with a wide peak at ~40 Hz. In the abiotic studies with sand and clay, the peak was ~1 Hz [*Saneiyan et al.*, 2018]. The higher frequency peak suggests finer grain mineralization compared to abiotic processes [*Klein and Sill*, 2002; *Titov et al.*, 2002; *Kemna et al.*, 2005], which is a known advantage of the MICP approach [*DeJong et al.*, 2010; *Wang et al.*, 2017]. Furthermore, experimental comparison of chemical (abiotic) and MICP driven processes showed the precipitation differences both on grain size and distribution (Figure 5.13). MICP produces an evenly distributed and fine grain precipitation (Figure 5.13b) in comparison to a coagulated precipitation in the abiotic experiment (Figure 5.13a).

The temporal behavior of the imaginary conductivity also yields interesting results. During the first half of the experiment the magnitude increased, maintaining the same frequency peak. This is assumed as a result of increasing volume of calcite precipitation

[*Wu et al.*, 2010; *Saneiyan et al.*, 2018] with homogeneous grain size distribution. After 192 h, the magnitude drops, in parallel with a peak frequency decrease. Both observations are assumed to be associated with increased grain size formation, or coagulation of grains associated with microbial activity and biofilm formation (Figure 5.14) [*Williams et al.*, 2005; *Bracco et al.*, 2012; *Van Driessche et al.*, 2017]. Hence, imaginary conductivity can be used to track the MICP stages, from early precipitation, to mature precipitation and biofilm formation. The latter stage would be the baseline for long term monitoring of the MICP treatment.

Figure 5.13: Calcite precipitation pattern at the bottom of a beaker. (a) Chemically induced calicite precipitation (mixture of Na_2CO_3 and $CaCl_2$). (b) Calcite precipitation as a result of MICP.

As expected, the real conductivity component of the SIP signal did not show any frequency dependency and showed only minimal temporal changes, failing to monitor the precipitation pattern during the MICP treatment. The absolute change of the signal magnitude was minimal, probably associated with changes in fluid conductivity as a result of calcite precipitation. The real component, analogous to DC resistivity measurements,

cannot effectively monitor the precipitation of microbial induced calcite but can be used to support the imaginary component monitoring.

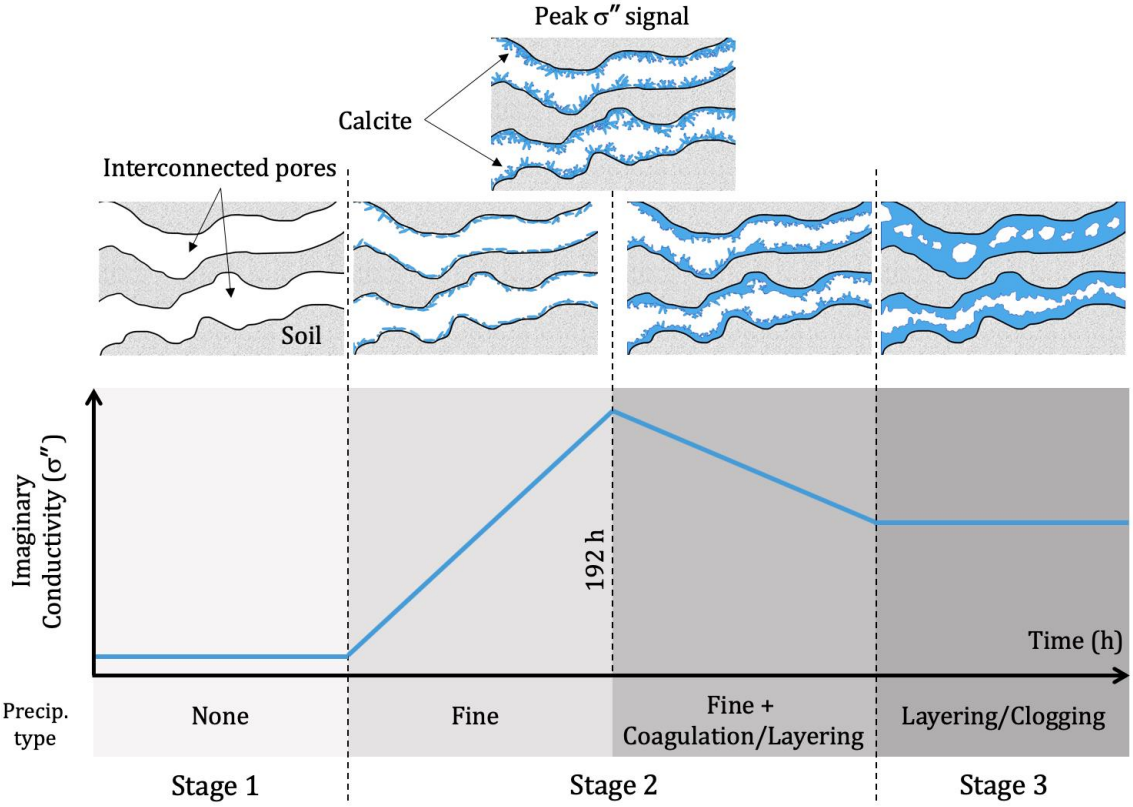

Figure 5.14: Conceptual model of calcite precipitation inside the column. Stage 1: no precipitation (background). Stage 2: precipitation of calcite minerals and formation of biofilm within the pore space. Stage 3: steady state, mineral layering and pore clogging.

Shear-wave velocity measurements, as standard soil stiffness measurements [*Stokoe et al.*, 1999; *Yang and Liu*, 2016], tracked the MICP progress by exhibiting an increasing trend over time. Overall, an increase of 34% in V_s was observed in our laboratory study. Although the increasing trend in shear-wave velocity signal is a clear indication of a successful MICP treatment (i.e., increase in soil stiffness/strength), similar to real conductivity signal we cannot characterize the stage of precipitation using this method.

The field scale experiment showed distinctive similarities to the laboratory experiment. MICP treatment was confirmed through the measured increase in ammonia concentration in collected effluent samples from the treatment target zone and the observation of calcite in incubated artificial soil samples taken from the treated region [*Saneiyan et al.*, 2019]. Despite minor near surface anomalies (probably associated with electrode noise and/or inversion routine), resistivity measurements did not show any change over time (Figure 5.11), or any frequency dependency (Figure 5.10), consistent with laboratory findings. Resistivity data were helpful though, because they provided a clear image of the subsurface geology that was used to constrain the geophysical data processing and interpretation.

Time-lapse inverted plots of phase shift revealed an increase in the signal magnitude until day 10 for higher frequencies (e.g., 40 Hz) followed by a decline, until the end of study (day 15), but remained higher compared to pre-treatment values. This behavior is also consistent with the laboratory findings suggesting progression from early MICP processes to a mature state. In addition, measurements at different frequencies showed elevated phase shift magnitude in the treatment area. Phase shift responses at different frequencies show the most change within the treatment area, allowing for efficient monitoring of the progress of MICP, but show some variability on the location, timing and magnitude of the peak response. This variability could be linked to different, distinctive MICP processes, and could potentially provide additional details on MICP progress.

Time domain IP (TDIP) measurements confirmed a successful MICP treatment in the field and were able to track the extent of the subsurface treatment (both spatially and temporally) [*Saneiyan et al.*, 2019]. Although TDIP would probably be adequate for real

life applications of MICP, SIP appears to provide additional information that are needed, at least in research studies, to better understand the MICP mechanisms and optimize field implementation. SIP data appear to better outline the treated area, and provide details on MICP progresses, from precipitation onset, to mature conditions.

5.6 Conclusion

MICP is an effective soil stabilization method; utilizing common soil borne microbes to achieve higher soil stiffness. This study confirms MICP performance in both laboratory and field settings, and introduces a new geophysical monitoring method for this purpose that offers significant advantages. Furthermore, the SIP signal in both studies exhibits similar trends at similar frequencies, allowing for direct comparison and further confirming the capability of the method in monitoring MICP with minimal dependency to the environment of application. Monitoring subsurface changes is challenging, expensive and typically suffers from low temporal and spatial resolution. Incorporating geophysical measurements can significantly reduce the cost and provide real time subsurface images, offering unparalleled spatiotemporal resolution. This research suggests that SIP can be successfully used as a MICP characterization and monitoring tool. SIP is clearly sensitive to MICP processes and can provide high resolution images of subsurface changes and these changes can be linked to different stages during MICP treatment and can be used for long term monitoring of the improved soil status. SIP can efficiently complement current monitoring practices, minimizing the need of invasive and expensive sampling.

Acknowledgements

We would like to thank Dr. Ken Williams, Rifle IFRC site manager for access to the site, background information and on-site support. This project was funded by National Science Foundation grant #1363224.

Chapter 6: Conclusions and future work recommendations

6.1 Summary of findings and work significance

First and most importantly, MICP is a promising environmentally safe solution for stabilizing soil. The active ingredients and to some extent, byproducts of MICP (ammonia - if controlled), are far less harmful to natural ecosystems and human health than most synthetic and man-made soil stabilization material. Secondly, MICP has the potential to efficiently stabilize large areas. The motility of the microorganisms in search of carbon source provides the transportation platform for stabilization reagents in subsurface. Making MICP not only capable of reaching the smallest pores, but also providing better cementation homogeneity. And lastly, MICP uses cost efficient and natural ingredients and requires fewer injection points; thus, from economical point of view, MICP is a cost-efficient soil stabilization method. Although MICP is still at its testing stages, it is clear that this method has several advantages over the common soil stabilization practice.

The only problem in understanding the subsurface processes of MICP is lack of spatiotemporal insights. Geophysical methods discussed in this thesis proved to be sensitive to MICP progress in media. IP specifically, shows to be very promising by providing 1, 2, and 3D images of the subsurface showing both spatial and temporal extents of MICP progression. It should be quite obvious that all geophysical methods discussed in this thesis certainly can complement the direct sampling methods and improve our understanding of MICP processes. Since geophysical methods indirectly provide a high spatiotemporal resolution images of subsurface, if combined with the right amount of direct samples can be significantly beneficial in the way of reducing costs and time of MICP monitoring projects.

In part one of this thesis (chapter 3), it is shown that spectral induced polarization is capable of tracking calcite precipitation in the medium, and also able to provide details of the precipitation pattern in higher spatiotemporal resolution than other methods. The precipitation pattern may not seem important at early stages, but it is important as the soil stabilization advances. The only way to ensure the quality of stabilized soil is to exactly monitor and measure the precipitation pattern. A coagulated pattern is undesirable and results in inhomogeneous cementation; prone to localized failure at uncemented spots. Long-term SIP monitoring can prevent such bad behaviors during MICP, simply by providing the cementation pattern.

While we cannot solely rely on geophysical methods for monitoring MICP, in chapter 4 it is shown that time domain induced polarization (TDIP) can significantly improve our understanding of impacted area of cementation during active MICP. Direct methods at a very high cost (e.g., excessive sampling and prolonged analysis time) hardly are capable of providing such information, and probably will result in degradation of the impacted area (due to bore hole drilling and destructive soil sampling). Additionally, the mentioned methods are incapable of real-time monitoring. However, the real-time TDIP monitoring provides all the spatiotemporal details about MICP while being cost-efficient, reliable, fast and easy-to-use.

In chapter 5 spectral induced polarization successfully showed not only in laboratory scale, but also field scale projects, we can obtain such valuable information about micro and macro scale details of MICP processes. Additionally, we saw a total agreement between laboratory and field scale SIP monitoring in this chapter; while the conditions at field are uncontrolled. This shows that SIP can distinguish background from

MICP signal. Although SIP provides detailed information regarding the MICP processes, compared to TDIP, this method can be time consuming in the field. Furthermore, the complex signal analysis may require experienced geophysicist's eyes. TDIP on the other hand, requires simpler data acquisition routines and signal analysis as well as shorter survey time. These benefits make TDIP more desirable for field applications, where high spatiotemporal resolutions in macro scale are required to delineate the MICP, but micro scale details can be neglected.

There are indeed some downsides to geophysical measurements, for instance it is very easy to misinterpret the obtained information in the absence of physical evidence. However, geophysical methods can reduce the number of physical sampling and therefore, the overall cost of the monitoring projects. Furthermore, geophysical methods can be obtained and analyzed in real-time; a feature that most direct monitoring techniques lack. It is also notable, geophysical methods (especially TDIP/SIP) can be used as viable long-term monitoring methods through permanent instrument installation at a site with remote controlling. All in all, geophysical methods are the future of MICP monitoring; even though further studying is required to ensure the data quality.

6.2 Future work recommendations

Although this current work proves to be beneficial in understanding MICP related processes, there are still remaining challenges in the field. Following research is suggested to overcome the remaining challenges and ambiguities:

1. Further controlled laboratory SIP/TDIP should be conducted to study and identify different precipitated phases during MICP. It is required to clarify

the mineralogy of precipitated carbonates and correlate them with SIP signal.

2. IP signatures of microbial communities versus the solid inorganic phase (carbonates) should be clarified. In depth laboratory studies using SIP can identify peak frequencies of each phase (organic versus inorganic).
3. Quantitative correlations between IP signal and solidification status (i.e., soil stiffness) of the soil underwent MICP.
4. On the field scale monitoring of MICP, future work is required to identify exact and consistent peak frequencies (SIP) related to cementation (calcite precipitation).
5. In depth microbial analysis in field scale with focus on ureolysis and correlation with geophysical signals are required. While the main focus of this thesis was geophysics, the effect of ureolysis rate and microbial activities on IP/SIP should be investigated in future.
6. Real-time geophysical measurements and long-term (on the scale of months) site characterization with remote field data acquisition should be investigated. In this thesis it is provided that SIP and TDIP are capable of autonomous data collection.

References

A. & Cheng, L. C. P. J. D. (2012), Identifying Groundwater Contamination Using Resistivity Surveys at a Landfill near Maoming, China, *Nat. Educ. Knowl.*, *3*(7), 20.

Abdulsamad, F., N. Florsch, M. Schmutz, and C. Camerlynck (2016), Assessing the high frequency behavior of non-polarizable electrodes for spectral induced polarization measurements, *J. Appl. Geophys.*, *135*, 449–455, doi:10.1016/j.jappgeo.2016.01.001.

Abo-El-Enein, S., and A. Ali (2012), Utilization of microbial induced calcite precipitation for sand consolidation and mortar crack remediation, *HBRC J.*, *8*(3), 185–192, doi:10.1016/j.hbrcj.2013.02.001.

Akiya, N., and P. E. Savage (2002), Roles of water for chemical reactions in high-temperature water.pdf, *Chem. Rev.*, *102*(8), 2725–2750, doi:http://dx.doi.org/10.1021/cr000668w.

Anbu, P., C.-H. Kang, Y.-J. Shin, and J.-S. So (2016), Formations of calcium carbonate minerals by bacteria and its multiple applications., *Springerplus*, *5*(1), 250, doi:10.1186/s40064-016-1869-2.

Anderson, N., R. Hoover, and P. Sirles (2008), *Geophysical Methods Commonly Employed for Geotechnical Site Characterization*.

Anderson, R. T. et al. (2003), Stimulating the In Situ Activity of Geobacter Species to Remove Uranium from the Groundwater of a Uranium-Contaminated Aquifer, *Appl. Environ. Microbiol.*, *69*(10), 5884–5891, doi:10.1128/AEM.69.10.5884-5891.2003.

Archie, G. E. (1942), The Electrical Resistivity Log as an Aid in Determining Some Reservoir Characteristics, *Trans. AIME*, *146*(01), 54–62, doi:10.2118/942054-G.

Arjwech, R., and M. E. Everett (2015), Application of 2D electrical resistivity tomography to engineering projects : Three case studies, , *37*(6), 675–681.

Atekwana, E. A., and L. D. Slater (2009a), Biogeophysics: A new frontier in Earth science research, *Rev. Geophys.*, *47*(4), 1–30, doi:10.1029/2009RG000285.

Atekwana, E. A., and L. D. Slater (2009b), Biogeophysics: A new frontier in Earth science

research, *Rev. Geophys.*, *47*(4), RG4004, doi:10.1029/2009RG000285.

Ayolabi, E. a, A. F. Folorunso, A. M. Odukoya, and A. E. Adeniran (2013), Mapping saline water intrusion into the coastal aquifer with geophysical and geochemical techniques : the University of Lagos campus case (Nigeria), , *2*(1), 1–14, doi:10.1186/2193-1801-2-433.

Bhaduri, S., N. Debnath, S. Mitra, Y. Liu, and A. Kumar (2016), Microbiologically Induced Calcite Precipitation Mediated by Sporosarcina pasteurii, *J. Vis. Exp.*, (110), 53253, doi:10.3791/53253.

Binley, A., and A. Kemna (2005), DC Resistivity and Induced Polarization Methods, in *Hydrogeophysics*, edited by Y. Rubin and S. S. Hubbard, pp. 129–156, Springer Netherlands, Dordrecht.

Boquet, E., a. Boronat, and a. Ramos-Cormenzana (1973), Production of Calcite (Calcium Carbonate) Crystals by Soil Bacteria is a General Phenomenon, *Nature*, *246*, 527–529, doi:10.1038/246527a0.

Börner, F. D., and J. H. Schön (1995), Low frequency complex conductivity measurements of microcrack properties, *Surv. Geophys.*, *16*(1), 121–135, doi:10.1007/BF00682716.

Börner, F. D., J. R. Schopper, and A. Weller (1996), Evaluation of transport and storage properties in the soil and groundwater zone from induced polarization measurements1, *Geophys. Prospect.*, *44*(4), 583–601, doi:10.1111/j.1365-2478.1996.tb00167.x.

Bracco, J. N., M. C. Grantham, and A. G. Stack (2012), Calcite growth rates as a function of aqueous calcium-to-carbonate ratio, saturation index, and inhibitor concentration: Insight into the mechanism of reaction and poisoning by strontium, *Cryst. Growth Des.*, *12*(7), 3540–3548, doi:10.1021/cg300350k.

Burbank, M., T. Weaver, M. Asce, R. Lewis, T. Williams, B. Williams, and R. Crawford (2013), Geotechnical Tests of Sands Following Bioinduced Calcite Precipitation Catalyzed by Indigenous Bacteria, *J. Geotech. Geoenvironmental Eng.*, *139*(6), 928–936, doi:10.1061/(ASCE)GT.1943-5606.0000781.

Burbank, M. B., T. J. Weaver, T. L. Green, B. C. Williams, and R. L. Crawford (2011), Precipitation of Calcite by Indigenous Microorganisms to Strengthen Liquefiable Soils, *Geomicrobiol. J.*, *28*, 301–312, doi:10.1080/01490451.2010.499929.

Burbank, M. B., T. J. Weaver, B. C. Williams, and R. L. Crawford (2012), Urease Activity of Ureolytic Bacteria Isolated from Six Soils in which Calcite was Precipitated by Indigenous Bacteria, *Geomicrobiol. J.*, *29*(4), 389–395, doi:10.1080/01490451.2011.575913.

Cardoso, R., I. Pires, S. O. D. Duarte, and G. A. Monteiro (2018), Effects of clay's chemical interactions on biocementation, *Appl. Clay Sci.*, *156*(September 2017), 96–103, doi:10.1016/j.clay.2018.01.035.

Caterina, D., A. Flores Orozco, and F. Nguyen (2017), Long-term ERT monitoring of biogeochemical changes of an aged hydrocarbon contamination, *J. Contam. Hydrol.*, *201*, 19–29, doi:10.1016/J.JCONHYD.2017.04.003.

Chang, I., A. K. Prasidhi, J. Im, and G. C. Cho (2015), Soil strengthening using thermo-gelation biopolymers, *Constr. Build. Mater.*, *77*, 430–438, doi:10.1016/j.conbuildmat.2014.12.116.

Cheng, L., and R. Cord-Ruwisch (2012), In situ soil cementation with ureolytic bacteria by surface percolation, *Ecol. Eng.*, *42*, 64–72, doi:10.1016/j.ecoleng.2012.01.013.

Choo, H., H. Nam, and W. Lee (2017), A practical method for estimating maximum shear modulus of cemented sands using unconfined compressive strength, *J. Appl. Geophys.*, *147*(Supplement C), 102–108, doi:https://doi.org/10.1016/j.jappgeo.2017.10.012.

Davis, C. A., E. Atekwana, E. Atekwana, L. D. Slater, S. Rossbach, and M. R. Mormile (2006), Microbial growth and biofilm formation in geologic media is detected with complex conductivity measurements, *Geophys. Res. Lett.*, *33*(18), 1–5, doi:10.1029/2006GL027312.

Day-Lewis, F. D., L. D. Slater, J. Robinson, C. D. Johnson, N. Terry, and D. Werkema (2017), An overview of geophysical technologies appropriate for characterization and monitoring at fractured-rock sites, *J. Environ. Manage.*, *204*, 709–720, doi:10.1016/J.JENVMAN.2017.04.033.

DeJong, J. et al. (2013), Biogeochemical processes and geotechnical applications: progress, opportunities and challenges, *Géotechnique*, *63*(4), 287–301, doi:10.1680/geot.SIP13.P.017.

DeJong, J. T., M. B. Fritzges, and K. Nüsslein (2006), Microbially induced cementation to

control sand response to undrained shear, *J. Geotech. Geoenvironmental Eng.*, *132*(November), 1381.

DeJong, J. T., B. M. Mortensen, B. C. Martinez, and D. C. Nelson (2010), Bio-mediated soil improvement, *Ecol. Eng.*, *36*(2), 197–210, doi:10.1016/j.ecoleng.2008.12.029.

Dey, A., and H. F. Morrison (1979a), Resistivity modeling for arbitrarily shaped three dimensional structures, *GEOPHYSICS*, *44*(4), 753–780, doi:10.1190/1.1440975.

Dey, A., and H. F. Morrison (1979b), Resistivity modelling for arbitrarily shaped two dimensional structures, *Geophys. Prospect.*, *27*(1), 106–136, doi:10.1111/j.1365-2478.1979.tb00961.x.

Dhami, N. K., M. S. Reddy, and A. Mukherjee (2013), Biomineralization of calcium carbonates and their engineered applications: a review., *Front. Microbiol.*, *4*(October), 314, doi:10.3389/fmicb.2013.00314.

Dlubac, K., R. Knight, Y. Q. Song, N. Bachman, B. Grau, J. Cannia, and J. Williams (2013), Use of NMR logging to obtain estimates of hydraulic conductivity in the High Plains aquifer, Nebraska, USA, *Water Resour. Res.*, *49*(4), 1871–1886, doi:10.1002/wrcr.20151.

Dobecki, T. L., and P. R. Romig (1985), Geotechnical and groundwater geophysics, *GEOPHYSICS*, *50*(12), 2621–2636, doi:10.1190/1.1441887.

Van Driessche, A. E. S., M. Kellermeier, L. G. Benning, and D. Gebauer (2017), *New Perspectives on Mineral Nucleation and Growth*.

Ferris, F. G., T. J. Beveridge, and W. S. Fyfe (1986), Iron-silica crystallite nucleation by bacteria in a geothermal sediment, *Nature*, *320*(6063), 609–611, doi:10.1038/320609a0.

Ferris, F. G., L. G. Stehmeier, A. Kantzas, and F. M. Mourits (1996), Bacteriogenic Mineral Plugging, *J. Can. Pet. Technol.*, *35*(08), 6, doi:10.2118/96-08-06.

Flores Orozco, A., K. H. Williams, P. E. Long, S. S. Hubbard, and A. Kemna (2011), Using complex resistivity imaging to infer biogeochemical processes associated with bioremediation of an uranium-contaminated aquifer, *J. Geophys. Res. Biogeosciences*, *116*(3), 1–17, doi:10.1029/2010JG001591.

Flores Orozco, A., A. Kemna, C. Oberdörster, L. Zschornack, C. Leven, P. Dietrich, and H. Weiss (2012), Delineation of subsurface hydrocarbon contamination at a former hydrogenation plant using spectral induced polarization imaging, *J. Contam. Hydrol.*, *136–137*, 131–144, doi:10.1016/j.jconhyd.2012.06.001.

Florsch, N., A. Revil, and C. Camerlynck (2014), Inversion of generalized relaxation time distributions with optimized damping parameter, *J. Appl. Geophys.*, *109*, 119–132, doi:10.1016/j.jappgeo.2014.07.013.

Fox, P. M., J. a. Davis, M. B. Hay, M. E. Conrad, K. M. Campbell, K. H. Williams, and P. E. Long (2012), Rate-limited U(VI) desorption during a small-scale tracer test in a heterogeneous uranium-contaminated aquifer, *Water Resour. Res.*, *48*(5), 1–18, doi:10.1029/2011WR011472.

Fujita, Y., J. L. Taylor, T. L. Gresham, M. E. Delwiche, F. S. Colwell, T. L. Mcling, L. M. Petzke, and R. W. Smith (2008), Stimulation of microbial urea hydrolysis in groundwater to enhance calcite precipitation., *Environ. Sci. Technol.*, *42*(8), 3025–3032, doi:10.1021/es702643g.

Gat, D., M. Tsesarsky, D. Shamir, and Z. Ronen (2014), Accelerated microbial-induced CaCO3 precipitation in a defined coculture of ureolytic and non-ureolytic bacteria, *Biogeosciences*, *11*(10), 2561–2569, doi:10.5194/bg-11-2561-2014.

Gomez, M. G., B. C. Martinez, J. T. DeJong, C. E. Hunt, L. A. deVlaming, D. W. Major, and S. M. Dworatzek (2015), Field-scale bio-cementation tests to improve sands, *Proc. Inst. Civ. Eng. - Gr. Improv.*, *168*(3), 206–216, doi:10.1680/grim.13.00052.

Gomez, M. G., C. M. Anderson, C. M. R. Graddy, J. T. DeJong, D. C. Nelson, and T. R. Ginn (2017), Large-Scale Comparison of Bioaugmentation and Biostimulation Approaches for Biocementation of Sands, *J. Geotech. Geoenvironmental Eng.*, *143*(5), 04016124, doi:10.1061/(ASCE)GT.1943-5606.0001640.

Günther, T., T. Martin, and C. Rücker (2016), Spectral Inversion of SIP field data using pyGIMLi / BERT Framework pyGIMLi Spectral field data inversion, *Proc. 4th Int. Work. Induc. Polariz.*, doi:10.1007/s10342-013-0711-4.G.

Gustafsson, J. P. (2016), Visual MINTEQ 3.1, *KTH, Sweden*. Available from: https://vminteq.lwr.kth.se/

Haeri, S. M., A. Hamidi, and N. Tabatabaee (2005), The effect of gypsum cementation on

the mechanical behavior of gravely sands, *Geotech. Test. J.*, *28*(4), 380–390.

Hammes, F., and W. Verstraete (2002), Key roles of pH and calcium metabolism in microbial carbonate precipitation, *Rev. Environ. Sci. Biotechnol.*, (1), 3–7, doi:10.1023/A:1015135629155.

Head, K. H. (1994), *Manual of Soil Laboratory Testing, Permeability, Shear Strength and Compressibility Tests*, 2nd ed., Wiley, John & Sons, Incorporated.

Heenan, J., A. Porter, D. Ntarlagiannis, L. Y. Young, D. D. Werkema, and L. D. Slater (2013), Sensitivity of the spectral induced polarization method to microbial enhanced oil recovery processes, *Geophysics*, *78*(5), E261–E269, doi:10.1190/geo2013-0085.1.

Heenan, J., L. D. Slater, D. Ntarlagiannis, E. A. Atekwana, B. Z. Fathepure, S. Dalvi, C. Ross, D. D. Werkema, and E. A. Atekwana (2015), Electrical resistivity imaging for long-term autonomous monitoring of hydrocarbon degradation: Lessons from the Deepwater Horizon oil spill, *Geophysics*, *80*(1), B1–B11, doi:10.1190/geo2013-0468.1.

Hohmann, G. W., and S. H. Ward (1981), Electrical methods in mining geophysics, *Econ. Geol*, *75*, 806–828.

Huang, H., and I. J. Won (2003), Real-time resistivity sounding using a hand-held broadband electromagnetic sensor, *Geophysics*, *68*(4), 1224–1231, doi:10.1190/1.1598114.

Ivanov, V., and J. Chu (2008), Applications of microorganisms to geotechnical engineering for bioclogging and biocementation of soil in situ, *Rev. Environ. Sci. Biotechnol.*, *7*(2), 139–153, doi:10.1007/s11157-007-9126-3.

JCPDS (2013), PDF 4+ ICDD Database, Joint Committee on Powder Diffraction Standards— International Centre for Diffraction Data, 12 Campus Blvd., Newtown Square, PA, 19073-3273, U.S.A, , © 1997-2014.

Karol, R. H. (2003), *Chemical Grouting And Soil Stabilization, Revised And Expanded*, 3rd, revised ed., CRC Press, New York.

Kemna, A., E. Räkers, and A. Binley (1997), Application of complex resistivity tomography to field data from a kerosene-contaminated site, in *3rd EEGS Meeting*,

pp. 151–154.

Kemna, A., H. M. Münch, K. Titov, E. Zimmermann, and H. Vereecken (2005), Relation of SIP Relaxation Time of Sands to Salinity, Grain Size and Hydraulic Conductivity, in *11th European Meeting of Environmental and Engineering Geophysics*.

Kemna, A. et al. (2012), An overview of the spectral induced polarization method for near-surface applications, *Near Surf. Geophys.*, 453–468, doi:10.3997/1873-0604.2012027.

Klein, J. D., and W. R. Sill (2002), Electrical properties of artificial clay-bearing sandstone, *Geophysics*, *47*(11), 1593–1605, doi:10.1190/1.1441310.

Knight, R., D. O. Walsh, J. J. Butler, E. Grunewald, G. Liu, A. D. Parsekian, E. C. Reboulet, S. Knobbe, and M. Barrows (2016), NMR Logging to Estimate Hydraulic Conductivity in Unconsolidated Aquifers, *Groundwater*, *54*(1), 104–114, doi:10.1111/gwat.12324.

Koestel, J., A. Kemna, M. Javaux, A. Binley, and H. Vereecken (2008), Quantitative imaging of solute transport in an unsaturated and undisturbed soil monolith with 3-D ERT and TDR, *Water Resour. Res.*, *44*(12), n/a-n/a, doi:10.1029/2007WR006755.

Kruschwitz, S., C. Prinz, and A. Zimathies (2016), Study into the correlation of dominant pore throat size and SIP relaxation frequency, *J. Appl. Geophys.*, *135*, 375–386, doi:10.1016/j.jappgeo.2016.07.007.

Laabidi, E., and R. Bouhlila (2016), Impact of mixing induced calcite precipitation on the flow and transport, *Carbonates and Evaporites*, 1–13, doi:10.1007/s13146-016-0305-6.

LaBrecque, D., and W. Daily (2008), Assessment of measurement errors for galvanic-resistivity electrodes of different composition, *Geophysics*, *73*(2), F55–F64, doi:10.1190/1.2823457.

Lee, J.-S., and J. C. Santamarina (2005), Bender Elements: Performance and Signal Interpretation, *J. Geotech. Geoenvironmental Eng.*, *131*(9), 1063–1070, doi:10.1061/(ASCE)1090-0241(2005)131:9(1063).

Lesmes, D. P., and K. . K. M. Frye (2001), Influence of pore fluid chemistry on the complex

conductivity and induced polarization responses of Berea sandstone, *J. Geophys. Res.*, *106*(B3), 4079–4090, doi:10.1029/2000JB900392.

Lesmes, D. P., and F. D. Morgan (2001), Dielectric spectroscopy of sedimentary rocks, *J. Geophys. Res. Solid Earth*, *106*(B7), 13329–13346, doi:10.1029/2000jb900402.

De Lima, O., and M. Sharma (1992), a Generalized Maxwell-Wagner Theory for Membrane Polarization in Shaly Sands, *Geophysics*, *57*(3), 431–440, doi:10.1190/1.1443257.

Maclennan, K. (2013), Methods for Addressing Noise and Error in Controlled Source Electromagnetic Data, Colorado School of Mines.

Marshallt, D. J., and T. R. Madden (1959), INDUCED POLARIZATION, A STUDY OF ITS CAUSES, *GEOPHYSICS*, *24*(4), 790–816, doi:https://doi.org/10.1190/1.1438659.

Martinez, B. C., J. T. DeJong, T. R. Ginn, B. M. Montoya, T. H. Barkouki, C. Hunt, B. Tanyu, and D. Major (2013), Experimental Optimization of Microbial-Induced Carbonate Precipitation for Soil Improvement, *J. Geotech. Geoenvironmental Eng.*, *139*(4), 587–598, doi:10.1061/(ASCE)GT.1943-5606.0000787.

Mitchell, A. C., and F. G. Ferris (2006), The Influence of Bacillus pasteurii on the Nucleation and Growth of Calcium Carbonate, *Geomicrobiol. J.*, *23*(3–4), 213–226, doi:10.1080/01490450600724233.

Mitchell, J. K., and J. C. Santamarina (2005), Biological Considerations in Geotechnical Engineering, *J. Geotech. Geoenvironmental Eng.*, *131*(10), 1222–1233, doi:10.1061/(ASCE)1090-0241(2005)131:10(1222).

Montoya, B. M., K. Feng, and C. Shanahan (2013), Bio-mediated soil improvement utilized to strengthen coastal deposits, in *the 18th International Conference on Soil Mechanics and Geotechnical Engineering*, pp. 2565–2568, Paris.

Moon, C. J., M. E. G. Whateley, and A. M. Evans (2006), *Introduction to mineral exploration*, Sydney: Blackwell Publishing.

Mujah, D., M. A. Shahin, and L. Cheng (2017), State-of-the-Art Review of Biocementation by Microbially Induced Calcite Precipitation (MICP) for Soil Stabilization,

Geomicrobiol. J., *34*(6), 524–537, doi:10.1080/01490451.2016.1225866.

Mwakanyamale, K., L. Slater, A. Binley, and D. Ntarlagiannis (2012), Lithologic imaging using complex conductivity: Lessons learned from the Hanford 300 Area, *GEOPHYSICS*, *77*(6), E397–E409, doi:10.1190/geo2011-0407.1.

Ng, W., M. Lee, and S. Hii (2012), An overview of the factors affecting microbial-induced calcite precipitation and its potential application in soil improvement, *World Acad. Sci. Eng. Technol.*, *62*(2), 723–729.

Nordsiek, S., and A. Weller (2008), A new approach to fitting induced-polarization spectra, *Geophysics*, *73*(6), F235, doi:10.1190/1.2987412.

Ntarlagiannis, D., N. Yee, and L. Slater (2005), On the low-frequency electrical polarization of bacterial cells in sands, *Geophys. Res. Lett.*, *32*(24), 2–5, doi:10.1029/2005GL024751.

Ntarlagiannis, D., J. Robinson, P. Soupios, and L. Slater (2016), Field-scale electrical geophysics over an olive oil mill waste deposition site: Evaluating the information content of resistivity versus induced polarization (IP) images for delineating the spatial extent of organic contamination, *J. Appl. Geophys.*, *135*, 418–426, doi:10.1016/j.jappgeo.2016.01.017.

Ohan, J. (2018), Microbial Community Dynamics of an Aquifer Biostimulated to Precipitate Calcite, Oregon State University.

Ohan, J., S. Saneiyan, J. Lee, D. Ntarlagiannis, S. Burns, and F. S. Colwell (2017), Microbial Community Structure of an Alluvial Aquifer Treated to Encourage Microbial Induced Calcite Precipitation, in *American Geophysical Union, Fall Meeting*, New Orleans, LA.

Omoregie, A. I., L. H. Ngu, D. E. L. Ong, and P. M. Nissom (2019), Low-cost cultivation of Sporosarcina pasteurii strain in food-grade yeast extract medium for microbially induced carbonate precipitation (MICP) application, *Biocatal. Agric. Biotechnol.*, *17*, 247–255, doi:10.1016/J.BCAB.2018.11.030.

Orozco, A. F., A. Kemna, and E. Zimmermann (2012), Data error quantification in spectral induced polarization imaging, *Geophysics*, *77*(3), E227, doi:10.1190/geo2010-0194.1.

Orozco, A. F., K. H. Williams, and A. Kemna (2013), Time-lapse spectral induced polarization imaging of stimulated uranium bioremediation, *Near Surf. Geophys.*, *11*(5), 531–544, doi:10.3997/1873-0604.2013020.

van Paassen, L. A., R. Ghose, T. J. M. van der Linden, W. R. L. van der Star, and M. C. M. van Loosdrecht (2010), Quantifying Biomediated Ground Improvement by Ureolysis: Large-Scale Biogrout Experiment, *J. Geotech. Geoenvironmental Eng.*, *136*(12), 1721–1728, doi:10.1061/(ASCE)GT.1943-5606.0000382.

Pelton, W. H., S. H. Ward, P. G. Hallof, W. R. Sill, and P. H. Nelson (1978), Mineral discrimination and removal of inductive coupling with multifrequency IP, *GEOPHYSICS*, *43*(3), 588–609, doi:10.1190/1.1440839.

Personna, Y. R., L. Slater, D. Ntarlagiannis, D. Werkema, and Z. Szabo (2013), Complex resistivity signatures of ethanol biodegradation in porous media, *J. Contam. Hydrol.*, *153*, 37–50, doi:10.1016/j.jconhyd.2013.07.005.

Al Qabany, A., K. Soga, and C. Santamarina (2012), Factors Affecting Efficiency of Microbially Induced Calcite Precipitation, *J. Geotech. Geoenvironmental Eng.*, *138*(8), 992–1001, doi:10.1061/(ASCE)GT.1943-5606.0000666.

Robinson, J. L. (2015), Improving characterization of fractured rock using 3D cross-borehole electrical resistivity tomography (ERT), , (May 2015), doi:10.7282/T3DF6T3V.

Robinson, J. L., L. D. Slater, and K. V. R. Schäfer (2012), Evidence for spatial variability in hydraulic redistribution within an oak-pine forest from resistivity imaging, *J. Hydrol.*, *430–431*, 69–79, doi:10.1016/j.jhydrol.2012.02.002.

Rodriguez-Navarro, C., F. Jroundi, M. Schiro, E. Ruiz-Agudo, and M. T. González-Muñoz (2012), Influence of substrate mineralogy on bacterial mineralization of calcium carbonate: Implications for stone conservation, *Appl. Environ. Microbiol.*, *78*(11), 4017–4029, doi:10.1128/AEM.07044-11.

Rücker, C., T. Günther, and F. M. Wagner (2017), pyGIMLi: An open-source library for modelling and inversion in geophysics, *Comput. Geosci.*, *109*(January), 106–123, doi:10.1016/j.cageo.2017.07.011.

Saneiyan, S., D. Ntarlagiannis, D. D. J. Werkema, F. S. Colwell, and J. Ohan (2016), Long Term Monitoring of Microbial Induced Soil Strengthening Processes, in *American*

Geophysical Union, Fall Meeting, San Francisco, CA.

Saneiyan, S., D. Ntarlagiannis, D. D. Werkema, and A. Ustra (2018), Geophysical methods for monitoring soil stabilization processes, *J. Appl. Geophys.*, *148*, 234–244, doi:10.1016/j.jappgeo.2017.12.008.

Saneiyan, S., D. Ntarlagiannis, J. Ohan, J. Lee, F. Colwell, and S. Burns (2019), Induced polarization as a monitoring tool for in-situ microbial induced carbonate precipitation (MICP) processes, *Ecol. Eng.*, *127*, 36–47, doi:10.1016/j.ecoleng.2018.11.010.

Santamarina, J. C., K. A. Klein, and M. A. Fam (2001), *Soils and waves:Particulate materials behavior, characterization and process monitoring*, Chichester; New York: J. Wiley & Sons.

Schmutz, M., A. Ghorbani, P. Vaudelet, and A. Blondel (2014), Cable arrangement to reduce electromagnetic coupling effects in spectral-induced polarization studies, *Geophysics*, *79*(2), A1–A5, doi:10.1190/geo2013-0301.1.

Scott, J. B. T. (2003), Determining pore-throat size in Permo-Triassic sandstones from low-frequency electrical spectroscopy, *Geophys. Res. Lett.*, *30*(9), 1–4, doi:10.1029/2003GL016951.

Seigle, H. O. (1959), MATHEMATICAL FORMULATION AND TYPE CURVES FOR INDUCED POLARIZATION, *Geophysics*, *24*(3), 547–565, doi:https://doi.org/10.1190/1.1438625.

Slater, L. D., and D. Lesmes (2002), IP interpretation in environmental investigations, *Geophysics*, *67*(1), 77, doi:10.1190/1.1451353.

Slater, L. D., and S. K. Sandberg (2000), Resistivity and induced polarization monitoring of salt transport under natural hydraulic gradients, *Geophysics*, *65*(2), 408, doi:10.1190/1.1444735.

Smith, R. W., Y. Fujita, S. S. Hubbard, and T. R. Ginn (2012), *Field Investigations of Microbially Facilitated Calcite Precipitation for Immobilization of Strontium-90 and Other Trace Metals in the Subsurface*.

Stokoe, K. H., M. B. Darendeli, R. D. Andrus, and L. T. Brown (1999), Dynamic soil properties: laboratory, field and correlation studies, in *Second International*

Conference on Earthquake Geotechnical Engineering, vol. 3, pp. 811–845.

Sumner, J. S. (2012), *Principles of Induced Polarization for Geophysical Exploration*, Vol. 5., Elsevier, Amsterdam, TheNetherlands, TheNetherlands.

Tabbagh, A., P. Cosenza, A. Ghorbani, R. Guérin, and N. Florsch (2009), Modelling of Maxwell–Wagner induced polarisation amplitude for clayey materials, *J. Appl. Geophys.*, *67*(2), 109–113, doi:https://doi.org/10.1016/j.jappgeo.2008.10.002.

Telford, W. M., L. P. Geldart, R. E. Sheriff, and D. A. Keys (1976), *Applied Geophysics*, Cambridge University Press.

Titov, K., V. Komarov, V. Tarasov, and a. Levitski (2002), Theoretical and experimental study of time domain-induced polarization in water-saturated sands, *J. Appl. Geophys.*, *50*(4), 417–433, doi:10.1016/S0926-9851(02)00168-4.

U.S. Department of Energy (1999), *Final Site Observational Work Plan for the UMTRA Project Old Rifle Site*.

United Nations, Department of Economic and Social Affairs, P. D. (2018), *World Urbanization Prospects: The 2018 Revision, Online Edition*.

Ustra, A., L. Slater, D. Ntarlagiannis, and V. Elis (2012), Spectral Induced Polarization (SIP) signatures of clayey soils containing toluene, *Near Surf. Geophys.*, *10*(6), 503–515, doi:10.3997/1873-0604.2012015.

Ustra, A., C. A. Mendonça, D. Ntarlagiannis, and L. D. Slater (2016), Relaxation time distribution obtained from a Debye decomposition of spectral induced polarization data, *Geophysics*, *81*(2), 1–10, doi:10.1190/GEO2015-0095.1.

Vanhala, H., and H. Soininen (1995), Laboratory technique for measurement of spectral induced polarization response of soil sampies, *Geophys. Prospect.*, *43*(5), 655–676, doi:10.1111/j.1365-2478.1995.tb00273.x.

Vinegar, H. J., and M. H. Waxman (1984), Induced polarization of shaly sands, *Geophysics*, *49*(8), 1267–1287, doi:10.1190/1.1441755.

Van Voorhis, G. D., H. Nelson, and T. L. Drake (1973), Complex resistivity spectra of

porphyry copper mineralization: Geophysics, *Geophysics*, *38*(1), 49–60, doi:https://doi.org/10.1190/1.1440333.

Walsh, D. et al. (2013), A small-diameter nmr logging tool for groundwater investigations, *Groundwater*, *51*(6), 914–926, doi:10.1111/gwat.12024.

Wang, C., and L. D. Slater (2019), Extending Accurate Spectral Induced Polarization Measurements into the kHz Range: Modeling and Removal of Errors from Interactions between the Parasitic Capacitive Coupling and the Sample Holder, *Geophys. J. Int.*, 895–912, doi:10.1093/gji/ggz199.

Wang, Z., N. Zhang, G. Cai, Y. Jin, N. Ding, and D. Shen (2017), Review of Ground Improvement Using Microbial Induced Carbonate Precipitation (MICP), *Mar. Georesources Geotechnol.*, *0618*(May), 1064119X.2017.1297877, doi:10.1080/1064119X.2017.1297877.

Ward, S. H. (1990), Resistivity and induced polarization methods, *Geotech. Environ. Geophys.*, *1*, 147–188.

Waxman, M. H., and L. J. M. Smits (1968), Electrical conductivities in oil-bearing shaly sands, *Trans Am Inst Miner. Met. Pet. Eng*, *243*(2), 107–122, doi:10.2118/1863-A.

Weigand, M., and A. Kemna (2016), Relationship between Cole-Cole model parameters and spectral decomposition parameters derived from SIP data, *Geophys. J. Int.*, *205*(3), 1414–1419, doi:10.1093/gji/ggw099.

Weil, M. H., J. T. DeJong, B. C. Martinez, and B. M. Mortensen (2012), Seismic and Resistivity Measurements for Real-Time Monitoring of Microbially Induced Calcite Precipitation in Sand, *Geotech. Test. J.*, *35*(2), doi:10.1520/GTJ103365.

Weller, A., and L. Slater (2012), Salinity dependence of complex conductivity of unconsolidated and consolidated materials: Comparisons with electrical double layer models, *Geophysics*, *77*(5), doi:10.1190/geo2012-0030.1.

Weller, A., W. Debschü;tz, and S. Nordsiek (2010), Estimating permeability of sandstone samples by nuclear magnetic resonance and spectral-induced polarization, *Geophysics*, *75*(6), 215–226, doi:10.1190/1.3507304.

Weller, A., L. Slater, and S. Nordsiek (2013), On the relationship between induced

polarization and surface conductivity: Implications for petrophysical interpretation of electrical measurements, *Geophysics*, *78*(5), D315–D325, doi:10.1190/geo2013-0076.1.

Whiffin, V. S. (2004), Microbial CaCO3 Precipitation for the Production of Biocement.

Whiffin, V. S., L. A. Van Paassen, and M. P. Harkes (2007), Microbial Carbonate Precipitation as a Soil Improvement Technique, *Geomicrobiol. J.*, *24*, 417–423, doi:10.1080/01490450701436505.

Williams, K. H., D. Ntarlagiannis, L. D. Slater, A. Dohnalkova, S. S. Hubbard, and J. F. Banfield (2005), Geophysical imaging of stimulated microbial biomineralization, *Environ. Sci. Technol.*, *39*(19), 7592–7600, doi:10.1021/es0504035.

Williams, K. H., A. Kemna, M. J. Wilkins, J. Druhan, E. Arntzen, A. L. N'Guessan, P. E. Long, S. S. Hubbard, and J. F. Banfield (2009), Geophysical monitoring of coupled microbial and geochemical processes during stimulated subsurface bioremediation, *Environ. Sci. Technol.*, *43*(17), 6717–6723, doi:10.1021/es900855j.

Wong, J. (1979), An electrochemical model of the induced-polarization phenomenon in disseminated sulfide ores, *GEOPHYSICS*, *44*(7), 1245–1265, doi:10.1190/1.1441005.

Worrell, E., L. Price, N. Martin, C. Hendriks, and L. O. Meida (2001), Carbon Dioxide Emission from the Global Cement Industry, *Annu. Rev. Energy Environ.*, *26*, 303–329, doi:10.1146/annurev.energy.26.1.303.

Wu, Y., S. Hubbard, K. H. Williams, J. B. Ajo-Franklin, and J. A. Franklin (2010), On the complex conductivity signatures of calcite precipitation, *J. Geophys. Res.*, *115*, 1–10, doi:10.1029/2009JG001129.

Yang, J., and X. Liu (2016), Shear wave velocity and stiffness of sand : the role of non-plastic fines, *Geotechnique*, *66*(6), 500–514, doi:http://dx.doi.org/10.1680/jgeot.15.P.205.